BOSTON UNIVERSITY

COLLEGE OF ENGINEERING

Dissertation

OPTICAL IMAGING MARKERS OF BREAST CANCER TREATMENT RESPONSE AND RESISTANCE

by

ANUP TANK

B.S., University of California, San Diego, 2016
M.S., Boston University, 2018

Submitted in partial fulfillment of the

requirements for the degree of

Doctor of Philosophy

2022

Approved by

First Reader

Darren Roblyer, Ph.D.
Associate Professor of Biomedical Engineering
Associate Professor of Electrical and Computer Engineering

Second Reader

Hadi Nia, Ph.D.
Assistant Professor of Biomedical Engineering
Assistant Professor of Materials Science and Engineering

Third Reader

David Boas, Ph.D.
Professor of Biomedical Engineering
Professor of Electrical and Computer Engineering

Fourth Reader

David J. Waxman, Ph.D.
Professor of Biology
Professor of Medicine
Professor of Biomedical Engineering

Fifth Reader

Jacopo Ferruzzi, Ph.D.
Assistant Professor of Biomedical Engineering
The University of Texas at Dallas

DEDICATION

To my family for inspiring me to take this journey

ACKNOWLEDGMENTS

To Darren, thank you for being my mentor and research advisor especially as a M.S. student when I was unsure about my path. I chose to stay for my PhD because of the environment you created where you empowered me to choose my own research path.

To all the BOTLab members, both former and present, thanks for being a great group to get to know and work with over the past six years. I would like to thank Hannah and Kavon, in particular, as those who have helped substantially with my work along the way.

To my undergraduate research mentor, Daryl Preece thanks for convincing me to get into optics when I knew nothing about the field and ended up spending the next 8 years of my life working on it.

To my committee members: Hadi Nia, David Boas, David Waxman, and Jacopo Ferruzzi, thank you for the assistance, insight and resources that you provided along the path.

To Christen, Allie, Stephanie, David Cawston and the rest of BME/BU members for all the assistance throughout the years.

To all of the friends I've made along the way, thanks for the memories and making this journey remarkable.

To Mom, Dad, and Nimit, you have been supporting me from the beginning and always encouraged me to follow my dreams, no matter where it leads.

OPTICAL IMAGING MARKERS OF BREAST CANCER TREATMENT RESPONSE AND RESISTANCE

ANUP TANK

Boston University College of Engineering, 2022

Major Professor: Darren Roblyer, Associate Professor of Biomedical Engineering

ABSTRACT

Breast cancer is currently projected to affect 1 in 8 women in the US over the course of their lifetime with more than 40,000 deaths in 2022. While there has been significant improvement in patient outcomes, the ongoing challenge of highly heterogeneous breast cancer responses to therapeutics, combined with the increasing array of agents and dosing regimens, highlights the importance of tools that can assist oncologists in monitoring and adapting regimens to improve outcomes. Non-invasive imaging modalities can provide valuable prognostic feedback by longitudinally tracking the functional and metabolic characteristic of tumors. This work focuses on a platform of three imaging modalities to investigate breast cancer response and progression in different models of different length scales from humans to mice to 3D spheroids. This dissertation will highlight two Diffuse Optical Imaging (DOI) techniques: Diffuse Optical Spectroscopic Imaging (DOSI) and Spatial Frequency Domain Imaging (SFDI) and a microscopy technique: Fluorescence Lifetime Imaging Microscopy (FLIM).

The preclinical setting, and in particular, in vitro models provide the unique advantage of controlling for biological heterogeneity compared to the clinical setting. In this setting, FLIM can measure the autofluorescence of key enzymatic metabolites and quantify levels of oxidative phosphorylation (OXPHOS) compared to glycolysis. A preliminary study demonstrated that FLIM could discriminate between non-invasive vs invasive breast cancer spheroids embedded in collagen and the metabolic profile was modulated by the density of the collagen. DOI techniques utilize near-infrared light to probe tissue and can quantify the optical absorption and scattering of tissue. These optical properties can be used to determine hemodynamic and cellular growth information about tissue and tumors. SFDI can provide widefield optical properties of tumors with a penetration depth of several millimeters making it the ideal imaging modality for tracking murine breast tumors. A major advantage of utilizing a murine breast cancer model is being able to study tumors in a living organism while controlling for both subject and tumor diversity. A study was conducted that confirmed SFDI derived optical scattering served as a prognostic biomarker to discriminate between a paired immunoresponsive and immunoresistant murine breast cancer model. Finally, DOSI is a clinical instrument that can provide point optical properties with a depth sensitivity of a few centimeters making this the ideal instrument for monitoring breast tumors in breast cancer patients. A large, multi-center clinical trial demonstrated that a large tumor oxyhemoglobin increase is a strong prognostic biomarker of treatment response as soon as the first day after treatment onset and the manifestation of the biomarker strongly depending on the specific treatment regimen the patients received. In summary, this dissertation demonstrates the rich

diversity of information that can be discovered through these imaging techniques. These multiscale imaging modalities can provide a translational platform for discoveries to move from cells to animal and ultimately validation in humans.

TABLE OF CONTENTS

LIST OF TABLES

LIST OF FIGURES

LIST OF ABBREVIATIONS

AC ..... Adriamycin + cyclophosphamide

ACRIN ..... American College of Radiology Imaging Network

APD ..... Avalanche Photodiode

AUC ..... Area under the curve

Bev ..... Bevacizumab

Cb ..... Carboplatin

CPA ..... Cyclophosphamide

CW ..... Continuous Wave

DCIS ..... Ductal Carcinoma in situ

DMD ..... Digital Micromirror Device

DOI ..... Diffuse Optical Imaging

DOSI ..... Diffuse optical spectroscopic imaging

DOT ..... Diffuse optical tomography

DTX ..... Docetaxel

ECM ..... Extracellular Matrix

ETC ..... Electron Transport Chain

FAD ..... Flavin Adenine Dinucleotide

FLIM ..... Fluorescence Lifetime Imaging Microscopy

FLIRR ..... Fluorescence Lifetime Redox Ratio

GEE ..... Generalized estimating equations

HbO2 ..... Oxyhemoglobin

HER2..... Human Epidermal Growth Factor Receptor 2

HHb.....Deoxyhemoglobin

HR.....Hormone Receptor

IDC.....Invasive Ductal Carcinoma

IHC..... Immunohistochemistry

ILC.....Invasive Lobular Carcinoma

INFAR-1 ..... Interferon-□/□ receptor-1

IRF .....Instrument Response Function

ISPY-2.....Investigation of Serial Studies to Predict Your Therapeutic Response through Imaging and Molecular Analysis

LDA ..... Linear Discriminant Analysis

LDH ..... Lipoamide Dehydrogenase

LUT.....Lookup Table

MET .....Metronomic

MPM ..... Multiphoton Microscopy

MTD.....Maximum tolerated dose

NAC .....Neoadjuvant Chemotherapy

NADH .....Nicotinamide Adenine Dinucleotide

NIR.....Near-Infrared

nPTX .....Paclitaxel

NPV..... Negative Predictive Value

NR .....Non-Responders

OXPHOS.....Oxidative Phosphorylation

pCR .....Pathologic Complete Response

PPV .....Positive Predictive Value

PR.....Partial Response

Pzb..... Pertuzumab

ROC .....Receiver Operating Characteristics

ROI.....Region of Interest

RTE..... Radiative Transport Equation

SFDI..... Spatial Frequency Domain Imaging

SHG.....Second Harmonic Generation

StO2 ..... Oxygen Saturation

TCSPC ..... Time-Correlated Single Photon Counter

TNBC.....Triple Negative Breast Cancer

TOI..... Tissue optical index

Tr.....Trastuzumab

VEGR-2 .....Vascular Endothelial Growth Factor Receptor 2

VIS .....Visible

Chapter 1: Breast Cancer Background

1.1 Incidence and Risk Factors

Breast cancer is currently projected to affect 1 in 8 women in the U.S. and an estimated 287,850 cases in 2022 (National Cancer Institute, 2022). It is projected to be responsible for over 40,000 deaths in 2022. This disease primarily affects middle aged and older women with a median age of 63 years old. The long-term survival has decreased steadily over the years primarily thought to be a result of improved screening methodology and novel treatment regimens. A large public health emphasis on the importance of screening has led to an increase in diagnosis of new breast cancer cases over the past 40 years at earlier stages. The diagnosis and treatment of breast cancer at earlier stages can greatly improve patient outcomes.

There are many risk factors for breast cancer such as the BRCA gene, obesity, familial history, and mammography dense breasts. Dense breasts remain one of the strongest, independent risk factors as patients with dense breasts are 4-6x more likely to develop breast cancer than patients with low density breasts (Boyd et al., 1995).

1.2 Pathology and Diagnosis

The breast is made up of three distinct tissue types: lobules, ducts, and connective tissue (NCCN, 2022). The majority of breast tumors start in the ducts (80%) called invasive ductal carcinoma (IDC) or lobules (10%) called invasive lobular carcinoma (ILC) which then invade into the other tissues in the breast. There is an additional form of pre-

cancerous lesions called ductal carcinoma *in situ* (DCIS), in which cancer cells are in the linings of the ducts but have not yet spread to the other parts of the breast.

Breast cancer displays many of same hallmarks as other cancers such as sustained proliferation and resisting cell death (Hanahan & Weinberg, 2011) but it has several specific unique phenotypes. Breast tumors are usually considered to be desmoplastic and have a thick stromal layer surrounding the tumor(Insua-Rodríguez & Oskarsson, 2016). They are also typically considered to be immunologically "cold" compared to other tumor types such as melanoma and lung cancer. Immunotherapies such as checkpoint blockade inhibitors for PD-L1 have been extremely successful in other cancer types but have failed to show as much success in treating breast cancer. Breast tumors are known for having limited T-cell infiltration and generally considered to be immunosuppressive (Vonderheide et al., 2017).

Breast tumors are typically diagnosed by palpation or screening through imaging techniques as mammogram or ultrasound and confirmed by biopsy. At the time of diagnosis, the tumor is also staged. The tumor stage correlates with the prognosis and affects the specific treatment regimens. This staging includes three pieces of information: 1) Size of the primary tumor in the breast, 2) If/How may lymph nodes are involved, and 3) If the cancer has metastasized to distant organs. A larger tumor size, node involvement, and presence of distant metastasis have all been shown to be correlated poorer outcomes (National Cancer Institute, 2022; Sopik & Narod, 2018).

In addition to the tumor staging, another critical factor that has been associated with prognosis and affects treatment regimen is the tumor phenotype (NCCN, 2022). Breast tumors are biopsied to confirm the diagnosis of invasive carcinoma and additionally to characterize the phenotype of tumor cells. They are tested for the presence of estrogen receptor, progesterone receptor, and human epidermal growth factor receptor 2 (HER2). When estrogen or progesterone bind to the corresponding receptor, downstream cellular signaling is activated to promote proliferation. HER2 is a tyrosine kinase receptor and oncogene that promotes a particularly aggressive form of tumors. Patients are also grouped by different subtypes of cancer based on the receptor status. If the tumor is estrogen and/or progesterone positive, they are considered hormone receptor positive (HR+). If the tumor is HER2 positive, then they are considered HER2+. If the tumor is both hormone receptor negative and HER2 negative, it is classified as triple negative breast cancer (TNBC).

1.3 Breast Cancer Treatment

These receptors along with tumor staging dictate what type of treatment a patient may receive (NCCN, 2022). When breast cancer patients receive treatment, it is typically administered in addition to surgery. Adjuvant chemotherapy is when a patient receives surgery first to remove the primary tumor and then receives chemotherapy to kill any residual tumor cells. This is contrast to neoadjuvant chemotherapy (NAC) in which patient first undergoes chemotherapy to shrink the primary tumor and then have surgery

to remove the residual tumor cells. Both treatment options have been shown to have similar long-term outcomes (Asselain et al., 2018). NAC has several advantages compared to adjuvant therapies. NAC allows for the rapid assessment of tumor response to treatment compared to adjuvant therapy which removes the primary tumor and makes it much more difficult to assess success of treatment. Adjuvant therapies typically look at survival metrics over multiple years, compared to NAC which can assess the pathologic state of the tumor post treatment over the course of three to six months. Additionally, NAC can shrink the primary tumor to make inoperable breast tumors operable and improve surgical breast conservation rates (Mieog et al., 2007).

The current preferred chemotherapy regimen is dose-dense doxorubicin (Adriamycin) and cyclophosphamide (AC) followed by sequential dose-dense paclitaxel (NCCN, 2022). These treatment regimens use three cytotoxic agents with distinct mechanisms of action that attacks cells at different points in the cell replication cycle and ultimately helps limit resistance. The dose-dense treatment schedule aims to limit the amount of time the tumor has to continue to proliferate without being exposed to chemotherapy agents (Munzone & Colleoni, 2015). Additionally, depending on the tumor's receptor subtype, patients can receive targeted therapies (NCCN, 2022). For patients that are HR+, they will typically receive endocrine therapy post chemotherapy to inhibit the effects of the hormones inducing recurrence in tumor cells. Patients that are HER2+ will receive a targeted HER2 monoclonal antibody, trastuzumab +/- pertuzumab. Recently for TNBC,

additional targeted therapies such as pembrolizumab for those with PD-L1 positive tumors has been approved (NCCN, 2022).

1.4 Breast Cancer Treatment Response

HER2+ breast cancer is one of the most aggressive forms of breast cancer and had poor outcomes until the development of trastuzumab as a targeted agent (Viani et al., 2007). Now it paradoxically is one of the most aggressive forms of cancer but one that has the one of the best prognoses. Other types of breast cancer such as TNBC are much more difficult to treat and have poorer clinical outcomes (National Cancer Institute, 2022). The deaths from breast cancer are primarily due to treatment resistance that leads to metastasis. The metastasis in critical organs such as the lungs, liver, and brain are ultimately what is responsible for patient deaths and is very difficult to treat. The five-year relative survival rate for patients with cancer localized to the breast is 99.1%, cancer that has spread to lymph nodes is 86.1% and cancer that has distantly metastasized is 30% (National Cancer Institute, 2022). These statistics make it clear that once the cancer metastasizes it often too late and demonstrates the importance of ensuring optimal outcome in the primary tumor at the earliest stages to limit recurrence.

In the current standard of care NAC setting, only about 22% of patients' tumors are completely eradicated with no residual disease, called a pathologic complete response (pCR) (Cortazar et al., 2014). The pCR rate is continuing to improve and certain subtypes such as HER2+ have reported pCR rates greater than 50% (Krystel-Whittemore et al., 2019). pCR patients have excellent long-term outcomes. Patients that have good clinical

outcomes but fail to achieve pCR still achieve some therapeutic benefit and are determined to be a partial response (PR). PR patients additionally benefit from an increase in breast conserving surgeries (Kümmel et al., 2014). This is contrast to patients that have minimal clinical and treatment response are deemed to be non-responders (NR). These patients have the poorest outcomes and the most critical to identify at the earliest stages of treatment (Hamy et al., 2020).

These primary tumors may fail to respond to treatment for a variety of reasons. Cancer resistance pathways can come in a variety of forms such as suppression of apoptotic signaling, alterations in drug metabolism, and increased drug efflux (Alfarouk et al., 2015; Kareva et al., 2015; Nakasone et al., 2012; Sharma et al., 2017). For targeted therapies such as trastuzumab, alterations in the target receptor and expression levels can limit therapeutic efficacy. Cancer cells have many pathways to evade destruction and currently it is difficult to ascertain which patients will fail to respond to specific treatment regimens.

1.4 Breast Cancer Treatment Monitoring

In the NAC setting, it is critical to identify treatment responsive and resistant treatment patients as early as possible since the primary tumor could continue to grow and/or metastasize. The current treatment monitoring strategies in the standard of care are not well suited for longitudinal monitoring and discovery of prognostic biomarkers (Graham et al., 2014).

Physical examination or standard-of-care imaging modalities such as mammography, ultrasound, and MRI provide anatomical information which has shown limited success in predicting response at early timepoints with an agreement with final response respectively of 19%, 26%, 35%, and 71% (Yeh et al., 2005). Tumor anatomical changes often lag behind functional changes, making modalities capable of probing functional characteristic extremely valuable. Functional modalities such as FDG-PET, contrast enhanced MRI, and Magnetic Resonance Spectroscopy have shown improved prognostic ability (Avril et al., 2016; Kaushik et al., 2019; Mclaughlin & Hylton, 2011; Partridge et al., 2018), but these technologies suffer from high cost and/or necessity of contrast agents preventing their use for frequent longitudinal monitoring.

Currently, these treatment monitoring strategies have only been used in investigational studies and have not been established in standard clinical practice, despite a tremendous amount of feedback available for both treatment monitoring as well as in the drug development process. For example, the ISPY-2 (Investigation of Serial Studies to Predict Your Therapeutic Response through Imaging and Molecular Analysis) adaptive trial platform, seeks to integrate as much feedback in the evaluation of a therapeutic regimen (Barker et al., 2009). Specifically, serial MRI images are taken throughout treatment to evaluate the effects of different agents and use that information to inform which patient and tumor characteristics might best be assigned to which treatment. This information will be critical as entirely new categories of treatments such as immunotherapies are developed, which have worked resoundingly well for some types of solid tumors but have only been effective in a small number of breast cancer patients (Emens, 2018).

Importantly, continuous monitoring may be able to help determine which patients are most likely to benefit from experimental treatment plans. While efforts such as the ISPY-2 study may provide a glimpse towards the future of oncology, there is a need for improved technologies that can provide frequent monitoring of treatment efficacy with high accuracy.

Chapter 2: Imaging Modalities and Instrumentation

2.1 Diffuse Optical Imaging

Diffuse Optical Imaging (DOI) is an affordable, non-invasive, and label-free imaging modality that uses near-infrared (NIR) light (600nm-1000nm) at multiple wavelengths to quantify tissue optical properties (Applegate et al., 2020; O'Sullivan et al., 2012). These photons can be modeled through the radiative transport equation (RTE), which describes how the photons propagate through tissue (Haskell et al., 1994). The RTE is very complex to model through heterogenous tissue so most commonly the P1 diffusion approximation is used to simplify the model. The diffuse approximation can be applied to tissues such as the breast, where scattering dominates over absorption. DOI captures photons that have been multiply scattered and is sensitive to both the absorption and scattering properties of the tissue along its path length. Importantly, the continuous wave (CW) implementation is not capable of separating both parameters and typically assumes a scattering parameter to extract the absorption coefficient. The other implementations rely on using either modulating the temporal pulse, temporal modulation frequency, or spatial frequency are all capable of quantifying both absorption and scattering (O'Sullivan et al., 2012). Depending on the specific implementation and imaging parameters, DOI techniques depth sensitivity can range from several millimeters to a few centimeters. The absorption coefficient can be fit to Beer's law to quantify tissue constituents such as concentrations of oxy (HbO_2) and deoxy (HHb) hemoglobin. The reduced scattering coefficient has been shown to track the size and concentration of tissue

components. DOI techniques have extensively been applied to breast cancer to diagnose and track treatment response in both the clinical and preclinical setting.

2.2 Diffuse Optical Spectroscopic Imaging (DOSI)

Diffuse Optical Spectroscopic Imaging (DOSI) is a clinical DOI technique that has been extensively used to monitor breast cancer patients (Tromberg et al., 2008). Specific details about DOSI methodology, instrumentation, and processing have been described elsewhere (Bevilacqua et al., 2000; O'Sullivan et al., 2012). Briefly, the DOSI instrument used in this work utilizes temporally modulated laser diodes (659, 689, 781, 829 nm or 658, 682, 785, 810, 830, 850 nm) and a broadband near-infrared light source (650-1000 nm) to illuminate tissue. The lasers are modulated in temporal frequency from 50-400 MHz. The temporally modulated light is collected by an avalanche photodiode (APD) and the change in signal amplitude and phase were measured with custom electronics, modeled in Figure 2.1 a) in the temporal domain. Prior to measuring subjects, a measurement is taken on a tissue mimicking phantom with known optical properties in order to calibrate the instrument response function.

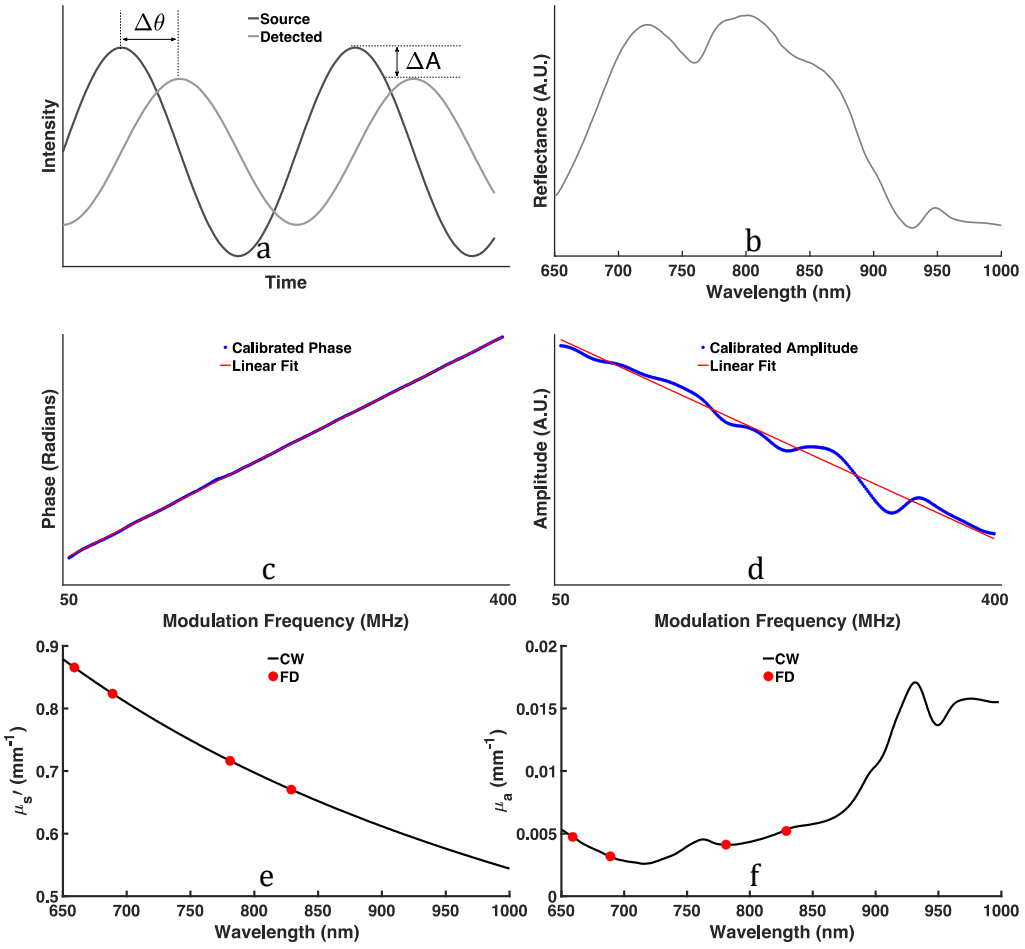

Figure 2.1 a) Model of amplitude and phase changes of temporally modulated light in tissue between the input and detected light. b) Broadband diffuse reflectance from breast tissue in 650-1000 nm. c, d) Calibrated phase delay (c) and amplitude decay (d) measurements across the frequency modulation sweep from 50-400 MHz at 850 nm. e, f) DOSI calculated optical properties of a breast tumor at each frequency domain diode (red) and when combined with the continuous wave measurement, the broadband (black) scattering (e) and absorption (f) from 650-1000 nm.

The amplitude and phase changes at each modulation frequency at each wavelength is fit to the P1 diffusion approximation of the radiative transport equation with the semi-infinite boundary equations in order to calculate the absorption (μ_a) and reduced scattering coefficient (μ_s') at each laser diode (Pham et al., 2000), which is shown in

Figure 2.1 c, d) in red. The scattering values are fit to a power law to extract the normalized scattering amplitude (a) and scattering power (b) and to extrapolate scattering values across the wavelength range of 650-1000 nm, shown in Figure 2.1 e).

$$\mu_s'(\lambda) = a * \left(\frac{\lambda}{\lambda_{800}}\right)^{-b}$$

These scattering values are combined with the broadband diffuse reflectance measurements, shown in Figure 2.1f), to calculate the absorption coefficient from 650-1000 nm. The absorption coefficient is fit to Beer's Law to extract absolute concentrations of oxyhemoglobin (HbO2), deoxyhemoglobin (HHb), water, and lipid. Additional composite metrics can be calculated such as total hemoglobin (THb=HbO2+HHb), oxygen saturation (StO2=HbO2/THb), and tissue optical index (TOI).

2.3 DOSI for Breast Cancer Treatment Monitoring

DOSI has been used in numerous studies seeking to identify prognostic biomarkers at various clinically relevant timepoints (Altoe et al., 2018; A. E. Cerussi et al., 2011; Falou et al., 2014; Gunther et al., 2018; Jakubowski et al., 2004; Jiang et al., 2014; Tank et al., 2020; Tromberg et al., 2016). For example, Ueda *et al.* demonstrated that prior to chemotherapy, elevated tumor oxygen saturation was a powerful predictor of response levels (Ueda et al., 2012). It was hypothesized that non-hypoxic tumors may still have functioning vasculature capable of delivering cytotoxic drugs to the tumor and reflects an increased state of chemo-sensitivity. In a different study, it was shown that responding patients to chemotherapy had an oxyhemoglobin flare, a large increase in oxyhemoglobin on day 1 after the start of treatment, while non-responders had a small decrease (Roblyer

et al., 2011). In responders, this effect was transient and began to decrease on day 3. It was hypothesized that this reaction was an inflammatory response to damage caused by the cytotoxic chemotherapy, which in turned increased local vessel perfusion and corresponding oxyhemoglobin levels. Non-responding patients may have been resistant to cytotoxic chemotherapy or may have had an immunosuppressive environment incapable of generating that inflammatory response. Other studies have investigated the extent of TOI change from baseline to the midpoint and end of treatment (A. E. Cerussi et al., 2011). These studies analyzed a normalized TOI ratio of the tumor in affected breast over a matched location in the contralateral normal breast. This metric serves as an intra-patient normalization metric such that when the value decreases towards 1, it indicates that the tumor area has successfully become more normalized. These changes are attributed to a decrease in pathogenesis of the tumor with a decrease in hypoxia and cellular content, and recovery of normal adipose tissue. Based on these results, the first prospective multi-center clinical trial for optical NAC monitoring was undertaken at seven sites across the country (Tromberg et al., 2016). In this study, the primary endpoint failed to reach statistical significance at midpoint and showed prognostic ability only on a subset of the population. This potentially indicates that, when measuring a diverse population set with a wide variety of treatments, the TOI metric may be insufficient and new optical biomarkers are needed to determine response.

Critically, all prior DOSI studies have included patients receiving heterogenous treatment regimens, representing a major limitation for the field. Different treatment regimen and agents have different mechanisms of action and consequently affect the tumor's

functional and metabolic profile differently. Consequently, this may affect both DOSI derived parameters as well as the timepoint when prognostic biomarkers appear. In Chapter 3 of this dissertation, I describe a clinical DOSI monitoring study where breast cancer patients were monitored throughout the first week of chemotherapy and DOSI parameters were analyzed as a function of their respective treatment regimen.

While treatment remains one confounding variable in search of biomarkers, there is also the patient's physiological features such as age or BMI as well as the tumor staging and subtype. All these potential covariates make it difficult to discover biomarkers, instead; the preclinical setting allows for complete control over these variables.

2.3 Spatial Frequency Domain Imaging (SFDI)

The preclinical setting allows for complete experimental control and isolation of specific mechanisms of interest. DOSI parameters in the clinical setting can be explored and studied in the preclinical setting using a better suited DOI modality: Spatial Frequency Domain Imaging (SFDI). SFDI is the wide-field DOI technique our lab uses to track murine tumor optical properties. Specific details about SFDI methodology, instrumentation, and processing have been described elsewhere (Cuccia et al., 2005, 2009). SFDI projects spatially modulated sinusoidal patterns onto tissue, as shown in Figure 2.2, over a 15x20 cm field of view with VIS (visible) and NIR LEDs to recover the optical absorption (μ_a) and reduced scattering coefficient (μ_s') at each projected wavelength. Different spatial frequencies ranging from 0-0.5 mm^{-1} are projected at each

wavelength with 3 different phase offsets (0°, 120°, and 240°) using a digital micromirror device (DMD). Depending on the specific spatial frequencies and wavelengths used, the depth sensitivity of SFDI typically ranges from 3-5mm.

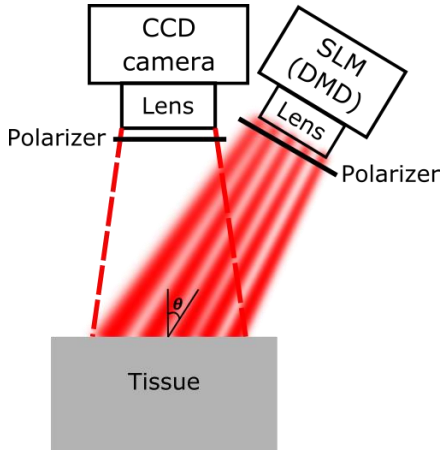

Figure 2.2 Schematic of the SFDI system with spatially modulated light projected into tissue and the diffuse reflectance collection by a CCD camera (Karrobi et al., 2019).

The different phase images are demodulated to extract the modulation amplitude envelope for each wavelength-frequency combination using a previously established method (Cuccia et al., 2009). Prior to tissue measurement, a calibration measurement is taken on a tissue mimicking phantom with known optical parameters to remove the system response and to obtain calibrated diffuse reflectance maps. These measurements can also be calibrated with the use of an in-frame phantom to correct for any drift occurring throughout a measurement day, which may span several hours (Tabassum et al., 2018). The corrected diffuse reflectance value at each pixel can be fit to a two-frequency lookup table (LUT) per wavelength to determine the tissue optical properties. In the case of mouse tumor imaging, our lab has previously developed a LUT using a two

layer Monte Carlo simulation to account for a fixed skin layer optical properties in order to better estimate the underlying tumor optical parameters(Tabassum et al., 2018). A ROI is manually selected over the tumor region using the μ_a map. The ROI is corrected for both height and angle, a necessary requirement due to the irregular, dynamic shape of tumors during longitudinal measurements (Tabassum et al., 2016, 2018; Zhao et al., 2016). Any remaining artifacts in the image are removed such as unphysiological data with extremely low absorption. These corrected ROIs of optical property is then used to calculate the two scattering parameters, *a* and *b*, as well as four absorption-based parameters: HbO_2, HHb, StO_2, and THb. SFDI's ability to rapidly quantify widefield optical properties makes it an ideal tool for research experiments.

2.4 SFDI for treatment monitoring

SFDI has been used for a host of applications (Gioux et al., 2019) in ex-vivo samples such as margin detection in resected breast samples, clinical applications such as burn wound assessment, and most relevant to this work, murine tumor monitoring (Tabassum et al., 2016). The feasibility of preclinical tumor monitoring has been previously established by our lab and demonstrated that SFDI parameters related to scattering correlate with both tumor growth, response, and rebound (Tabassum et al., 2018). Most recently, a comprehensive longitudinal study was undertaken in which a murine prostate cancer model was used to study treatment response zxy. Mice were separated into three treatment categories: untreated control, treatment with a cytotoxic drug: Cyclophosphamide (CPA), and treatment with an antiangiogenic agent: DC101. Cyclophosphamide is a cytotoxic, antineoplastic agent that damages cell's DNA,

preventing replication and inducing apoptosis. Cyclophosphamide is given in the standard-of-care for several cancers and has previously been shown to have synergistic immunomodulatory effects that can lead to a positive treatment response (Roghanian et al., 2019). DC101 is an experimental monoclonal antibody specifically targeting the murine vascular endothelial growth receptor-2 (VEGFR-2). Mice were monitored with SFDI every 2-3 days throughout treatment for 18 days starting with the initiation of treatment. This study demonstrated that the scattering parameters, *a* & *b*, were the most valuable parameters to track changes in tumor volume in the treated cohorts versus the untreated cohort. *a* had been previously shown to track with the density of scatters while *b* has been shown to correlate with the distribution of scattering particle sizes (Hielscher et al., 1997; Mourant et al., 1997). It was hypothesized that the increases in *a* parameter served as an indicator of apoptosis and correlated strongly with IHC apoptosis marker of Cleaved Caspase-3. The *b* parameter was hypothesized to be a surrogate for cell proliferation and was correlated with IHC proliferation marker of PCNA. This study demonstrated the potential for SFDI to be used in the preclinical setting to study tumor response and the ability to validate findings with high molecular specificity techniques such as IHC.

A major limitation in the preclinical setting and with the previous study is the treatment arm are either often compared to an untreated placebo or another treatment arm with a differing mechanism of action. These comparisons do not match the clinical setting where it is critical to discover if patients who receive the same treatment have

heterogenous clinical responses. It is often difficult to develop paired models in which a model either responds or fails to respond to the same treatment. These paired models can help to confirm the validity of the biomarkers as well as improve the chance of translatability to the clinic. In Chapter 4 of this dissertation, I describe a SFDI longitudinal treatment monitoring study conducted on a paired immune responsive-resistant murine breast cancer model

SFDI and more broadly DOI techniques provide optical properties tissue volume averaged optical parameters. Its ease of use combined with the fact that it provides the information in non-invasive, label-free make these techniques extremely attractive. However, the tissue volume averaged make these intrinsically low-resolution and difficult to use to study *in vitro* samples. *in vitro* samples of tumors are typically much smaller than both human and murine breast tumors and the lack of specific physiological elements such as skin enables the use of much higher resolution imaging techniques such as microscopy.

2.5 Multiphoton Microscopy (MPM)

Multiphoton Microscopy (MPM) has been used for a wide range of intravital imaging applications using both exogenous contrast agents and endogenous contrast mechanisms such as second harmonic generation and autofluorescence (Helmchen & Denk, 2005). MPM excitation occurs when multiple (>1) photons interact in a nonlinear process that confines the excitation volume in both the lateral and axial dimensions as shown in Figure 2.3. This allows for intrinsic depth sectioning and collection of 3D imaging sets.

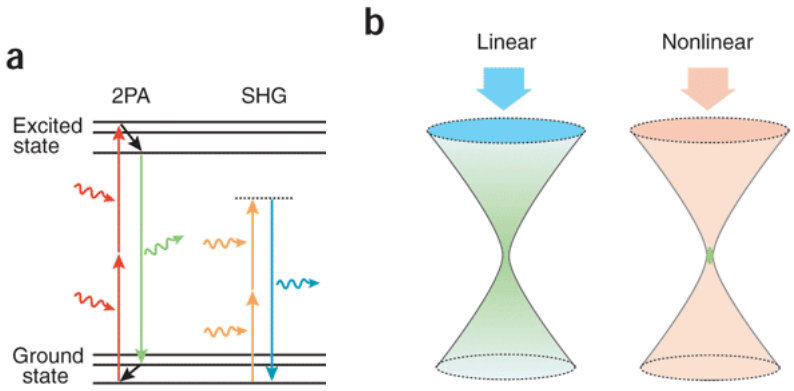

Figure 2.3. a) Jablonski diagram of nonlinear process through which two photon interaction can excite a fluorescent dye or generate a harmonic at a higher frequency. b) Demonstration of differences in excitation volumes between linear and non-linear excitation. Using a single photon, a large cone shape region is excited while with non-linear excitation, the excitation volume is confined to the focal plane (Helmchen & Denk, 2005).

MPM typically uses longer NIR excitation wavelengths (700 -1300 nm) compared to single photon microscopy which typically uses shorter, visible wavelengths. Mie scattering in tissue is represented by an inverse relationship with wavelength, resulting in the longer MPM excitation light scattering less in tissue and being able to resolve images as deep as 1 mm into the brain(Helmchen & Denk, 2005). These features enable MPM to sample deeper than many other high-resolution microscopy techniques, allowing improved in vivo investigations of the brain (Sakadžić et al., 2010) and solid tumors (Walsh et al., 2014).

2.6 Fluorescence Lifetime Imaging (FLIM)

MPM is commonly used to excite exogenous fluorescent dyes, which upon excitation exponentially decays on the order of nanoseconds to the ground state and the time-integrated intensity is measured. There are several endogenous molecules that have autofluorescence such as nicotinamide adenine dinucleotide (NADH) and flavin adenine

dinucleotide (FAD). These co-enzymes exist in either the bound or free state which affects its fluorescence decay rate. A specialized form of MPM, fluorescence lifetime imaging microscopy (FLIM), captures the fluorescence decay of an excited species such as NADH to distinguish between the relative proportion of free and bound NADH. The fluorescence decay can be measured with a time-correlated single photon counter (TCSPC) that has sub nanosecond time resolution. The fluorescence decay of these species can be modeled as a bi-exponential decay with a short lifetime, corresponding to free FAD and bound NADH, and a long lifetime, corresponding to bound FAD and free NADH.

2.7 FLIM Metabolic Contrasts: NADH and FAD

NAHD and FAD are heavily involved in metabolic processes such as oxidative phosphorylation (OXPHOS) and glycolysis (Datta et al., 2020). NADH plays a critical role in mediating mitochondrial respiration by serving as an electron donor in the electron transport chain (ETC), oxidizing NADH to NAD+. NADH is also a main electron acceptor in glycolysis and Krebs cycle, reducing NAD+ to NADH. In its free state, NADH is self-quenching and has a short lifetime. When it interacts with other proteins such as complex 1 in the ETC, the conformational change in the enzyme eliminates the self-quenching feature and has a subsequently longer fluorescence lifetime. FAD is also involved in metabolic redox reactions with $FADH_2$ being oxidized to FAD in complex 2 of the ETC and being reduced from FAD to $FADH_2$ in Krebs cycle. FAD's fluorescence is usually quenched when bound to most proteins and the main FAD bound signal comes from its interaction with lipoamide dehydrogenase (LipDH), which is proportional to the

local NAD+ concentrations. This leads to the fact that increased NADH intensity and bound NADH should correspond to increased OXPHOS and decreased glycolysis. Conversely, increased FAD intensity and bound FAD should correspond to increased glycolysis and decreased OXPHOS.

2.8 Previous FLIM work and validation

FLIM has been used extensively to measure a host of applications such as neuronal populations, cancer cells, solid tumors, and human skin (Bird et al., 2005; Georgakoudi & Quinn, 2012; Z. Liu et al., 2018; Mah et al., 2018; Quinn et al., 2013; Varone et al., 2014; Wallrabe et al., 2018; A. J. Walsh et al., 2013, 2014). These studies determined significant differences in FLIM derived patterns between different disease states These studies independently validated their findings using chemical assays and mass spectrometry and showed that the FLIM parameters correlated with markers of OXPHOS, glycolysis, glucose uptake, and fatty acid synthesis. A FLIM metric that has shown promise and been validated is the fluorescence lifetime redox ratio (FLIRR), which is a composite metric of the ratio of bound NADH to bound FAD (Wallrabe et al., 2018). Larger values corresponded to OXPHOS and lower values correlated with glycolysis. In Chapter 5 of this dissertation, 3D breast cancer spheroids are imaged using FLIM embedded in varying collagen concentrations to determine the relationship between the ECM, cell invasion and metabolism using the FLIRR metric.

Chapter 3: Diffuse optical spectroscopic imaging reveals distinct early breast tumor hemodynamic responses to metronomic and maximum tolerated dose regimens

Background

Breast cancer patients with early stage disease are increasingly administered neoadjuvant chemotherapy (NAC) to downstage their tumors prior to surgery. In this setting, approximately 31% of patients fail to respond to therapy. This demonstrates the need for techniques capable of providing personalized feedback about treatment response at the earliest stages of therapy to identify patients likely to benefit from changing treatment. Diffuse Optical Spectroscopic Imaging (DOSI) has emerged as a promising functional imaging technique for NAC monitoring. DOSI uses non-ionizing near-infrared light to provide non-invasive measures of absolute concentrations of tissue chromophores such as oxyhemoglobin. In 2011 we reported a new DOSI prognostic marker, oxyhemoglobin flare: a transient increase in oxyhemoglobin capable of discriminating NAC responders within the first day of treatment. In this follow up study, DOSI was used to confirm the presence of the flare as well as to investigate whether DOSI markers of NAC response are regimen dependent.

Methods

This dual-center study examined 54 breast tumors receiving NAC measured with DOSI before therapy and the first week following chemotherapy administration. Patients were treated with either a standard of care Maximum Tolerated Dose (MTD) regimen or an investigational Metronomic (MET) regimen. Changes in tumor chromophores were tracked throughout the first week and compared to pathologic response and treatment regimen at specific days utilizing Generalized Estimating Equations (GEE).

Results

Within patients receiving MTD therapy, the oxyhemoglobin flare was confirmed as a prognostic DOSI marker for response appearing as soon as day 1 with post-hoc GEE analysis demonstrating a difference of 48.77% between responders and non-responders ($p<0.0001$). Flare was not observed in patients receiving MET therapy. Within all responding patients, the specific treatment was a significant predictor of day 1 changes in oxyhemoglobin, showing a difference of 39.45% ($p=0.0010$) between patients receiving MTD and MET regimens.

Conclusions

DOSI optical biomarkers are differentially sensitive to MTD and MET regimens at early timepoints suggesting the specific treatment regimen should be considered in future DOSI studies. Additionally, DOSI may help to identify regimen-specific responses in a more personalized manner, potentially providing critical feedback necessary to implement adaptive changes to the treatment strategy.

This work presented in Chapter 3 was published in the journal: *Breast Cancer Research* in 2020 (Tank et al., 2020) with the following authors and corresponding institutions:

Anup Tank[a], Hannah M. Peterson[a], Vivian Pera[a], Syeda Tabassum[b], Anais Leproux[c], Thomas O'Sullivan[d], Eric Jones[e], Howard Cabral[e], Naomi Ko[f], Rita S. Mehta[g], Bruce J. Tromberg[c], Darren Roblyer[a*]

[a]Department of Biomedical Engineering, Boston University, Boston, MA

[b]Department of Electrical Engineering, Boston University, Boston, MA

[c]Beckman Laser Institute and Medical Clinic, University of California, Irvine, Irvine, California

[d]Department of Electrical Engineering, University of Notre Dame, Notre Dame, IN

[e]Department of Biostatistics, Boston University, Boston, MA

[f]Department of Hematology and Medical Oncology, Boston Medical Center, Boston, MA

[g]Department of Medicine, University of California Irvine, Irvine, California

HMP, TO, NK, RSM, BJT, and DR were responsible for study design. HMP, ST, AL, TO, and DR were responsible for the data collection and imaging. AT, VP, AL, and DR were responsible for data processing and image analysis. AT, EJ, HC, and DR were responsible for statistical analysis. AT and DR were responsible for interpretation of data.

3.1 Background

Neoadjuvant chemotherapy (NAC) is an important treatment strategy for breast cancer patients with early-stage disease. NAC is used to downstage primary tumors and its use has led to more breast conserving surgeries (Kümmel et al., 2014). Pathologic complete response (pCR) to NAC, defined as the absence of invasive disease at the time of surgery, has been accepted by the FDA as a surrogate endpoint correlated with clinical benefit (FDA, 2014). The use of pCR as an endpoint in drug studies has the potential benefit of evaluating efficacy much more rapidly than an endpoint of progression free survival or overall survival and has recently led to accelerated approval of pertuzumab for use in HER2 positive breast cancer in the NAC setting (Esserman & DeMichele, 2014). Patients that fail to achieve pCR but have a substantial reduction in tumor size (>50%) also receive therapeutic benefit including a higher rate of breast conserving surgeries (Asselain et al., 2018). The combination of these partial responders (PR) with pCR patients represent the cohort most likely to benefit from NAC. Unfortunately, 31% of patients fail to respond to therapy (Asselain et al., 2018) These are the patients most critical to identify so that their therapy can be altered to avoid ineffective treatment and unwarranted side effects.

The ongoing challenge of highly heterogeneous responses to cancer therapeutics, combined with the increasing array of therapeutic agents and dosing regimens, highlights the importance of tools that can assist oncologists in personalizing, monitoring, and adapting regimens to improve outcomes and limit toxicity. Unfortunately, current

methods to assess treatment response, especially at early stages of treatment, are limited (Graham et al., 2014). Standard of care imaging modalities such as mammography, ultrasound, and MRI provide anatomical information which has shown limited success in predicting response at early timepoints (Hylton et al., 2012; Mclaughlin & Hylton, 2011; Yeh et al., 2005). Functional imaging modalities such as FDG-PET (Avril et al., 2016), contrast enhanced MRI (Partridge et al., 2018), and MRS (Danishada et al., 2010) have often demonstrated both earlier and improved prognostic ability, but these modalities suffer from high cost and/or necessity of contrast agents making them impractical for frequent longitudinal monitoring.

Diffuse Optical Spectroscopic Imaging (DOSI) and Diffuse Optical Tomography (DOT) are emerging as affordable, non-invasive functional imaging modalities for longitudinally monitoring breast tumors during NAC (Gibson & Dehghani, 2009; Tromberg et al., 2008). DOSI uses near-infrared light (650-1000 nm) to interrogate tissue optical absorption and scattering properties up to several centimeters in depth (Bevilacqua et al., 2000; O'Sullivan et al., 2012; Pham et al., 2000). DOSI measures absolute concentrations of oxyhemoglobin, deoxyhemoglobin, lipid, and water. These parameters have been shown by multiple research groups to be valuable prognostic markers at various points throughout NAC (Tromberg et al. 2016; Roblyer et al. 2011; A. E. Cerussi et al. 2011; Falou et al. 2014; Gunther et al. 2018; Ueda et al. 2012; J M Cochran et al. 2017; Sajjadi et al. 2017; Jiang et al. 2014; Ueda et al. 2017; Zhu et al. 2018). For example, a recent landmark multi-center study (ACRIN 6691) showed that changes in tumor

deoxyhemoglobin, water, and lipid at midpoint of NAC correlated strongly to pCR (Tromberg et al., 2016). Additionally, we have previously shown that alterations in tumor oxyhemoglobin during the first day of therapy can discriminate responding from non-responding NAC patients, representing the earliest DOSI marker of treatment response to date (Roblyer et al., 2011).

Importantly, almost all prior treatment monitoring studies with DOSI and DOT have analyzed NAC treatment response irrespective of regimen, representing a substantial limitation in the field. The magnitude of antiangiogenesis, hypoxia, immune activation, and other biological effects induced by systemic therapies are highly dependent on the specific agents and treatment schedules (Bertolini et al., 2003; Kareva et al., 2015; Ueda et al., 2017). Consequently, DOSI and DOT prognostic biomarkers may be highly dependent on the particular agents and schedule. Current standard of care NAC regimens most commonly utilize Maximum Tolerated Dosing (MTD) (NCCN, 2019). MTD is defined as the highest dose that can be administered without unacceptable side effects. This strategy relies on the kinetics of large doses of drug administrations leading to dramatic tumor cytotoxicity, typically followed by a rest period in which the host recovers from off-target effects (Hanahan et al., 2000). In this paradigm, non-responding patients can endure up to several months of severe cytotoxic side effects without any therapeutic benefit. Alternative treatment dosing schedules are currently being explored to both enhance therapeutic efficacy and reduce off target toxicity. Perhaps most importantly, Metronomic (MET) scheduling, which utilizes lower dose agents

administered more frequently, has demonstrated promising anti-angiogenic properties (Kerbel & Kamen, 2004; Pasquier et al., 2010) as well as anti-tumor immune activation while limiting side effects (Kareva et al., 2015; Masuda et al., 2014; Munzone & Colleoni, 2015). There continues to be considerable interest in investigating whether MET regimens can improve response rates and outcomes in breast and other cancers, demonstrated by the dozens of active clinical studies exploring metronomic regimens listed on www.clinicaltrials.gov.

We present here clinical evidence of regimen specific DOSI response during early NAC, demonstrating that the oxyhemoglobin flare, a transient increase in tumor oxyhemoglobin concentration occurring during the first week of NAC, manifests as a powerful prognostic marker in patients receiving an MTD regimen primarily consisting of Adriamycin and cyclophosphamide, but fails to appear in a well-matched MET cohort receiving the cytotoxic chemotherapy agents: carboplatin and paclitaxel with either the targeted agent bevacizumab or trastuzumab. In MTD patients, oxyhemoglobin flare peaked 24 hours following the first chemotherapy infusion, separating the responding and non-responding patients. In contrast, the MET patients displayed very small changes in oxyhemoglobin regardless of response. These differences in the MTD vs MET patients are likely attributable to the differences in treatment regimen including both the treatment agents and dosing. This work highlights the importance of precision treatment monitoring strategies that account for the specific therapeutic regimen.

3.2 Methods

3.2.1 Spectroscopy

Specific details about the DOSI instrumentation have been well described elsewhere (Bevilacqua et al., 2000). Briefly, DOSI uses near-infrared light (650-1000 nm) to measure deep tissue functional information with a handheld probe. For this study, fiber-coupled temporally modulated laser diodes (659, 689, 781, 829 nm or 658, 682, 785, 810, 830, 850 nm) and a broadband near-infrared light source (650-1000 nm) were used to illuminate the tissue from the skin surface. An avalanche photodiode was used to detect the remitted temporally modulated laser light and a spectrometer was used to measure the remitted broadband light. The lasers were frequency swept from 50 to 400 MHz; the amplitude and phase perturbations induced by the tissue were measured with a vector network analyzer or custom analog electronics (No et al., 2008). The amplitude and phase at each wavelength and modulation frequency were fit to an analytical solution to the P1 diffusion approximation of the Boltzmann transport equation solved in the frequency-domain with semi-infinite boundary conditions (Haskell et al., 1994). This information was combined with broadband diffuse reflectance measurements to yield broadband optical absorption and reduced scattering properties (Bevilacqua et al., 2000). Absolute concentrations of oxyhemoglobin (HbO_2), deoxyhemoglobin (HHb), water, and lipid were then determined by a least squares fitting procedure of the broadband absorption spectra to the known extinction coefficient spectra of these four chromophores according to Beer's Law. Additional composite metrics were also computed including total hemoglobin ($THb = HbO_2 + HHb$), Oxygen Saturation ($StO_2 = HbO_2 / THb$), and Tissue Optical Index (TOI=HHb*Water/Lipid). All data analysis was conducted using custom processing codes developed in MATLAB R2014b (MathWorks Inc).

3.2.2 Imaging Procedure

DOSI scans were conducted prior to chemotherapy administration (baseline) and as many days as possible within the first week of starting therapy dependent on patient availability and health status. A standardized DOSI measurement protocol was used to measure the patients (Tromberg et al., 2016). Briefly, a sequential rectangular grid pattern with 1 cm spacing was transferred to the tissue using a transparency and surgical marker. The DOSI probe was placed against the breast and a measurement was taken at every point on the grid. Landmarks such as the nipple, areola, freckles and moles were used to coregister longitudinal measurements. The size of the rectangular grid was chosen to fully include the tumor region with clear margins as determined by prior standard of care imaging and palpation. An example of a measurement grid is shown in Figure 3.1 on the left breast using a 3D bust model. An interpolated heat map of the TOI composite metric in shown over the right breast over a 3.7 cm tumor. The tumor and areola both show significant TOI contrast relative to the surrounding breast tissue, a highly conserved feature seen across many breast cancer subjects (A. Cerussi et al., 2006).

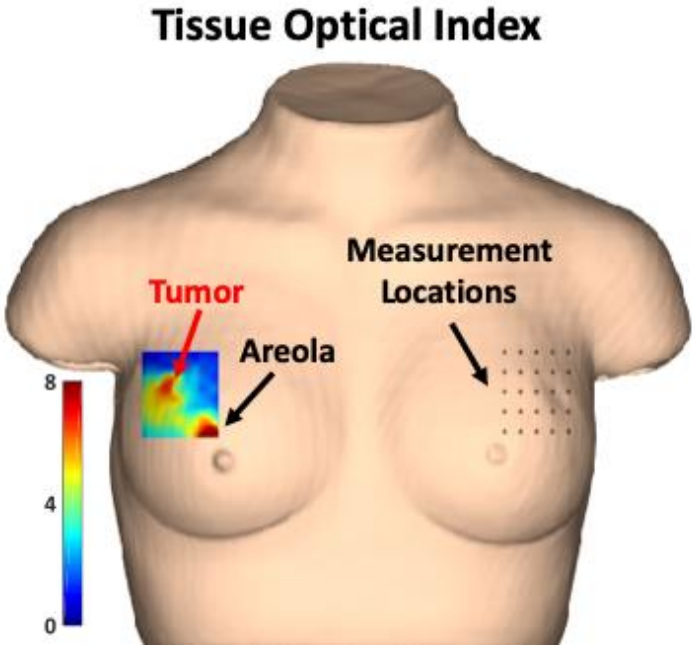

Figure 3.1 Bust model of DOSI measurement. Example of DOSI measurement grid locations (right) and subsequent TOI map (left) demonstrating tumor and areolar contrast.

3.2.3 Image Analysis

2D heat maps of each chromophore (i.e. HbO_2, HHb, water, lipid) and composite metrics (i.e. THb, StO_2, TOI) were generated for each subject and at each time point. A tumor region of interest (ROI) was determined using a combination of peak TOI contrast, as described by previous studies (A. Cerussi et al., 2006; A. E. Cerussi et al., 2011; Tromberg et al., 2016), and tumor size was determined by ultrasound or MRI. The tumor ROI size remained constant throughout the longitudinal measurements but was allowed to laterally shift in cases of grid displacement. Tumor chromophore concentrations were calculated by taking the mean over the tumor ROI.

3.2.4 Subject Eligibility and Enrollment

53 female breast cancer patients were measured at Boston Medical Center (BMC) and University of California, Irvine (UCI) from May 2004 to October 2017. Subject's ages ranged from 26 to 71. One patient had bilateral breast cancer with both tumors measured for a total of 54 DOSI monitored tumors. Eligible subjects had a diagnosis of invasive breast cancer and were planned for neoadjuvant cytotoxic chemotherapy with definitive breast surgery following therapy. Each patient's treatment regimen was determined by their oncologist; a subset of subjects was simultaneously enrolled in an investigational protocol testing MET dosing and scheduling (Clinicaltrials.gov Identifier NCT00618657). The patients received a biopsy prior to treatment to confirm invasive cancer diagnosis, which provided the tumor receptor status (i.e. ER, PR, HER2). Potential subjects were excluded if they were pregnant or previously received treatment to the affected breast. Data from a portion of these 54 subjects had been used in prior published works, including the initial observation of oxyhemoglobin flare (Roblyer et al., 2011), which analyzed 24 of the current 54 subjects throughout week 1, including Day 1. The remaining 30 subjects' data at Day 1 have not been published before, although 14 of the current 54 subjects were also enrolled in the ACRIN 6691 study (Tromberg et al. 2016; Jeffrey M. Cochran et al. 2018), which included baseline, early (days 5-10), midpoint, and pre-surgical timepoint measurements. All patients provided written informed consent. This project was approved by the Institution Review Board at Boston University, Boston Medical Center and UCI.

3.2.5 Histopathology

Each patient's resected tumor was evaluated by the local institution's pathologist to generate a pathology report. After treatment, the patient was assigned a tertiary response status according to the National Surgical Adjuvant Breast and Bowel Project Protocol (Rastogi et al., 2008): pathologic complete response (pCR), partial response (PR), and no response (NR). pCR was defined as no residual tumor burden in resected tumor. PR was defined as a decrease in the largest tumor dimension by >50% from diagnosis to resection while NR was defined as a decrease of <50%. A binary classification of response was also utilized in which Responders, defined as subjects achieving either pCR or PR, were compared against NR subjects.

3.2.6 Statistical Analysis

Generalized Estimating Equations (GEE) were used to longitudinally model the DOSI chromophores throughout the first week after chemotherapy utilizing SAS (SAS Institute) (Littell et al., 1991). The GEE accounted for the correlation between multiple measurements on a single patient and allowed for an unbalanced dataset with subjects considered as clusters, an exchangeable correlation structure, and a normal model with an identity link function. Separate models were run each of four chromophores: HbO_2, HHb, Water and Lipid. In addition, for each outcome variable, three separate models were run on population stratifications of treatment schedule and pathologic response to isolate the effects of specific covariates and interaction terms: 1. MTD Responders vs MTD Non-Responders, 2. MET Responders vs MET Non-Responders, and 3. MTD Responders vs

MET Responders. Additional covariates included in these models included: institution (Boston Medical Center vs UC Irvine), age, hormone receptor status (estrogen receptor or progesterone receptor), and HER2 status. Significance for model parameters was determined at a level of 0.05 and when adjusted for multiple comparisons with Bonferroni correction at a level of 0.0125. Additional covariates relating to treatment such as chemotherapeutic agent or drug mechanism were not included as these parameters were highly correlated with treatment schedule (e.g. all patients administered Adriamycin + Cyclophosphamide received an MTD schedule). Post hoc contrasts between outcome means adjusted for covariates in the statistical models were performed at each day post chemotherapy between strata of interest: 1.) MTD: Responders vs Non-Responders and 2.) Responders: MTD vs MET. Significance for post hoc contrasts, when adjusted for multiple comparisons with Bonferroni correction, was determined at a level of 0.0036.

Linear Discriminant Analysis (LDA) was preformed using MATLAB to assess the prognostic accuracy of percent change in oxyhemoglobin on day 1 among MTD and MET population. This analysis assumed multivariate normal densities and equal covariance for each group. 5-fold cross-validation was used to train and test the dataset and limit overfitting. We note that there was approximately twice as many responders as non-responders in the MTD cohort and no efforts were made to account for this imbalance in the classification analysis. Posterior probabilities were calculated for each subject from the linear classification of Responders from Non-Responders. Receiver

operating characteristic (ROC) curves were generated by iterating through all posterior probability thresholds. The area under the curve (AUC) of the ROC curve was utilized to evaluate the performance of the model along with the optimal Sensitivity, Specificity, Positive Predictive Value (PPV), and Negative Predictive Value (NPV).

3.3 Results

3.3.1 Subject and Treatment Characteristics

The characteristics of all analyzed subjects are shown in Table 1, which shows the overall population (n=54) statistics as well as characteristics stratified by treatment schedule: Maximum Tolerated Dose (MTD, n=35) and Metronomic (MET, n=19). The MTD patients received treatment every 2 or 3 weeks at the highest dose without unacceptable side effects per the standard of care. In contrast, MET patients received treatment every week at a smaller dose than MTD. The average overall subject age was 49.9 ± 11.1 years with a slightly higher age among the MTD subset, 51.3 ± 11.1 years and slightly lower in MET subset, 47.4 ± 10.8 years. The average tumor size was 3.5 ± 1.7 cm for all subjects, 3.8 ± 1.9 cm for MTD subjects, and with 3.0 ± 1.3 cm MET subjects. Age and tumor size were not significantly different ($p>0.05$) between the MTD and MET cohort through the Wilcoxon rank sum test using MATLAB, utilizing a nonparametric test to avoid any assumptions of the underlying distributions.

All patients received a diagnosis of invasive carcinoma with the majority of patients (91%) receiving a diagnosis of Invasive Ductal Carcinoma (IDC). 65% of subjects had hormone receptor-positive tumors. 15 subjects were diagnosed with HER2 positive tumors, of those

7 received Trastuzumab (Tr) as part of their first neoadjuvant treatment and the other 8 received Tr at a timepoint which was not in the scope of this study. Within the MTD treatment schedule, one patient received a combination of HER2 targeted therapies with both Tr and Pertuzumab (Pzb) along with the cytotoxic agent Docetaxel (DTX). One MTD patient received a combination of Carboplatin (Cb), DTX, and Tr. Three MTD patients received Adriamycin (A) + Cyclophosphamide (C) + DTX, while 30 MTD patients received A+C, which is the current standard of care therapy. Among the MET patients, 14 patients received Carboplatin (Cb) + Paclitaxel (nPTX) + Bevacizumab (Bev) and 5 patients received Cb + nPTX + Tr.

At the time of surgery, 35 patients (65%) were determined to be Responders while 19 patients (35%) were Non-Responders. 71% of MTD patients were Responders (n=25) and 53% of MET patients were Responders (n=10). All proportions (Location, Histology, Receptor Status, and Pathologic Response) were not significantly different between MTD and MET cohorts ($p>0.05$) using the Z-Test for Proportions implemented in MATLAB.

Subject and Tumor Characteristics

Variables	Treatment Cohorts		
	Maximum Tolerable Dose (n=35)	Metronomic Dose (n=19)	Overall (n=54)
Age (years)			
Mean ± SD	51.3 ± 11.1	47.4 ± 10.8	49.9 ± 11.1
Tumor Size (cm)			
Mean ± SD	3.8 ± 1.9	3.0 ± 1.3	3.5 ± 1.7
Location			
Left	15 (43%)	10 (53%)	25 (46%)
Right	20 (57%)	9 (47%)	29 (54%)
Histology			
IDC	31 (89%)	18 (95%)	49 (91%)
ILC	4 (11%)	1 (5%)	5 (9%)
Receptor Status			
ER			
-	13 (37%)	5 (26%)	18 (33%)
+	21 (60%)	14 (74%)	35 (65%)
PR			
-	15 (42%)	8 (42%)	23 (43%)
+	19 (54%)	11 (58%)	30 (56%)
HER2			
-	24 (69%)	14 (74%)	38 (70%)
+	10 (29%)	5 (26%)	15 (28%)
Unknown Receptor (ER,PR,HER2)	1 (2%)	0	1 (2%)
Pathologic Response			
Complete Response	10 (29%)	5 (26%)	15 (28%)
Partial Response	15 (43%)	5 (26%)	20 (37%)
No Response	10 (29%)	9 (47%)	19 (35%)
Treatment			
AC	30 (86%)	0	30 (56%)
AC+DTX	3 (9%)	0	3 (6%)
Cb+DTX+Tr	1 (3%)	0	1 (2%)
Cb+nPTX+Bev	0	14 (74%)	14 (26%)

Cb+nPTX+Tr	0	5 (26%)	5 (9%)
Pzb+DTX+Tr	1 (3%)	0	1 (2%)
Institute			
UC Irvine	29 (83%)	19 (100%)	48 (89%)
Boston Medical Center	6 (17%)	0	6 (11%)

Table 3-1: Table outlining the subject and tumors characteristics, pathology, and treatment. Abbreviations: IDC, Invasive Ductal Carcinoma; ILC, Invasive Lobular Carcinoma; ER, Estrogen Receptor; PR, Progesterone Receptor; HER2, Human Epidermal Growth Factor Receptor 2; AC, Adriamycin and Cyclophosphamide; DTX, Docetaxel; Cb, Carboplatin; Tr, Trastuzumab; nPTX, Paclitaxel; Bev, Bevacizumab; Pzb, Pertuzumab

3.3.2 DOSI reveals response and regimen dependent HbO2 changes on day 1 of NAC

The percent change from baseline was examined to normalize for varying baseline tumor chromophore concentrations among patients, with a focus on the primary aim of day 1 post chemotherapy changes. The observed changes across week 1 are shown in Figure 3.2. For subjects receiving MTD treatment, the largest difference between Responders and Non-Responders occurred on day 1. Responders on day 1 demonstrated a mean 40% increase in HbO2 at day 1 compared to a 13% decrease in Non-Responders. All MET subjects displayed much smaller changes on day 1: Responders with a 3% increase and Non-Responders with a 1% decrease. These differences are visualized in Figure 3.3, which shows representative 2D DOSI heatmaps of HbO2 concentrations at both baseline and day 1 for two different pCR subjects, one of whom received MTD treatment while the other received MET therapy. The MTD patient had a large increase of 50% in HbO2 from baseline to day 1 contrasted with the MET patient, which only increased by 0.3%.

In addition, there were relatively small changes in both MET Responders and Non-Responders across the entire week 1 as compared to the MTD patients.

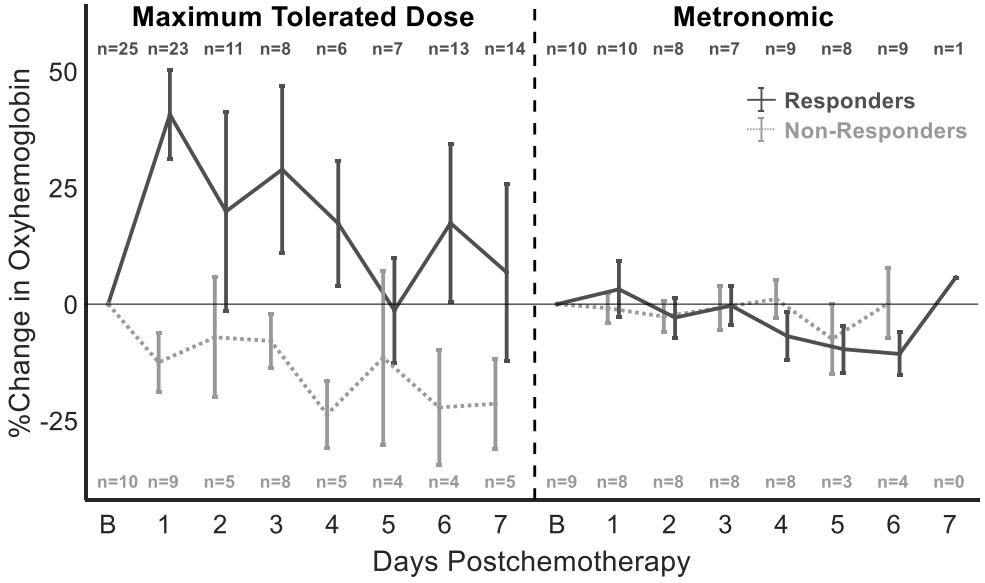

Figure 3.2 Week 1 Postchemotherapy changes of DOSI-monitored tumors. Percent change in oxyhemoglobin during the first week postchemotherapy separated by treatment: Maximum Tolerated Dose (Left) and Metronomic (Right) and pathologic response: Responders (Dark Grey, solid line) and Non-Responders (Light Grey, dashed). At day 1, MTD Responders and Non-Responders are significantly different ($p<0.0001$), while MET subjects fail to demonstrate a statistical difference. Number of subjects measured at each timepoint is indicated and color-coded for pathologic response. Error bars indicate mean ± standard error.

Separate GEE models were fit for the MTD and MET subject populations to isolate the effect of treatment and evaluate the effects of age, institution, hormone receptor status, HER2 status, days post chemotherapy, response, and the corresponding interaction terms. Within the MTD cohort, the interaction term of response and day 1 was a significant predictor of HbO_2 ($p<0.0001$) while the MET cohort failed to demonstrate a statistically significant predictor. In order to isolate the effect of pathologic response, a separate GEE

model was run on the Responder population to determine the effects of age, institution, hormone receptor status, HER2 status, days post chemotherapy, treatment schedule, and the corresponding interaction terms. The interaction term of treatment schedule and day 1 was a significant predictor of HbO_2 ($p=.0008$) in Responders. Post-hoc analysis of outcome adjusted estimates to compare the effect of treatment demonstrated a significant difference in day 1 HbO_2 changes between MTD Responders and MET Responders (39.45+/- 11.98%, $p=0.0010$) seen in Table S3.1A. Similar analysis on the efficacy of HbO_2 as a prognostic biomarker at day 1 for patients receiving MTD demonstrated a difference of 48.77 +/- 9.51 % ($p<0.0001$) between Responders and Non-Responders seen in Table S3.1B. None of the additional covariates (age, institution, hormone receptor status, HER2 receptor status) contributed significantly to the model.

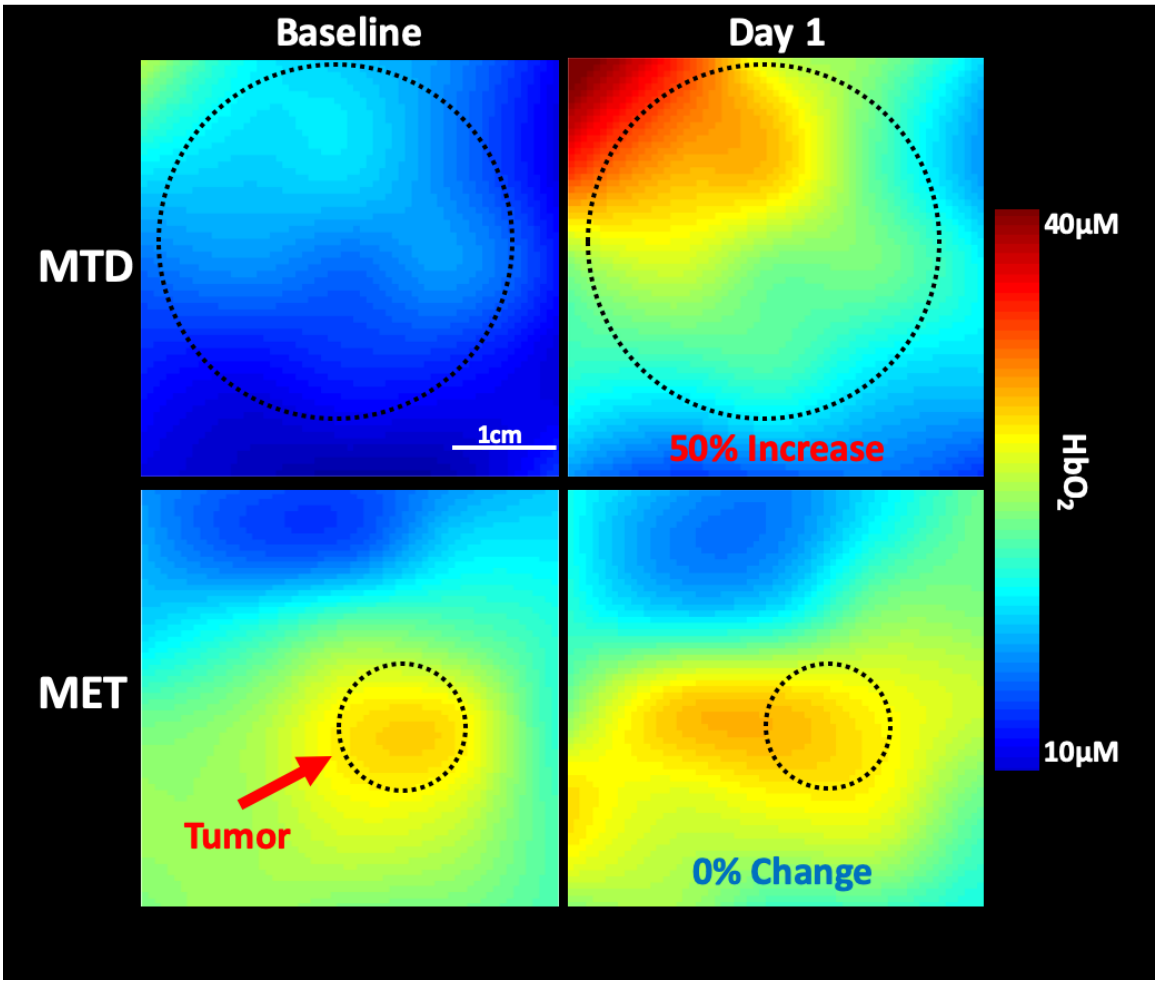

Figure 3.3 Map of oxyhemoglobin flare and regimen specific response. Interpolated HbO_2 maps at baseline (left column) and day 1 (right column) for two pathologic complete responder patients receiving Maximum Tolerated Dose (top) and Metronomic (bottom). The tumor region is indicated by the dashed circle with the scale bar indicating 1 cm. The percent change from baseline for the entire tumor region is indicated in the day 1 column showing oxyhemoglobin flare in MTD patient while MET patient showed almost no change.

Separate LDAs were run on the MTD and MET subject populations to evaluate HbO2 performance on day 1 as a prognostic predictor when isolating the effect of treatment, results shown in Figure S3.1. The MTD cohort had an AUC of 0.89, sensitivity of 0.91, specificity of 0.89, PPV of 0.95 and NPV of 0.80. In stark contrast, the MET cohort had an AUC of 0.50, sensitivity of 0.50, specificity of 0.75, PPV of 0.71, and NPV of 0.55.

DOSI measured changes in HHb, Water, and Lipid throughout week 1 of NAC

HHb, Water, and Lipid did not exhibit significant prognostic or regimen dependent changes in either MTD or MET patients. GEE analysis was run on these chromophores for each of the three population stratifications and there were no significant interactions of treatment or response at any day. The most notable interaction term was response and day 1 post chemotherapy ($p=0.0136$) for water in MTD patients, which came close to significance ($p<0.0125$ for Bonferroni correction). At this timepoint, non-responding MTD patients had a moderate decrease in water concentration compared to responders (Figure S3.2).

3.4 Discussion

Early prediction of NAC response would provide important feedback to alter the therapeutic regimen for each individual patient. We have demonstrated here that early DOS imaging markers are dependent on the specific NAC regimen administered. Specifically, MTD and MET regimens resulted in significantly different oxyhemoglobin responses throughout week 1 of NAC. Oxyhemoglobin flare, a previously reported prognostic biomarker for therapy response, manifested only in MTD treated breast tumors, while MET treatment yielded almost no hemodynamic changes across throughout week 1, regardless of response.

There have been few clinical monitoring studies of breast cancer patients at the earliest timepoints of neoadjuvant chemotherapy. Clinical studies utilizing Magnetic Resonance

Spectroscopy (Meisamy et al., 2004) and FDG-PET (Dehdashti et al., 2009) have previously observed a prognostic metabolic change within one day of therapy. The authors of the MRS study hypothesized that responding tumors receiving AC treatment underwent cytotoxicity and/or decreases in tumor proliferation at day 1, while the authors of the FDG-PET study demonstrated increased metabolic activity in responsive tumors on day 1. Our group has previously demonstrated the presence of the oxyhemoglobin flare on day 1, which provided discriminating of responders from non-responders in a cohort of 24 subjects, 21 of whom received MTD regimens (Roblyer et al., 2011). The present study included data from these prior subjects with the addition of 14 additional MTD subjects and 16 additional MET subjects. 11 new/previously unpublished MTD patients were measured on Day 1, of which 3/5 Responders displayed flare and 5/6 Non-Responders did not display flare (no increase in oxyhemoglobin). This lends some evidence to the prognostic ability of oxyhemoglobin flare as these new patients were measured at different institutions: UC Irvine and Boston Medical Center with different treating oncologists but given the limited new MTD subjects (n=11), we cannot validate flare as a prognostic biomarker in this publication.

Most strikingly, the oxyhemoglobin flare was only present in the subjects who received an MTD regimen, failing to manifest in subjects treated with a MET regimen and serving as a poor predictor of response with an AUC of 0.50 compared to AUC of 0.89 in MTD patients. In MET subjects, only small (<11%) changes in oxyhemoglobin were observed across the entire week 1 of therapy and no prognostic changes occurred in any of the

other hemodynamic parameters including deoxyhemoglobin, total hemoglobin, and oxygen saturation. The presence of oxyhemoglobin flare in responding MTD subjects, and a lack of hemodynamic response in both non-responding MTD subjects and all MET subjects suggests a distinct physiological reaction in responding MTD patients. A rise in oxyhemoglobin may occur due to either a decrease in tumor oxygen demand or an increase in tumor oxygen supply. Subjects that experienced flare had a relatively small change in deoxyhemoglobin leading to an increase in total hemoglobin and oxygen saturation (Figure S3.2), indicating an increase in oxygen supply. This would be consistent with the increased perfusion known to co-occur with an inflammatory response to cytotoxic cellular damage (Bracci et al., 2014; Grivennikov et al., 2010; Hendry et al., 2016; Martin et al., 2019; Newton & Dixit, 2012; Wanderley et al., 2018). The lack of oxyhemoglobin flare in MTD NR patients may indicate poor chemo- and/or immuno-responsiveness, leading to minimal shrinkage of the tumor and potentially poorer outcomes (Dieci et al., 2018; Hanahan & Weinberg, 2011).

MET therapy is characterized by the administration of lower dosage therapy with increased frequency. In this study, the low initial dose may have been insufficient to induce oxyhemoglobin flare, even in subjects who went on to achieve partial or complete responses. Additionally, MET regimens have been shown to exhibit substantially different anti-angiogenic and immunomodulatory effects compared to MTD (Bertolini et al., 2003; Chen et al., 2015; Doloff & Waxman, 2012; Hanahan et al., 2000; Kareva et al., 2015; Munzone & Colleoni, 2015; Pasquier et al., 2010). Additionally, 14 of the 19

MET subjects received the VEGF-A targeting drug Bevacizumab in addition to cytotoxic therapies. Clinical administration of bevacizumab as a monotherapy has been shown to cause hypoxia and decreased total hemoglobin on day 1 when measured with a time-domain diffuse optical system (Ueda et al., 2017). It is possible the administration of bevacizumab inhibited oxyhemoglobin flare in responding MET subjects. Notably, several other publications (A. E. Cerussi et al. 2011; Tromberg et al. 2016; Ueda et al. 2012; Jeffrey M. Cochran et al. 2018) included subjects enrolled in the same investigational MET trial, although the DOSI measurement timepoints investigated in these studies did not include day 1 measurements.

This retrospective study did not control for chemotherapeutic agents as patients across and in the MTD and MET cohorts received different agents as well as scheduling and dosing. The standard of care for NAC allows for flexibility in the order of agents and the exact regimen, determined by the oncologist. This further demonstrates the necessity to account for all aspects of the treatment regimen when investigating prognostic biomarkers. Within the MTD cohort, most patients received AC, however; some received additional DTX, representing a potential confounding variable. In the MET cohort, patients received different cytotoxic chemotherapy agents: Cb and nPTX compared to the MTD cohort receiving AC. These different chemotherapy agents have different mechanisms of actions as carboplatin and cyclophosphamide are both DNA alkylating agents that intercalates in DNA and prevents DNA replication, while adriamycin is a topoisomerase II inhibitor that interferes with DNA repair, and paclitaxel and docetaxel

are a microtubule-stabilizing agent that leads to cell cycle arrest and apoptosis (Abotaleb et al., 2018). Additionally, all MET patients were given a targeted agent, either Bev or Tr which have very different mechanisms of action compared to the other cytotoxic agents. The combination of different agents and dosing strategies may yield different synergistic mechanisms of action, ultimately differentially affecting the tumor and induction of the oxyhemoglobin flare.

Secondary methods may be necessary to confirm the exact biological origins of the flare through inflammatory and immune markers. Additional potential future analysis steps include a Z-score analysis like that conducted by Cochran et al in their analysis of DOSI measurements at early timepoints (within days 5-10 of the start of treatment), as well as determining if treatment schedule plays a significant factor at later DOSI measurement timepoints (Jeffrey M. Cochran et al. 2018).

3.5 Conclusion

In summary, we have demonstrated regimen-dependent hemodynamic responses during week 1 of NAC. Oxyhemoglobin flare manifested as a prognostic marker only in an MTD cohort and not in a MET cohort. This is important as DOSI and DOT treatment monitoring studies have traditionally aggregated subjects irrespective of treatment, while different regimens have markedly different biological mechanisms of action. Early regimen-specific DOSI prognostic markers could be critical for improving patient outcome by identifying non-responders and adapting therapy accordingly. DOSI may

also provide valuable feedback of investigational drug regimens and their proposed mechanisms of action.

3.6 Acknowledgements

The authors thank Elizabeth Pottier, Amanda Durkin, Brian Hill, Montana Compton, Erin Sullivan, and Ylenia Santoro for assistance in patient measurements, coordination, and engineering. The authors thank the patients that graciously volunteered their time to participate in this study.

3.7 Supplementary Information

Responders Cohort: MTD vs MET

Days Postchemotherapy	Difference Estimate %HbO2	Standard Error	Z value	P Value
1	39.4548	11.9849	3.29	0.001
2	27.6914	15.5288	1.78	0.0745
3	45.1494	15.8659	2.85	0.044
4	29.1872	14.0117	2.08	0.0372
5	18.733	12.8497	1.46	0.1449
6	27.1901	14.8437	1.83	0.067
7	9.7234	15.4755	0.63	0.5298

Table S3.1A) Post-hoc GEE Estimates of Oxyhemoglobin differences across Treatment of Responding patients on days 1-7. Significance is determined at Bonferroni corrected level of $p<0.0036$.

MTD Cohort: Responders vs Non-Responders

Days Postchemotherapy	Difference Estimate %HbO2	Standard Error	Z value	P Value
1	48.7737	9.5129	5.13	<.0001
2	28.8053	14.3329	2.01	0.0059
3	48.897	15.0479	3.25	0.0012
4	38.9028	12.8756	3.02	0.0025
5	19.6682	16.6273	1.18	0.2369
6	38.1247	13.3738	2.85	0.044
7	25.3257	13.3915	1.89	0.0586

Table S3.1B) Post-hoc GEE Estimates of Oxyhemoglobin differences across Response of MTD patients on days 1-7. Significance is determined at Bonferroni corrected level of p<0.0036.

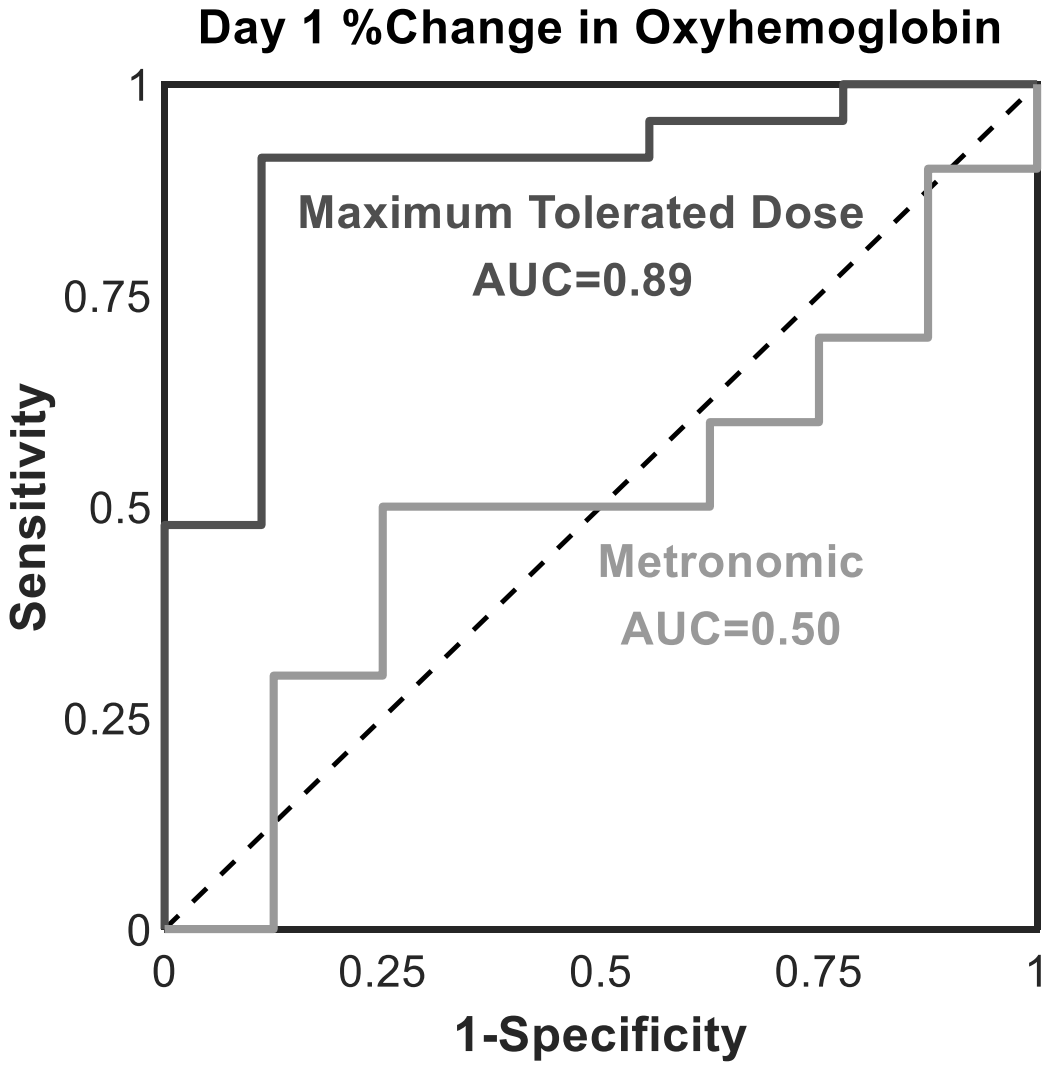

Figure S3.1 Prognostic Accuracy of Oxyhemoglobin Flare. Receiver Operator Characteristic (ROC) Curve of percent change in oxyhemoglobin on day 1 postchemotherapy as a classifier for pathologic response (Responders vs Non-Responders) for both MTD (dark grey) and MET (light grey) with their corresponding area under the curve (AUC).

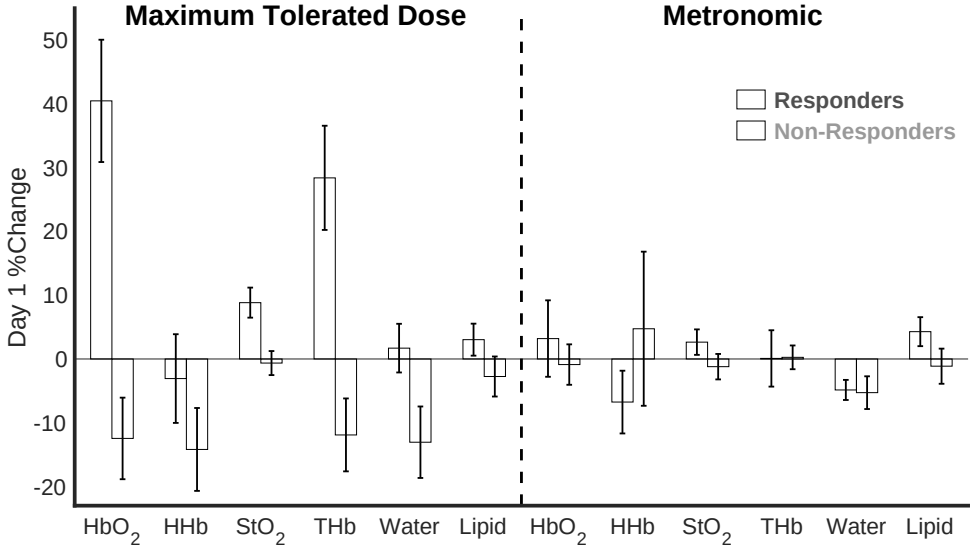

Figure S3.2. Day 1 Changes of DOSI-monitored tumors. Percent change during day 1 postchemotherapy in oxyhemoglobin, deoxyhemoglobin, oxygen saturation, total hemoglobin, water, and lipid separated by treatment: Maximum Tolerated Dose (left) and Metronomic (right) and pathologic response: Responders (Dark Grey) and Non-Responders (Light Grey). Error bars represent mean ± standard error.

Chapter 4: Spatial frequency domain imaging for monitoring immune-mediated chemotherapy treatment response and resistance in a murine breast cancer model

Spatial Frequency Domain Imaging (SFDI) can provide longitudinal, label-free, and widefield hemodynamic and scattering measurements of murine tumors in vivo. Our previous work has shown that the reduced scattering coefficient (μ_s') at 800 nm, as well as the wavelength dependence of scattering, both have prognostic value in tracking apoptosis and proliferation during treatment with anti-cancer therapies. However, there is limited work in validating these optical biomarkers in clinically relevant tumor models that manifest specific treatment resistance mechanisms that mimic the clinical setting. It was recently demonstrated that metronomic dosing of cyclophosphamide induces a strong anti-tumor immune response and tumor volume reduction in the E0771 murine breast cancer model. This immune activation mechanism can be blocked with an IFNAR-1 antibody, leading to treatment resistance. Here we present a longitudinal study utilizing SFDI to monitor this paired responsive-resistant model for up to 30 days of drug treatment. Mice receiving the immune modulatory metronomic cyclophosphamide schedule had a significant increase in tumor optical scattering compared to mice receiving cyclophosphamide in combination with the IFNAR-1antibody (9% increase vs 10% decrease on day 5 of treatment, $p<0.001$). The magnitude of these differences increased throughout the duration of treatment. Additionally, scattering changes on day 4

of treatment could discriminate responsive versus resistant tumors with an accuracy of 78%, while tumor volume had an accuracy of only 52%. These results validate optical scattering as a promising prognostic biomarker that can discriminate between treatment responsive and resistant tumor models.

This work presented in Chapter 4 was published in *Scientific Reports* in 2022(Tank et al., 2022) with following authors and corresponding institutions.

Anup Tank[a], Cameron Vergato[b], David J. Waxman[b], Darren Roblyer[a]*

[a] Biomedical Engineering, Boston University, Boston, MA, USA

[b]Department of Biology and Bioinformatics Program, Boston University, Boston, MA, USA

A.T. and C.V. were responsible for mice experiments. A.T. was responsible for mouse imaging. A.T. was responsible for data processing, image processing, and statistical analysis. A.T. and D.R. were responsible for interpretation of data. A.T. and D.R. wrote the manuscript with assistance from the other authors.

4.1 Introduction

The preclinical setting allows for the exploration of new anti-cancer therapies while investigating specific treatment response and resistance mechanisms, providing valuable insight for clinical translation(Ireson et al., 2019). Preclinical imaging of intra-tumoral functional and metabolic changes induced by chemotherapy and immunotherapy can provide critical information regarding the tumor response and help identify improved treatment regimens and new methods for clinical treatment monitoring(O'Farrell et al., 2013). Recently, a label-free optical imaging technique called Spatial Frequency Domain Imaging (SFDI) has been introduced for preclinical tumor treatment monitoring (Tabassum et al., 2021). SFDI uses spatially modulated near infrared light to provide non-invasive and wide-field measurements of optical absorption and scattering properties(Cuccia et al., 2009). Optical scattering is sensitive to cellular and tissue microarchitecture while absorption is sensitive to tissue concentrations of oxy- and deoxyhemoglobin, which are related to both hypoxia and angiogenesis(Hoiland et al., 2016). SFDI has several distinct advantages over other preclinical imaging modalities. For example, it is uniquely capable of providing non-invasive, contact-free, label-free and widefield optical absorption and scattering maps of tissue. In comparison, microscopy-based intravital imaging methods, such as confocal or multiphoton microscopy, have improved spatial resolution (1-10 μm vs 500 μm for SFDI) but with limited penetration depth (~1 mm vs 5 mm for SFDI) and often require the addition of contrast agents(Perrin et al., 2020). Photoacoustic Imaging, which has much deeper penetration (up to several centimeters), is insensitive to scattering changes in tissue(Beard, 2011). Fluorescence and

bioluminescence imaging can provide deep tissue imaging but require exogenous imaging agents or genetically modified animal models, and cannot quantify scattering(Kosaka et al., 2009)

Our group has recently advanced SFDI for preclinical oncology imaging and has established optical scattering as a promising biomarker of drug treatment responses (Karrobi et al., 2019; Tabassum et al., 2016, 2018, 2021a; Zhao et al., 2016). We showed that optical scattering was strongly associated with apoptosis and decreased proliferation induced by cytotoxic and antiangiogenic therapies in murine breast and prostate tumors (Tabassum et al., 2021). Scattering amplitude was positively correlated with cleaved caspase-3, an IHC marker for apoptosis, and increased over time in response to treatment. Additionally, scattering power, which represents the wavelength dependence of scattering, was negatively correlated with PCNA, an IHC marker for proliferation, and decreased over time following treatment. However, an important limitation of this prior work is that the changes in the treated tumors were only compared to untreated controls. This does not adequately reflect the clinical setting in which all patients are treated (i.e., there are no untreated controls). In order to better mimic the clinical setting, models are needed that accurately recapitulate treatment resistance. Examining optical changes in the context of specific resistance mechanisms would then help validate optical scattering as a relevant imaging biomarker and increase the likelihood of the translatability to the clinical setting.

To accomplish this, we imaged a paired responsive resistance breast tumor model developed by our group (Vergato et al., 2021). In this model, metronomic dosing of cyclophosphamide (CPA) in mice bearing E0771 mouse breast tumors induced an immunostimulatory response characterized by infiltration of CD8+ T-cells coupled with a rapid decrease in tumor volume. The treatment response was shown to result from both an immune response and the cytotoxic effects of CPA. This was shown by inhibiting the interferon-1 pathway by blocking interferon-α/β receptor (IFNAR-1) with an antibody during CPA treatment, which greatly inhibited immune cell infiltration, leading to a lack of tumor regression. Type 1 interferon activation has a direct effect on the innate and adaptive response including mediating T-Cell recruitment(Huber & David Farrar, 2011), which was shown to be required for tumor regression. This is representative of an immunosuppressive model in which CPA would normally successfully treat the tumor, however, the antibody prevents the necessary immune mediated tumor cell death. This paired model of CPA vs CPA + IFNAR-1 antibody identifies immune activation as a key mechanism of response and resistance.

In this work, we used SFDI to image this paired model along with an untreated control tumor group to confirm that optical scattering can serve as a prognostic imaging biomarker to discriminate between responding and resistant tumors. We utilized Generalized Estimating Equations (GEE) to longitudinally model the SFDI data and identify differences in optical parameters between treatment-responsive, treatment-resistant, and control tumors. Additionally, through the use of linear discriminant

analysis, the classification accuracy of optical parameters at different timepoints was calculated and compared to the gold standard of tumor volume.

4.2 Methods

4.2.1 Spatial Frequency Domain Imaging

Specific details about the SFDI methodology, instrumentation and processing have been well described elsewhere(Tabassum et al., 2016, 2018, 2021). The Reflect RS system (Modulim Inc. Irvine, CA) was utilized to conduct the imaging. Briefly, SFDI was used to extract tissue optical properties: the absorption coefficient (μ_a) and reduced scattering coefficient (μ_s'), at each illumination wavelength on a pixel-by-pixel basis shown in Figure 4.1.

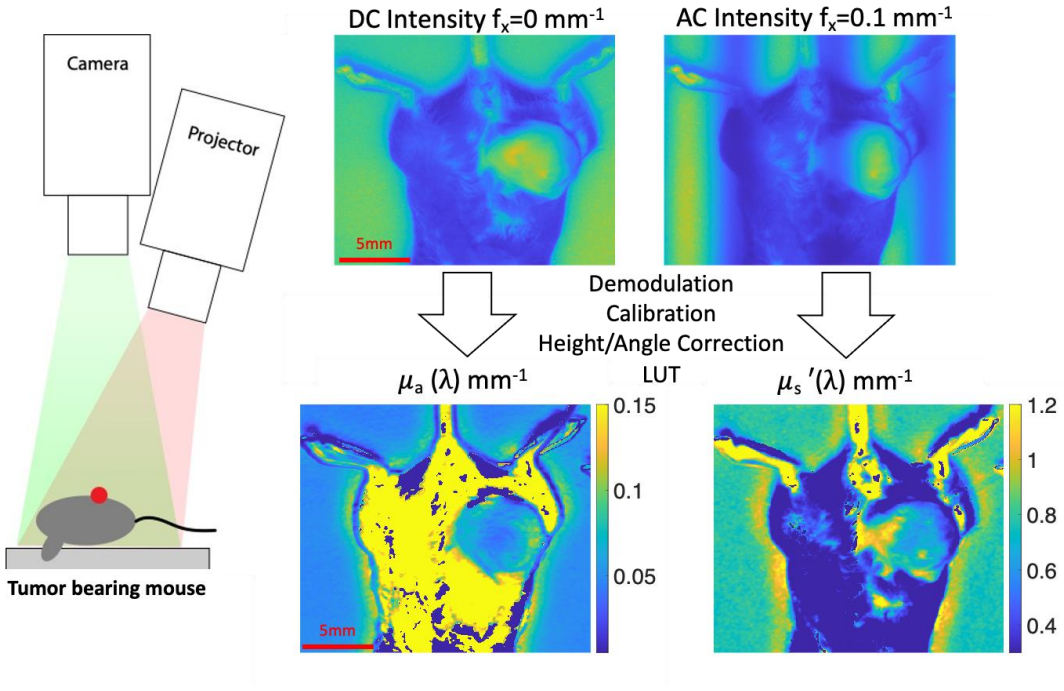

Figure 4.1. On the left, schematic of the SFDI system with the projector and camera. On the right is an example of intensity images at 731 nm for DC and AC (f_x=0.1 mm^{-1}). These are

demodulated, calibrated against a phantom, corrected for both height and angle, and then fit to a two-layer lookup table to calculate the optical properties: μ_a and μ_s'.

SFDI projects spatially modulated sinusoidal illumination patterns onto tissue over a 15x20 cm field of view. Illumination is provided with LEDs at 659, 691, 731, and 851 nm. For this study, two spatial frequencies, 0 and 0.1 mm-1, were projected at each wavelength at 3 different phase offsets (0°, 120°, and 240°) using a digital micromirror device (DMD). A CCD camera was used to collect the remitted light from tissue. Images were demodulated to extract the modulation amplitude envelope for each wavelength-frequency combination using a previously established method (Cuccia et al., 2009). Prior to tissue measurement, a calibration measurement was taken on a tissue mimicking phantom with known optical parameters: (659nm: μ_a=0.0086 $\mu_s' = 1.044$; 691nm: μ_a=0.0088 $\mu_s' = 1.014$; 731nm: μ_a=0.0087 $\mu_s' = 0.980$ 851 nm: μ_a=0.0074 $\mu_s' = 0.893$) to remove the system response and to obtain calibrated diffuse reflectance maps. These measurements are additionally calibrated with the use of an in-frame phantom to correct for any drift that occurs throughout a measurement day, which may span several hours.

The calibrated diffuse reflectance values were then corrected for the height and angle of the tumor(Zhao et al., 2016). The angle correction algorithm is able to correct for tissues surface angles up to 40-degrees and any angles greater than this threshold were not included in the analysis. The corrected diffuse reflectance values at each pixel were fit to a two-frequency, two-layer lookup table (LUT) to determine the tissue optical properties at each illumination wavelength. This two-layer LUT was developed to account for fixed

mouse skin layer optical properties in order to better estimate the underlying tumor optical parameters(Tabassum et al., 2018).

The μ_s' at each wavelength was fit to a power law of the form:

$$\mu_s'(\lambda) = a * \left(\frac{\lambda}{\lambda_{800}}\right)^{-b}$$

where a is the scattering amplitude normalized to 800 nm and b is the scattering power. The μ_a at each wavelength was fit using Beer's Law with the known extinction spectra to calculate chromophore concentrations (μM) of oxy-hemoglobin (HbO2) and deoxy-hemoglobin (HHb).

$$\mu_a(\lambda) = \varepsilon_{\mathrm{HbO_2}}(\lambda) * ct_{\mathrm{HbO_2}} + \varepsilon_{\mathrm{HHb}}(\lambda) * ct_{\mathrm{HHb}}$$

Additional composite metrics of total hemoglobin (ctTHb= ctHbO2+ctHHb) and oxygen saturation (StO2= ctHbO2/ctTHb) were also calculated.

An ROI was manually selected over the tumor region of resulting optical property and hemoglobin maps using the same procedures that have previously been described(Tabassum et al., 2021). Any remaining artifacts in the image were removed such as non-physiological data with extremely low absorption. All data analyzed and displayed represents the means over the ROI. All SFDI processing was conducted using MATLAB R2020b (MathWorks, Natick, Massachusetts).

4.2.2 Mouse model, treatment, and ex vivo analysis

Five-to six-week-old female C57BL/6 mice (B6-F, Taconic Biosciences, Rensselaer, New York) were implanted orthotopically with 2 x 105 mouse E0771 mammary carcinoma cells in the fourth mammary fat pad. Mice (n=26) were randomized to three groups: Control, PBS (vehicle) + isotype control (n=3); CPA, cyclophosphamide (CPA) (Cat # C0768, Sigma-Aldrich, St. Louis, MO) + isotype antibody control (n=9); and CPA + Ab, CPA + IFNα/β receptor-1 (IFNAR-1) antibody (clone MAR1-5A3, BioXCell, West Lebanon, NH) (n=14). Treatment was initiated on Day 0 once the tumor volumes reached 250 mm3, based on caliper measurements of tumor length (L) and tumor width (W) and the formula: V= (3.14/6) *(L*W)3/2. Vehicle control was administered as 200 μL of PBS every 6 days. Isotype control and anti-IFNAR-1 were administered as a 1 mg dose on Day -1, 0.5 mg on Day 0, and 0.25 mg every 3 days afterwards. CPA was administered on a metronomic schedule every 6 days at 110 mg/kg. Volume and SFDI imaging measurements were taken on Days 0-6 and then every 3 days from Days 9 to 30.

Approximately half of the treated mice (CPA, CPA + Ab) were euthanized on Day 12 and the remaining on Day 30 for ex vivo analysis. All the Control mice were euthanized by Day 12. Mice were additionally euthanized when deemed necessary by veterinarian for animal safety and health. Mice were euthanized through CO2 asphyxiation and confirmed through cervical dislocation. The exact number of mice in each treatment category at each time point are shown in Figure S4.1. All animal work was reviewed and approved by the Boston University Institutional Animal Care and Use Committee. All animal experiments were performed in accordance with the necessary and relevant

guidelines. This manuscript follows the reporting recommendations of the ARRIVE guidelines.

4.2.3 Statistical Analysis

Generalized estimating equations (GEE) were used to longitudinally model the SFDI optical parameters and tumor volume throughout the course of the study using SAS (SAS institute)(Littell et al., 1991). GEEs are a method to model the population averaged effects for longitudinal data with repeated measurements. All parameters were normalized to baseline values at day 0 and presented as a percent change from baseline in order to normalize inter-mouse differences. The GEE incorporates the information from repeated measurements from an individual to better model the population means. The GEE allowed for an unbalanced longitudinal dataset with subjects considered as clusters, an autoregressive correlation structure, and a normal model with identity link function. Separate models were run for the outcome variables of interest: scattering amplitude (a), deoxy-hemoglobin concentration (ctHHb), and tumor volume. Separate models were run on the short-term trends consisting of all three treatment groups until Day 12, when there are at least 3 mice per treatment category and the long-term trends, consisting of the CPA and CPA + Ab group until Day 30. Significance between the model parameters was determined at 0.050 and when adjusted for multiple comparisons at 0.017. Post-hoc contrasts for outcome variables adjusted for model covariates were compared across treatment groups at each measurement day. Significance for the post-hoc contrasts was

determined at 0.050 and when adjusted for multiple comparisons was at 0.007 for the short-term analysis and 0.003 for the long-term analysis.

Linear discriminant analysis (LDA) was performed to assess the classification accuracy of the SFDI-derived optical parameters to discriminate the different treatment groups relative to the reference of tumor volume. The LDA assumed multivariate normal distributions and equal covariances for each group. The analysis utilized leave-one-out cross validation to limit biasing the classifier. Similar to the GEE analysis, two separate analyses were conducted: (1) a short-term analysis consisting of all treatment groups up to Day 6 and (2) a long-term analysis consisting of CPA and CPA + Ab treatment groups up to Day 30. Due to the presence of three groups, the figure of merit was classification accuracy ((Correctly Classified Cases)/All Cases).

4.3 Results

4.3.1 Regimen Specific Volume Changes

Tumor volume changes are shown in Figure 4.2a with day 0 representing the first day of treatment when tumor volume reached 250mm^3, between 21-24 days after inoculation. The CPA group showed an increase in volume until day 3 when the tumor volume began to sharply decrease. The Control and CPA + IFNAR-1 Ab groups had large increases in tumor volume. Control group tumors appeared to undergo exponential growth, and all mice in this group were euthanized on Day 12. The CPA + Ab group showed a linear increase in tumor volume until approximately Day 9, followed by growth stasis.

4.3.2 Regimen Specific ex vivo Analysis

The *ex vivo* analysis is extensively described in the companion publication (Vergato et al., 2021). Briefly, using qPCR and fluorescence activated cell sorting, it was determined that there was a transient upregulation of immune stimulated genes such as MX1 and a subsequent infiltration of CD8+ T-Cells in the CPA group. This is in contrast to the CPA + Ab group, in which there was limited upregulation of immune stimulated genes and a lack of infiltrating CD8+ T-cells.

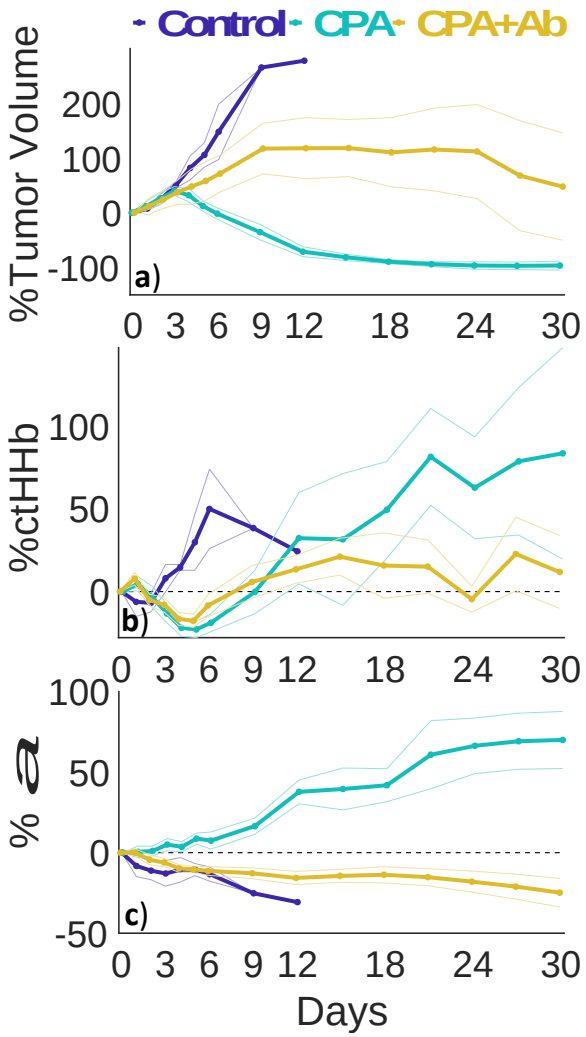

Figure 4.2. Longitudinal Day 30 Volume and Optical Changes Across Treatment Groups. Percent change in a) tumor volume, b) ctHHb, c) *a* separated by treatment: Control (purple), CPA (blue), CPA + Antibody (yellow). Lines represent means and shaded bars represent standard errors.

4.3.3 Regimen Specific Optical Changes

SFDI optical changes were differentially modified by their specific treatment. Two parameters, ctHHb and *a*, manifested markedly different patterns based on treatment, as shown in Figure 4.2b & c, respectively. ctHHb increased dramatically in the Control group over the early measurement period (Days 3-6) compared to both treated groups, which both showed a small decrease in the same time period. The scattering amplitude, *a*, increased dramatically over time in the CPA treatment group, while the Control and CPA + Ab groups both showed small decreases throughout their respective treatment course. The other longitudinal optical parameters measured by SFDI are shown in Supplemental Figures 4.2-5. Representative widefield *a* maps for each treatment group are shown in Figure 4.3. The differences between the CPA and other treatment groups increased over time for both ctHHb and *a*.

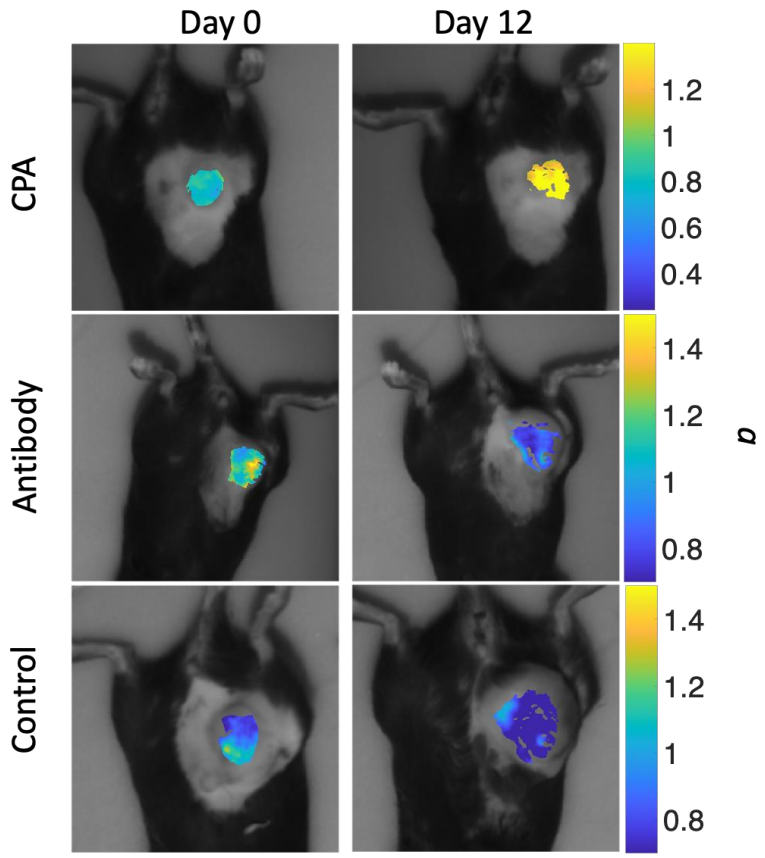

Figure 4.3. SFDI maps across treatment groups. Representative wide-field SFDI maps of the changes in *a* parameter (mm^{-1}) at Day 0 and 12 across the each of the three treatment groups.

4.3.4 Longitudinal Analysis

GEE Analysis demonstrated that Tumor Volume, ctHHb and *a* all had significant covariates of time * treatment group. Post hoc Analysis of the comparisons between the different treatment groups at different time points can be visualized in Supplementary Tables 1-3. Volume was significantly different between the CPA and Control group starting on Day 3 and the magnitude of the change increased each subsequent day. The CPA + Ab group was significantly different from the CPA and Control group starting on Day 5 and the difference between the groups continued to increase each subsequent day.

ctHHb was not significantly different between the CPA + Ab and CPA group at any time point. ctHHb was significantly different between the Control and both treatment groups during Days 4-6. After Day 6, the changes between the groups started to decrease. *a* was significantly different from the CPA group relative to the other groups starting on Day 5, and the differences tended to increase at subsequent time points.

4.3.5 Discriminant Analysis

Linear Discriminant Analysis demonstrated that in the short-term analysis the best combination of optical features was ctHHb and *a* on Day 5 with an accuracy of 0.92 to discriminate between the three treatment groups, as shown in Figure 4.4. This was only matched by the tumor volume metric on Day 6 with an accuracy of 0.92. Additionally, on Days 3, 4, and 5 the ctHHb and *a* metric had a substantially larger accuracy compared to the single feature of volume. The best single optical feature was *a*, which was equivalent to or outperformed volume on Days 3, 4, and 5.

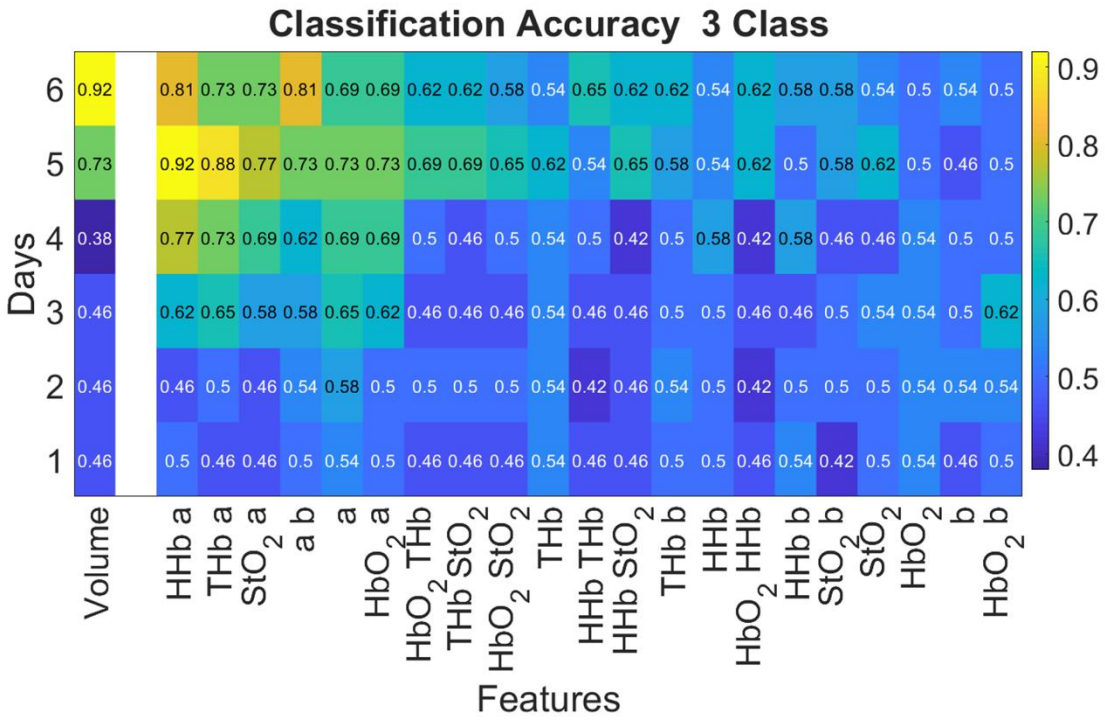

Figure 4.4. Short term classification accuracy feature selection. Linear discrimination analysis was conducted on the short-term cohort (through Day 6) for all 3 treatment groups (Control, CPA, and CPA + Ab). The classification accuracy for each timepoint and feature is displayed in text and indicated by shading for each metric at each timepoint. The combination of the SFDI parameters ctHHb and *a* provided higher classification accuracy than tumor volume on days 3, 4, and 5.

For the long-term analysis shown in Figure 4.5, *a* as a single feature was the best optical discriminator between the CPA and the CPA + Ab group over the entire study. It was a superior discriminator compared to tumor volume for the first five days, after which volume either matched or exceeded classification accuracy for the duration of the study. The individual trends in ctHHb and *a* along with tumor volume on Day 5 are shown in Supplemental Figure 4.6. These data, color coded by treatment, visually demonstrate how each treatment group displays a distinct trend. Figure 4.6 presents a scatterplot of the relationship between ctHHb and *a* for individual tumors on Day 5, with dashed lines

indicating the lines of separation between each group. This figure shows that with an overall accuracy of 0.92, there were 2 misclassifications out of 24 subjects: one of each of the CPA and Control groups were mistakenly determined to be in CPA + Ab group.

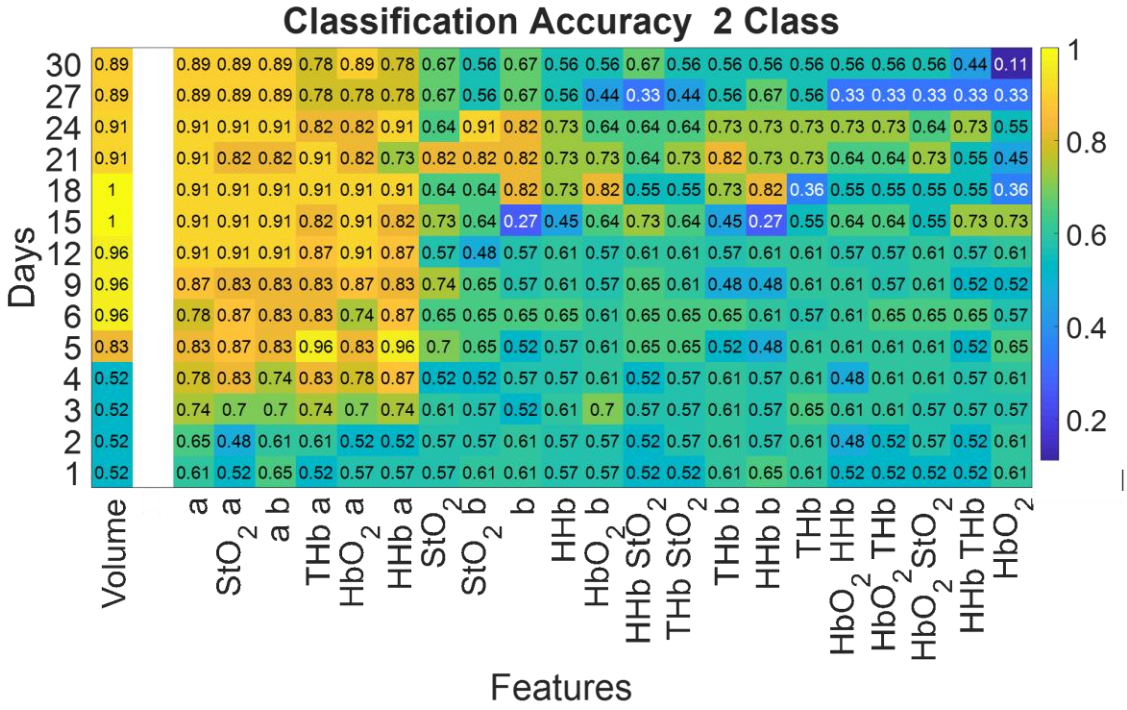

Figure 4.5. Long term classification accuracy feature selection for responders (CPA) versus resistant (CPA + Ab) cohorts. Linear discrimination analysis was conducted on the long-term cohort (through Day 30) for the treatment groups. The classification accuracy for each time point and feature is displayed in text and indicated by shading for each metric at each time point. SFDI derived parameters predicted earlier ability to discriminate responders versus resistance mice compared to tumor volume.

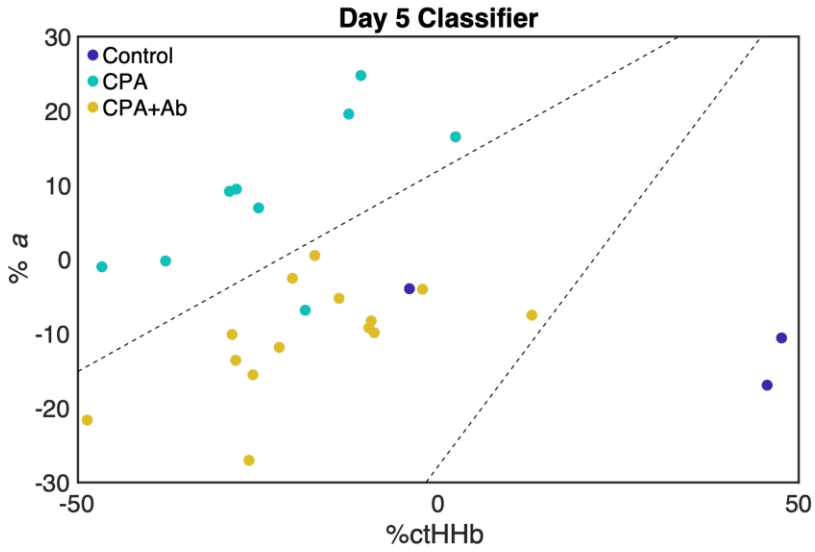

Figure 4.6 Feature Classification at Day 5. Scatterplot of the 2 best classification features: ctHHb and a for individual mice. The color of the individual points indicates its respective treatment: Control (purple), CPA (blue), CPA + Ab (yellow). The dashed lines indicate the calculated lines of separation between the different treatment groups.

4.4 Discussion and Conclusion

This works demonstrates the utility of SFDI to identify novel prognostic optical biomarkers for immune-modulated chemotherapy response and resistance. Specifically, scattering amplitude, *a*, was shown to be capable of accurately discriminating between a paired treatment-responsive and treatment-resistant murine breast cancer model at early time points. Dramatic changes in *a* occurred prior to changes in tumor volume, demonstrating its potential prognostic value as an early predictor of tumor response and resistance.

The two treatment groups and one control group exhibited dramatically different longitudinal tumor volume trends. The untreated control group showed a large,

exponential increase in tumor volume, as expected. The CPA + Ab group displayed a steady linear increase in tumor volume until Day 12, when it reached tumor stasis, likely representing an immunosuppressive phenotype. The CPA group showed a steady decrease in tumor volume after Day 3 and until Day 12, demonstrating a treatment-responsive and likely immunostimulatory phenotype. These results demonstrate a paired model of treatment response and resistance directly linked to immune stimulation or inhibition, respectively.

Starting on Day 5, the *a* parameter showed significant differences through GEE analysis ($p<0.005$) when comparing the CPA group (9% increase) to both the CPA + Ab (10% decrease) and Control (10% decrease) groups. This difference continued to grow throughout the study. This finding builds upon the previous findings by our lab that *a* can serve as a prognostic biomarker of treatment response in both prostate and breast cancer models (Tabassum et al., 2021).

The *a* parameter also showed predictive ability to discriminate between responsive, resistant, and untreated control tumors using linear discriminant analysis. The combination of ctHHb and *a* had high predictive ability to separate the three groups and outperformed tumor volume on Days 3, 4, and 5. When comparing the responsive CPA and resistant CPA + Ab, only one CPA mouse was misclassified. This means that all of the resistant tumors were accurately identified, which may represent the most important use of this imaging biomarker. The *a* parameter was equal to or outperformed tumor

volume as a classification feature on the first 5 days of study when discriminating between the CPA and the CPA + Ab group, and demonstrated excellent classification accuracy (~0.9) throughout the rest of the study. We note that the optical parameters used in the analysis were normalized to their pretreatment values and were represented as percent changes from baseline. This may help to improve the translatability of these findings as the classification accuracy relied only on relative changes rather than absolute tumor optical properties, which are likely to be highly variable in a diverse clinical population.

The changes observed in the *a* parameter are consistent with our prior work, which demonstrated that increases in the *a* parameter were associated with increased apoptosis as determined by ex-vivo immunostaining (Tabassum et al., 2021). Apoptosis induces a dramatic shift in the microarchitecture of a cell(Pucci et al., 2000). The chromatin in the nucleus deforms into aggregates before the cell nucleus breaks apart into smaller pieces. This in turn increases the local density of scattering centers which has been shown to increase the *a* parameter(Mulvey, Lie, et al., 2011; Mulvey, Zhang, et al., 2011).

We also note that in the companion paper describing the model used here, the CPA treated groups tended to show cytotoxic CD8+ T-Cell infiltration by Day 6, (see Figure 5 of ref (Vergato et al., 2021)), which is approximately when the scattering changes between the groups began to differentiate. This suggests that T-Cells contribute to treatment response as cytotoxic CD8+ T-cells most commonly kill cancer cells through

apoptotic pathways(Martínez-Lostao et al., 2015). Clinically, the presence of tumor infiltrating lymphocytes and specifically CD8+ T-cells has been associated with improved outcomes (Dieci et al., 2021; Oshi et al., 2020). It has previously been shown that the infiltration of CD8+ T-cells in EO771 tumors receiving immune checkpoint blockade therapy was necessary for tumor response and was associated with improved vessel perfusion (Zheng et al., 2018). Interestingly, in this work, CPA treatment was associated with an increase in ctHHb, ctTHb and a drop in StO_2 after day 6 (Figures 4.2b and Supplementary Figures S4.3-4), suggesting a higher tumor blood volume and a more hypoxic phenotype.

While the study focused on optical scattering changes, it is of note that the changes in ctHHb in the control group were significantly different from the treatment groups between Days 3 and 6. The large early spike in ctHHb in the control group may be correlated to the rapid tumor growth during this time period, potentially indicating high metabolic activity, and the tumor outgrowing its vascular supply(Martin et al., 2019). Interestingly, after Day 9, ctHHb of the CPA group continued to increase through the end of the study, despite the fact that the tumor volume decreased or reached stasis. This is in contrast to the CPA + Ab group that approximately followed the same trends as the CPA group until Day 15, after which ctHHb started to decrease and then stabilized around a smaller value (25% vs 50%). This could potentially be due to the fact that the tumor volume of the CPA + Ab group stabilized at this point and was no longer rapidly growing.

There are several limitations to this study. First, this study did not assess the optical properties in healthy tissue such as the contralateral fat pad, which may have changed with treatment. Second, this study did not compare the tumoral effect of administering the IFNAR-1 antibody in the absence of CPA. The IFNAR-1 antibody blocks a major immune pathway, which could have downstream effects on tumor growth and other functional changes. We note however that in a prior study in a mouse glioma model that IFNAR-1 antibody had no effect on tumor growth in the absence of CPA treatment(Du & Waxman, 2020). Here its use was solely to block the immune stimulation caused by metronomic CPA (Vergato et al., 2021). Third, a limited number of untreated control mice (n=3) were utilized. This was because the primary aim was to compare the changes between groups receiving treatment. Fourth, SFDI has a relatively shallow penetration depth (~ 5 mm) and may not be sensitive to changes in deeper tissue. Finally, depth sectioning was not explored with SFDI here, potentially obfuscating spatial heterogeneity such as differences in the core compared to the periphery of the tumor. Finally, while SFDI has been extensively used in various clinical applications including breast cancer treatment monitoring, its limited depth sensitivity could be a significant challenge in clinical setting with deeper tumors (Gioux et al., 2019; Robbins et al., 2017). Instead, other diffuse optical imaging technologies such as frequency domain- or time domain-diffuse optical spectroscopy may be better suited for tracking the scattering changes in tumors (Applegate et al., 2020). These clinical technologies allow for the potential for translation and validation of biomarkers found in the preclinical setting with SFDI. There

has been limited clinical work in examining scattering as a prognostic biomarker with diffuse optics, representing a potential avenue for future study.

Identification of prognostic biomarkers for treatment response remains a critical factor for improving treatment response. We have demonstrated SFDI derived optical scattering can serve as a promising prognostic marker to differentiate immune response and ultimately tumor response. This validates SFDI as a tool to investigate tumoral functional and metabolic changes when exposed to agents with varying mechanisms of actions such as immunotherapies. Importantly, this also raises the potential of using SFDI to discover predictive markers of resistance to treatment.

4.5 Supplementary Information

ctHHb						
	Antibody-CPA		Antibody-Control		CPA-Control	
Days	Mean ± SE	p-value	Mean ± SE	p-value	Mean ± SE	p-value
1	3 ± 5.5	0.59	14.01 ± 8	0.08	11.01 ± 8.25	0.18
2	-1.79 ± 6.91	0.80	1.72 ± 5.61	0.76	3.51 ± 7.5	0.64
3	5.33 ± 6.76	0.43	-15.97 ± 7.98	0.05	-21.3 ± 8.56	0.01
4	5.43 ± 6.1	0.37	**-31.09 ± 4.03**	**<.0001**	**-36.51 ± 4.99**	**<.0001**
5	5.16 ± 6	0.39	**-47.44 ± 14.29**	**0.0009**	**-52.6 ± 14.56**	**0.0003**
6	10.4 ± 8.14	0.20	**-58.39 ± 20.59**	**0.0046**	**-68.79 ± 20.19**	**0.0007**
9	6.03 ± 15.59	0.70	-41.4 ± 37.07	0.26	-47.43 ± 37.89	0.21
12	-18.83 ± 27.22	0.49	-16.06 ± 28.93	0.58	2.76 ± 38.06	0.94
15	-18.14 ± 27.75	0.51				
18	-39.51 ± 27.89	0.16				
21	-70.76 ± 28.36	0.013				
24	-70.66 ± 25.53	0.01				
27	-60.16 ± 39.94	0.13				
30	-74.81 ± 56.92	0.19				

Supplementary Table S4.1 Post hoc GEE contrast for ctHHb treatment comparisons. Post hoc GEE contrasts for ctHHb adjusted for model covariates comparing each pair of

treatment groups at each treatment day with the mean and standard error along with the p-value. Significance for the short term analysis was determined at 0.007 and long term analysis at 0.003 and is indicated by bolding.

a						
	Antibody-CPA		**Antibody-Control**		**CPA-Control**	
Days	Mean ± SE	p-value	Mean ± SE	p-value	Mean ± SE	p-value
1	-0.4 ± 4.06	0.92	8.35 ± 5.8	0.15	8.75 ± 6.37	0.17
2	-5.44 ± 4.09	0.18	6.73 ± 5.5	0.22	12.17 ± 5.42	0.02
3	-11.11 ± 4.32	0.01	6.82 ± 6.93	0.33	17.93 ± 7.38	0.02
4	**-13.34 ± 3.77**	**0.0004**	0.85 ± 6.61	0.90	14.19 ± 6.9	0.04
5	**-19.12 ± 3.76**	**<.0001**	0.07 ± 3.6	0.99	**19.18 ± 4.46**	**<.0001**
6	**-18.84 ± 5.64**	**0.0008**	1.95 ± 4.47	0.66	**20.79 ± 6.17**	**0.0008**
9	**-29.24 ± 5.72**	**<.0001**	13.12 ± 8.08	0.10	**42.36 ± 8.79**	**<.0001**
12	**-53.41 ± 7.97**	**<.0001**	**15.48 ± 4.9**	**0.0016**	**68.89 ± 7.54**	**<.0001**
15	**-47.42 ± 10.60**	**<.0001**				
18	**-50.75 ± 8.88**	**<.0001**				
21	**-72.39 ± 18.12**	**<.0001**				
24	**-81.65 ± 15.47**	**<.0001**				
27	**-87.58 ± 15.77**	**<.0001**				
30	**-92.78 ± 16.63**	**<.0001**				

Supplementary Table S4.2 Post hoc GEE contrast for a treatment comparisons. Post hoc GEE contrasts for a adjusted for model covariates comparing each pair of treatment groups at each treatment day with the mean and standard error along with the p-value. Significance for the short term analysis was determined at 0.007 and long term analysis at 0.003 and is indicated by bolding.

Volume						
	Antibody-CPA		Antibody-Control		CPA-Control	
Days	Mean ± SE	p-value	Mean ± SE	p-value	Mean ± SE	p-value
1	-0.31 ± 4.59	0.95	4.31 ± 4.12	0.30	4.62 ± 2.85	0.10
2	-1.85 ± 5.35	0.73	-1.96 ± 6.12	0.75	0.11 ± 5.54	0.98
3	-2.51 ± 6.17	0.68	-13.18 ± 6.25	0.03	**-10.67 ± 3.64**	**0.0034**
4	15.98 ± 9.14	0.08	-33.84 ± 13.17	0.01	**-49.82 ± 10.96**	**<.0001**
5	**45.95 ± 9.58**	**<.0001**	**-47.55 ± 13.92**	**0.0006**	**-93.5 ± 10.98**	**<.0001**
6	**73.13 ± 9.23**	**<.0001**	**-76.2 ± 25.35**	**0.0026**	**-149.33 ± 24.04**	**<.0001**
9	**152.64 ± 12.7**	**<.0001**	**-145.75 ± 17.05**	**<.0001**	**-298.39 ± 12.98**	**<.0001**
12	**189.02 ± 14.62**	**<.0001**	**-157.82 ± 20.36**	**<.0001**	**-346.84 ± 14.74**	**<.0001**
15	**-186.88 ± 16.61**	**<.0001**				
18	**-188.42 ± 19.47**	**<.0001**				
21	**-199.3 ± 24.04**	**<.0001**				
24	**-199.16 ± 28.60**	**<.0001**				
27	**-184.14 ± 32.26**	**<.0001**				
30	**-161.29 ± 32.28**	**<.0001**				

Supplementary Table S4.3 Post hoc GEE contrast for volume treatment comparisons. Post hoc GEE contrasts for volume adjusted for model covariates comparing each pair of treatment groups at each treatment day with the mean and standard error along with the p-value. Significance for the short term analysis was determined at 0.007 and long term analysis at 0.003 and is indicated by bolding.

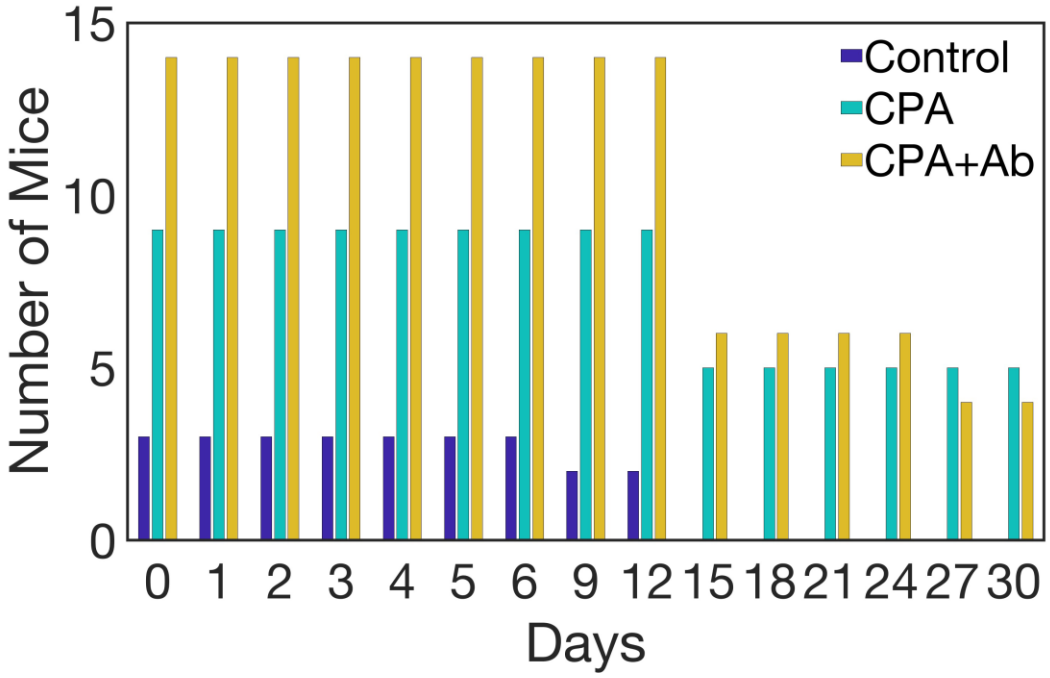

Supplementary Figure S4.1 Bar graph displaying the number of mice measured with each SFDI at each timepoint separated by each treatment group: Control (purple), CPA (blue), CPA + Antibody (yellow).

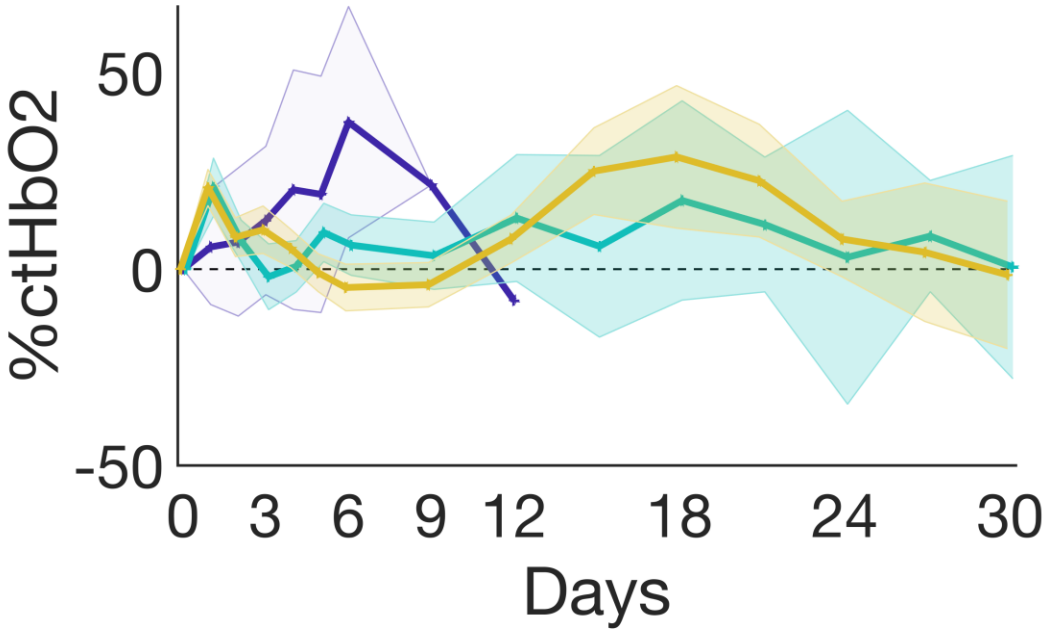

Supplementary Figure S4.2 Longitudinal Day 30 percent change in ctHbO2 Across Treatment Groups. Percent change in ctHbO2 separated by treatment: Control (purple), CPA (blue), CPA + Antibody (yellow). Lines represent means and shaded bars represent standard errors.

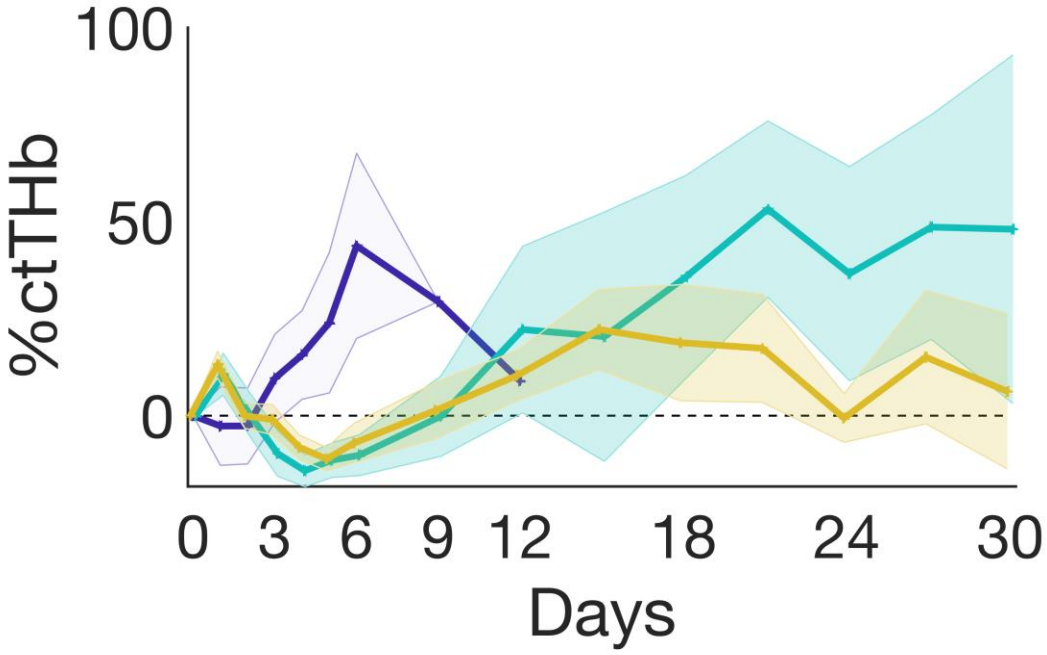

Supplementary Figure S4.3 Longitudinal Day 30 percent change in ctTHb Across Treatment Groups. Percent change in ctHbO2 separated by treatment: Control (purple), CPA (blue), CPA + Antibody (yellow). Lines represent means and shaded bars represent standard errors.

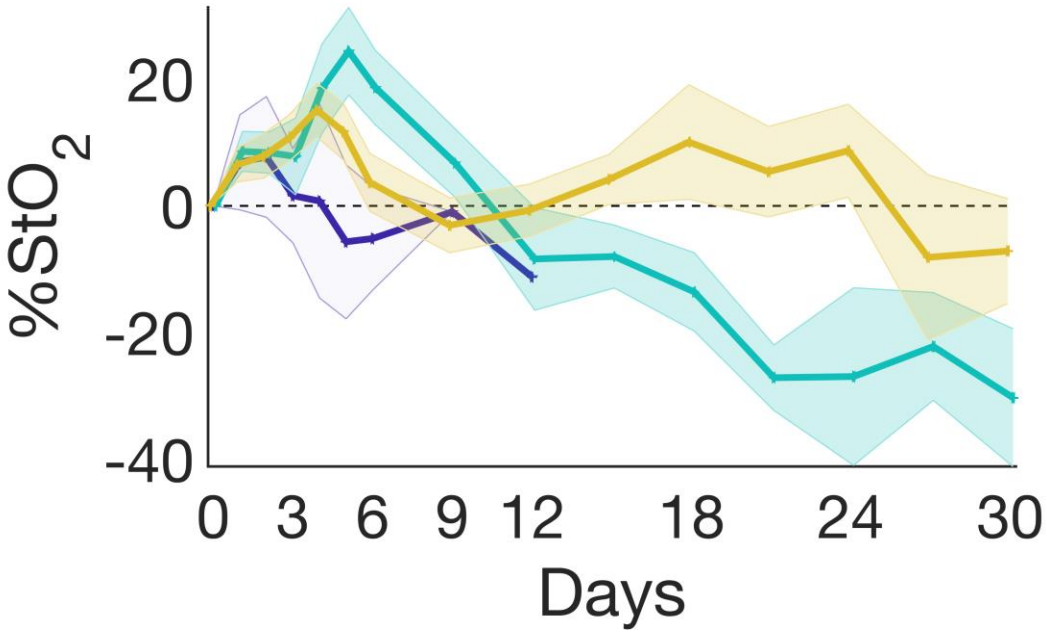

Supplementary Figure S4.4 Longitudinal Day 30 percent change in stO_2 Across Treatment Groups. Percent change in ctHbO2 separated by treatment: Control (purple), CPA (blue), CPA + Antibody (yellow). Lines represent means and shaded bars represent standard errors.

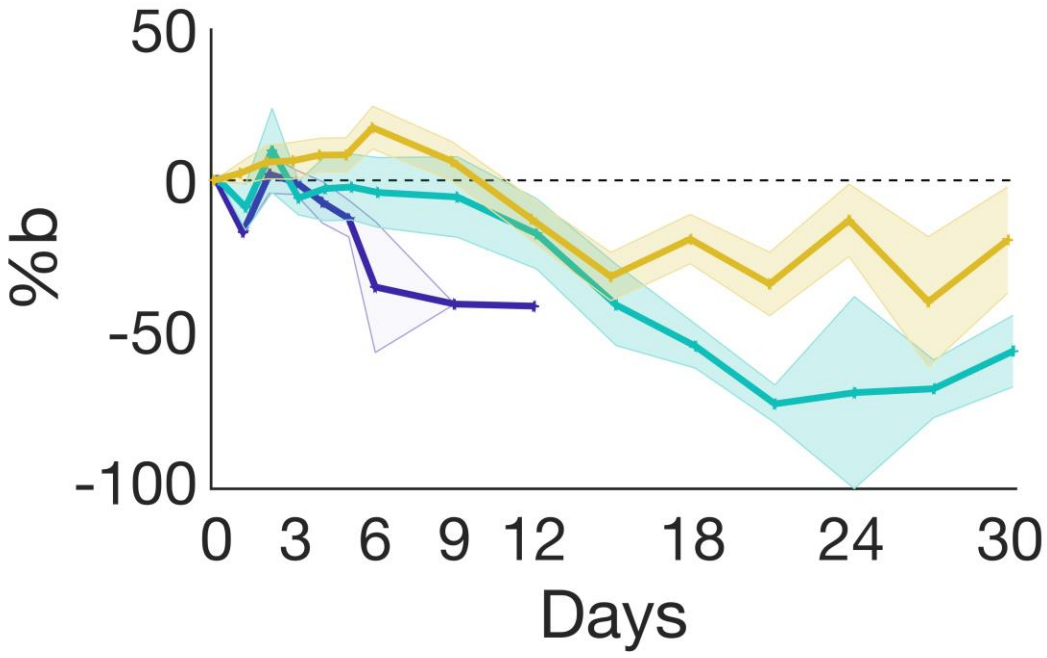

Supplementary Figure S4.5 Longitudinal Day 30 percent change in b Across Treatment Groups. Percent change in ctHbO2 separated by treatment: Control (purple), CPA (blue), CPA + Antibody (yellow). Lines represent means and shaded bars represent standard errors.

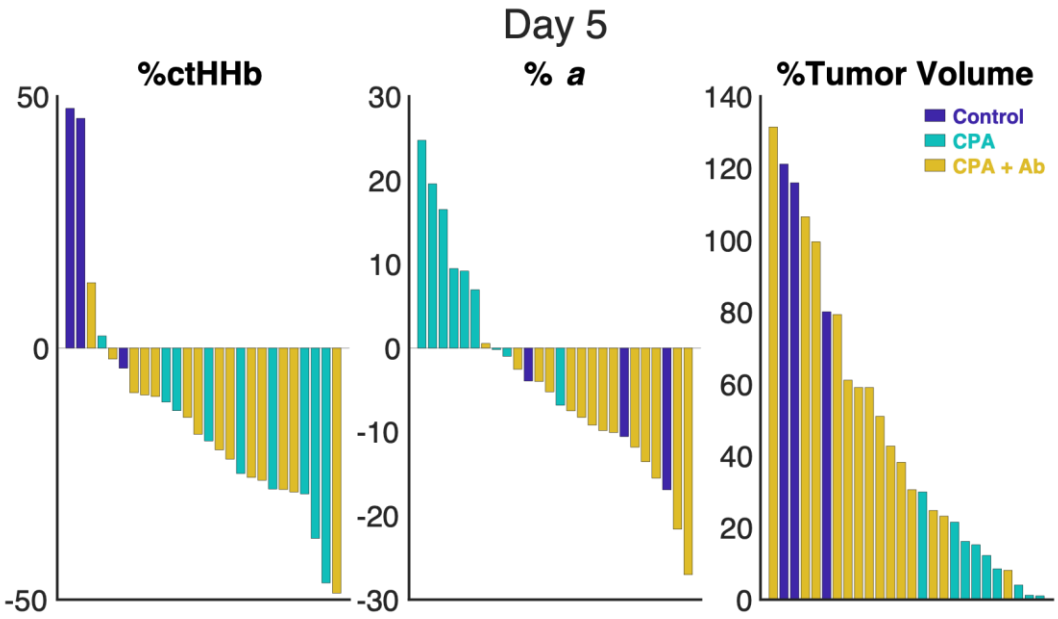

Supplemental Figure S4.6 Waterfall Plot of Individual mice optical and volume changes on Day 5. Plots of individual mice changes in ctHHb, *a*, and tumor volume on Day 5. The color of the bar plot indicates its respective treatment: Control (purple), CPA (blue), CPA + Antibody (yellow)

.

Chapter 5: Fluorescence Lifetime Imaging (FLIM) reveals that collagen density differentially induces metabolic shifts and spatial gradients in 3D breast cancer spheroids

Kavon Karrobi[a*], Anup Tank[a*], Ahsan Fuzail[a], Madhumathi Kalidoss[a], Karissa Tilbury[b], Muhammad Zaman[a], Jacopo Ferruzzi[a, c], Darren Roblyer[a]

[a]Department of Biomedical Engineering, Boston University, Boston, MA, 02215

[b]Department of Chemical and Biomedical Engineering, University of Maine, Orono, ME, 04469

[c]Department of Biomedical Engineering, The University of Texas at Dallas, Richardson, TX, 75080

Abstract

Cancer cells are mechanically sensitive to physical properties of the microenvironment, which can affect downstream signaling to promote malignancy through the modulation of metabolic pathways. Fluorescence Lifetime Imaging Microscopy (FLIM) can be used to measure the fluorescence lifetime of endogenous fluorophores, such as NAD(P)H and FAD, in live samples with subcellular spatial resolution. We used multiphoton FLIM to investigate the changes in cellular metabolism of 3D breast spheroids derived from MCF-10A and MD-MB-231 cell lines embedded in collagen with varying densities (1 vs. 4 mg/ml) over time (Day 0 vs. Day 3). FLIM data was collected over large areas (~ 700 μm^2) at imaging depths of 1-2 mm. MCF-10A spheroids demonstrated spatial gradients, with the cells closest to the spheroid edge exhibiting FLIM changes consistent with a shift towards oxidative phosphorylation (OXPHOS) while the spheroid core had changes consistent with a shift towards glycolysis. The MDA-MB-231 spheroids had a large change in FLIM measurements consistent with a shift towards OXPHOS with a more pronounced shift at the higher collagen concentration. These cells also underwent less proliferation and greater migration compared to matched cells at the lower collagen concentration. The MDA-MB-231 spheroids invaded into the collagen gel over time and cells that traveled the farthest had the largest changes consistent with a shift towards OXPHOS. Overall, these results suggest that the cells in contact with the ECM and those that have invaded farthest into the ECM, especially when

contained in a denser microenvironment, had the largest changes in FLIM measurements consistent with a shift in metabolism towards OXPHOS. More generally, these results demonstrate the ability of multiphoton FLIM to characterize how spheroids metabolism and spatial metabolic gradients are modified by physical properties of the 3D ECM.

K.K., K.T., M.Z., J.F., and D.R. were responsible for study design. K.K., M.A.F. and M.K. were responsible for developing and culturing the spheroids. K.K. was responsible for the imaging. K.K. and A.T were responsible for the data processing, image processing, and statistical analysis. K.K., A.T., and D.R. were responsible for the interpretation of data and analysis. K.K., A.T., and D.R were responsible for writing the manuscript with assistance from the other authors.

5.1 Introduction

An abnormal extracellular matrix (ECM) and its physical properties plays a critical role in the breast tumor microenvironment and has been associated with cancer development, progression, and metastasis (Insua-Rodríguez & Oskarsson, 2016). The ECM has been noted as a strong risk factor as women with dense breasts are 4-6x more likely to develop breast cancer than women with low density breasts (Boyd et al., 1995). Tumor cells can mechanically sense the physical properties of its environment and engage with the ECM through integrins and affect downstream signaling to promote a more invasive phenotype (Winkler et al., 2020). For example, the mechanosensing YAP/TAZ pathway modulates several downstream signaling cascades in stiff tumor microenvironments to increase cellular invasion and migration in addition to modulating metabolic pathways (Koo & Guan, 2018; Zanconato et al., 2016).

Cancer cells reprogram their energy metabolism to support their uncontrolled growth and proliferation (Hanahan & Weinberg, 2011). An extremely conserved modification across

many cancer types is the Warburg effect, also called aerobic glycolysis (Liberti & Locasale, 2016; Warburg et al., 1927), which is the tendency for cancer cells to shift towards glycolysis and fermentation over oxidative phosphorylation and respiration even in the presence of oxygen. The shift serves to sustain extensive cell growth and replication. While the Warburg effect has been extensively characterized, it is only one of the many metabolic perturbations observed in tumors.

Recent evidence suggests that proliferating cancer cells have a different metabolic profile than migrating cancer cells (Zanotelli et al., 2021). Cancer cell migration is a pivotal step of the metastatic cascade. Understanding the phenotypic mechanisms that drive tumor cells to migrate and eventually metastasize is critical for improving patient outcomes (Hanahan & Weinberg, 2011). The metabolic plasticity of cancer cells sustains their ability to dynamically adjust from a proliferative to migratory phenotype (Zanotelli et al., 2021). Migratory cells require a significant amount of energy to support cytoskeletal modifications and remodel the ECM (Zanotelli et al., 2021). Importantly, the metabolic demand for remodeling the ECM can depend on the physical properties of the ECM (Zanotelli et al., 2018). Migratory cancer cells support these physical modifications by following leader-follower invasion dynamics where leading migratory cells utilize more ATP as they engage and modify the ECM than the follower migratory cells (Zhang et al., 2019). The metabolic differences in leader versus follower cells and their importance in invasion highlights the need for spatially resolved methods to measure metabolic profiles to develop effective therapies targeting migrating cancer cells. (Ashton et al., 2018).

Fluorescence lifetime imaging microscopy (FLIM) is a non-invasive, spatially resolved label-free imaging modality that measures the fluorescence decay of fluorophores and can be used to measure the metabolic profile of live cancer cells (Datta et al., 2020; Georgakoudi & Quinn, 2012; Z. Liu et al., 2018). Multiphoton FLIM enhances both axial resolution and depth penetration, enabling sub-micron sensitivity throughout 3D tumor spheroid models that are hundreds of microns in diameter (Helmchen & Denk, 2005). The metabolic coenzymes nicotinamide adenine dinucleotide (NAD(P)H) and flavin adenine dinucleotide (FAD) are autofluorescent and their fluorescence decay rate dependent on if the coenzymes are free or bound. The relative proportions of free and bound NAD(P)H or FAD can infer the metabolic phenotype and been shown to correlate with conventional assays and mass spectrometry used to classify various metabolic pathways including oxidative phosphorylation, glycolysis, and fatty acid synthesis (Bird et al., 2005; Hou et al., 2016; Z. Liu et al., 2018; Mah et al., 2018; Quinn et al., 2013; Varone et al., 2014; Walsh et al., 2014). Similarly, the ratio of the bound NAD(P)H to bound FAD, the Fluorescence Lifetime Imaging Redox Ratio (FLIRR), is a promising optical biomarker to determine if a cell's primary metabolic pathway is oxidative phosphorylation or glycolysis (Wallrabe et al., 2018). A cancer cell's metabolic profile can provide critical information about its phenotype such as the differences in leader or follower characteristics (Zhang et al., 2019), or how the cancer cell is engaging with and potentially modifying the ECM (Mah et al., 2018). Other fluorescence intensity-based methods have been developed that are sensitive to other metabolic parameters such as

ATP/ADP ratio but require genetically encoded receptors (Zhang et al., 2019). FLIM can provide a label-free method to image and quantify a cells' metabolic profile to investigate the spatial relationship of cells with different metabolic demands.

Prior studies studying the effect of the ECM on cancer cells metabolism have had two main limitations. First, many prior FLIM studies have examined cancer cell metabolism in 2D cultures (Mah et al., 2018) which are unable to accurately recapitulate the 3D mechanical cell-ECM interactions (Baker et al., 2009). Additionally, epithelial cancer cells in 2D culture tend to be more glycolytic than in a 3D environment and display less metabolic plasticity (Al-Masri et al., 2021). Secondly, other studies used metabolic assays that provide molecular specificity but require bulk samples preventing the examination of the spatial metabolic trends particularly important in the case of cancer cell migration (C. Liu et al., 2021). The work conducted by Liu et al, for example, determined that stiffness of the ECM modulated the migratory and proliferative properties of 3D breast cancer cultures. They performed RNA-seq which resulted in bulk spheroid genetic enrichment scores for metabolic pathways. They demonstrated that stiffer environments induced a migratory phenotype that correlated with an overall enrichment in oxidative phosphorylation. However, RNA-seq is a bulk molecular tool and lacks sensitivity needed to characterize the spatial metabolic profiles associated with the complex metabolic phenotypes within the 3D spheroid. The characterization of single-cell level metabolic phenotypes is needed to further explore the hypothesis that leader/follower cells have stratified cellular metabolic phenotypes.

Here we present a study in which we used FLIM to image the spatial metabolic profile during migration of breast cancer spheroids embedded in 3D collagen gels at two different collagen concentrations (1mg/mL and 4 mg/mL) across two different time points (Day 0 and Day 3). We imaged two different human-derived breast cancer cell lines: MCF-10A, a non-invasive mammary epithelial cell line, and MDA-MD-231, a highly invasive breast cancer cell line. One and 4 mg/mL collagen concentrations were used to mimic a softer, low-density ECM compared to a stiffer, high-density ECM (Kang et al., 2021), respectively. We investigated the differences in migration and proliferation for each cell line from Day 0 to Day 3, and how migration and proliferation track with changes in the overall metabolic profile of the two breast cancer cell lines. Finally, the metabolic spatial maps of each spheroid were analyzed to probe any spatial metabolic relationships as a function of distance from the ECM or migration distance.

5.2 Methods

5.2.1 Cell lines and culture media

Metastatic MDA-MB-231 and non-tumorigenic MCF-10A human breast cancer cell lines were purchased from American Type Cell Culture Collection (ATCC) and cultured using standardized media and conditions as previously described (Kang et al., 2021). Briefly, MDA-MB-231 cells were cultured in DMEM (Corning, No. 10013CV), supplemented with 10% fetal bovine serum (ATCC, No. 302020). MCF-10A cells were cultured in DMEM/F-12 (ThermoFisher, No. 11330032) supplemented with 5% horse serum (Invitrogen, No. 16050122), 20 ng/ml EGF (Peprotech, AF10015; ThermoFisher, No.

10605HNAE), 0.5 mg/ml hydrocortisone (Sigma-Aldrich, No. H0888), 100 ng/ml choleratoxin (Sigma-Aldrich, C8052), 10mg/ml insulin (Sigma-Aldrich, No. I1882). Both media recipes contained 1% penicillin/streptomycin (ATCC, No. 302300; ThermoFisher, No. 15140122). Cells were maintained at 37°C and 5% CO_2 in a cell culture incubator.

5.2.2 Preparation of polydimethylsiloxane (PDMS) wells

Cylindrical PDMS wells (9 mm in diameter) were created inside 35 mm glass-bottom petri dishes (MatTek, No. P35G-0-10-C) using 3D printed self-centering cylinders as previously described (DeCamp et al., 2020). Briefly, 1 mL of a liquid PDMS mixture (Dow Corning, Midland, MI) with a 10:1 weight ratio of silicon elastomer to curing agent was deposited inside the dishes and around the cylinders and cured at 50°C for 2 hours. After removal of the cylinder, the resulting cylindrical well was cleaned from PDMS residues and coated using poly-D-lysine (Sigma-Aldrich, St. Louis, MO) and glutaraldehyde, which provided an anchoring layer for collagen to avoid gel floating. After rinsing with 1x PBS, the PDMS wells were sterilized under ultraviolet (UV) light for 30 mins.

5.2.3 Spheroid formation

MDA-MB-231 and MCF-10A spheroids were generated as previously described (Kang et al., 2021). Briefly, spheroids were generated by seeding approximately $1x10^3$ cells in each of the 96 wells of an ultra-low attachment plate (Corning, No. 7007) and allowed to form for 48 hours in the presence of 2.5% v/v Matrigel. Once formed, individual

spheroids surrounded by 5 µL of media were transferred onto coverslips inside PDMS wells (9 mm in diameter) created in 35 mm glass-bottom petri dishes (one spheroid per dish). Each spheroid was covered by 195 µL of ice-cold, rat-tail collagen I solution to achieve a total volume of 200 µL and a specific collagen concentration in each well. Collagen solutions were prepared by mixing acid-solubilized collagen I (Corning, No. 354249) with equal volumes of a neutralizing solution (100 mM HEPES buffer in 2x PBS). The desired collagen concentration was reached by adding adequate volumes of 1x PBS. Collagen solutions at different concentrations (1 and 4 mg/ml) polymerized for 1 hour at 37°C. The cell culture plates were rotated every minute for the first 10 minutes of polymerization to guarantee full embedding of the spheroid within the 3D collagen matrix. Finally, 2 mL of culture media (phenol-free, 50:50 v/v of MDA-MB-231 media to MCF-10A media) was added and the 3D organotypic culture was placed inside the incubator until taken out for FLIM measurements.

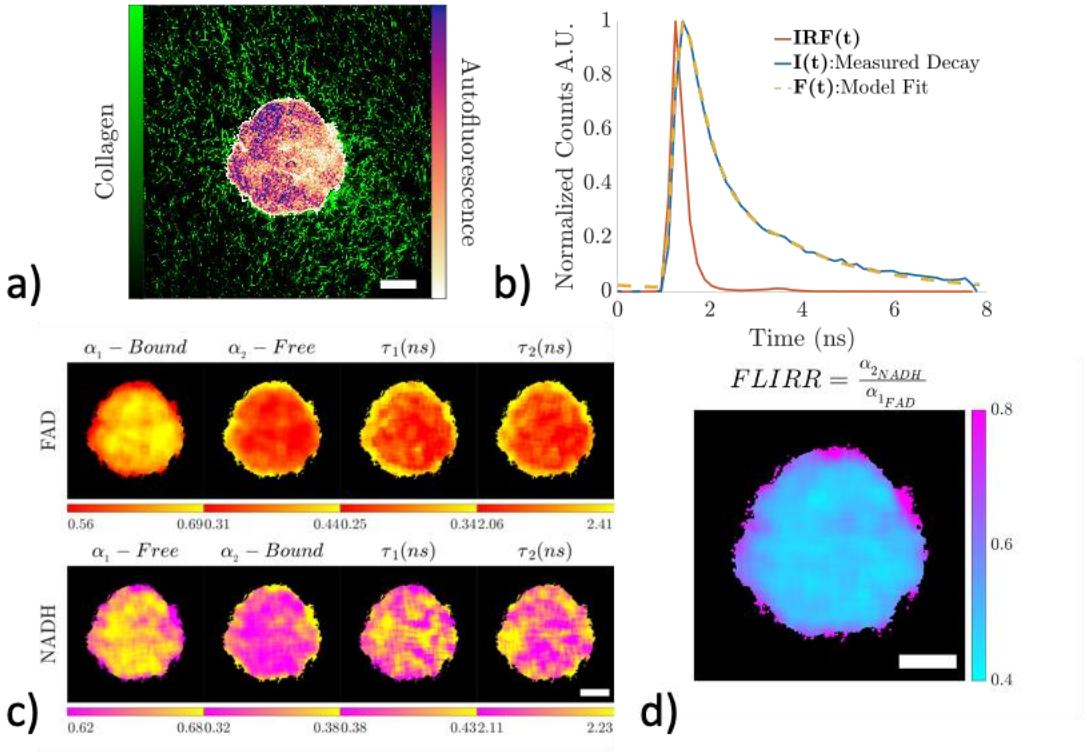

Figure 5.1. FLIM Methodology and Processing. a) An overlay of time-integrated NAD(P)H autofluorescence intensity from a MCF-10A breast cancer spheroid and second harmonic generated collagen signal from a 4 mg/mL collagen gel imaged at Day 3. B) Representative example of the measured decay signal I(t), which is a convolution of the measured impulse response function IRF(t) and the autofluorescence decay. The model fit F(t) is computed by convolving IRF(t) with a bi-exponential fluorescence decay model and comparing to I(t) using a nonlinear least squares fitting routine. C) Images of the four parameters (α_1, α_2, τ_1, τ_2) extracted from the nonlinear least squares fitting procedure for both FAD and NAD(P)H. τ_1 and τ_2 values are shown in units of nanoseconds. D) A representative image of Fluorescence Lifetime Imaging Redox Ratio (FLIRR) values in a MCF-10A spheroid, which is obtained as the ratio of bound NAD(P)H to bound FAD from part c). Scale bars (white) indicate 100 µm.

5.2.4 Multiphoton Fluorescence Lifetime Imaging Microscopy (FLIM)

Label-free multiphoton FLIM was used to monitor intracellular NAD(P)H and FAD fluorescence intensity and lifetimes of MDA-MB-231 and MCF-10A spheroids completely embedded in 3D collagen gels at different densities (1 and 4 mg/mL) over

time (days 0 and 3). These spheroids were imaged at a depth of ~1-2mm from the surface of the collagen gel in a single optical section. All spheroid samples were allowed to incubate in fresh phenol-free 50:50 culture media for a minimum of 3 hours prior to imaging. FLIM was performed using an upright multiphoton microscope (Bruker, Ultima Investigator) equipped with a stage top incubator (Tokai Hit, STXF-UKX-SET) to maintain samples at 37°C and 5% CO_2 with humidity during imaging.

A femtosecond titanium:sapphire tunable laser (Spectra-Physics, InSight X3) was used as the excitation source with a quarter-waveplate in the excitation path to circularly polarize the incident beam at the sample plane. The laser was tuned to either 760 or 880 nm for two-photon imaging of NAD(P)H or FAD respectively. For collagen imaging, through second harmonic generation (SHG), the laser was tuned to 1050 nm. The emission was detected in a non-descanned geometry through a 16x long working distance (3 mm) water immersion objective (0.8 NA) (Nikon, CFl75 LWD 16X W), and separated by a dichroic mirror (Chroma, 700 nm long-pass). A 720 nm short-pass filter blocked residual excitation wavelengths in the detection path. NAD(P)H and FAD fluorescence emission was collected using a 440±40 or 550±50 nm bandpass filter (Chroma), respectively. A GaAs photon counting photomultiplier tube (Hamamatsu, H10770PB-50) with a time-correlated single photon counter (Becker & Hickl, SPC-150) was used to collect the temporal decays of NAD(P)H and FAD autofluorescence (120 s collection time per frame, 256 temporal bins per pixel). Images were collected at a scanning resolution of 0.8 µm/pixel and 10 µs pixel dwell time using 1024 x 1024 pixels (Figure 5.1a).

SHG imaging of randomly oriented collagen fibers in the spheroid-embedded collagen samples was used to estimate the instrument response function (IRF) for both NAD(P)H and FAD FLIM configurations. To collect the IRF, the laser was tuned to 760 nm with a 375±30 nm bandpass filter for NAD(P)H analysis. and tuned to 880 nm with a 440±40 nm bandpass filter for FAD analysis, which had on average full width half maximums of 339±8 ps and 396±16 ps, respectively. SHG images (Figure 5.1a) of the collagen environment surrounding the embedded spheroids were acquired with the laser tuned to 1050 nm and a 525±35 nm bandpass filter for collection. There was a total of 8 conditions (2 cell lines x 2 collagen densities x 2 days), with each condition having n = 3 samples. As such, graphical data was generated by pooling all 3 samples for each condition.

5.2.5 Image segmentation

Binary masks were generated by processing NAD(P)H intensity images (Figure 5.1a), which were derived from the NAD(P)H lifetime data for each sample by summing the NAD(P)H temporal decays in each pixel. Two different binary masks methods were developed in MATLAB (MathWorks, R2021a) to process NAD(P)H intensity images. One method was developed to process images that contained either full or partial spheroids, and another to process images that only contained migrating cells, as one image processing pipeline was not sufficient to accurately segment both image types. For samples with full or partial spheroids, the intensity images were normalized between 0

and 1 and then a two-class Otsu's method (Otsu, 1979) was used to binarize and segment spheroids and cells from the background. The binarized and segmented images were then dilated using the built-in MATLAB functions *imdilate* and *strel* with a disk-shaped kernel (3-pixel radius) to fill in the shape of the segmented spheroids and cells. The built-in MATLAB function *imfill* (Soille, 1999) was then used to fill in any remaining gaps, followed by clearing of extraneous pixels in contact with the image borders using the built-in MATLAB function *imclearborder*.

For samples with only migrating cells, binary masks were generated from intensity images using a modified procedure to segment tumor vasculature (Karrobi et al., 2019). These steps consisted of i) a white top-hat transform, with the Matlab function *imtophat* to enhance smaller elements of the image, ii) normalizing images between 0 to 1, iii) applying an anisotropic diffusion filter (Kroon & Slump, 2009; Mendrik et al., 2009; Weickert & Scharr, 2002) to reduce noise in the images while preserving cell edges, and iv) finally a multiscale Hessian filter (Jerman et al., 2015) was applied to the images along with another top-hat transform to yield an intensity image with enhanced contrast. The image was binarized using a locally adaptive threshold (Bradley & Roth, 2011) with the MATLAB function *adaptthresh*, and refined using active contour segmentation (Chan & Vese, 2001) with the MATLAB function *activecontour* by inputting the contrast enhanced intensity image from step iv) and the binarized image.

5.2.6 FLIM image analysis

Binary masks were imported in MATLAB and used to isolate and analyze NAD(P)H and FAD lifetime data from spheroids and cells based on a previously described fitting routine (DeCamp et al., 2020). Briefly, each pixel within a given image (NAD(P)H or FAD) contained a time decay of fluorescence intensity $I(t)$ (Figure 5.1b). To maximize per pixel the total photon count in the temporal decays used during the fitting routine, lifetime data in each image was summed over space (20 x 20 pixels sliding window) and binned in time (256 temporal bins to 64 temporal bins) after applying the corresponding binary mask. The resulting lifetime images were then used to extract lifetime parameters of NAD(P)H and FAD. A bi-exponential fluorescence decay model was used to describe temporal decays of fluorescence intensity:

$$m(t) = \alpha_1 e^{-\frac{t}{\tau_1}} + \alpha_2 e^{-\frac{t}{\tau_2}}$$

where τ_1 and τ_2 represent the fast and slow lifetime components (in ns), respectively, and α_1 and α_2 represent the unitless fractional contribution of each component (with $\alpha_1 + \alpha_2 = 1$) for a given metabolic coenzyme. It should be noted that τ_1 and α_1 correspond to free NAD(P)H and τ_2 and α_2 correspond to enzyme bound NAD(P)H, and that this is reversed in the case of FAD (Figure 5.1c) (Wallrabe et al., 2018). For each masked pixel within a given image (NAD(P)H or FAD), $m(t)$ was convolved with the corresponding experimentally measured IRF and compared with the temporally binned fluorescence intensity decay data (Figure 5.1b). Using the built-in MATLAB function *lsqnonlin*, nonlinear least square analysis was performed with constraints on the lifetime parameters ($0.02\ ns \leq \tau_i \leq 100\ ns$ and $0 \leq \alpha_i \leq 1$) and seeding with random initial guesses.

The fitting routine was parallelized to handle large FLIM datasets. After processing NAD(P)H and FAD lifetime data through the fitting routine for a given sample, the Fluorescence Lifetime Imaging Redox Ratio (FLIRR) was computed for each masked pixel:

$$FLIRR = \frac{\alpha_{2_{NADH}}}{\alpha_{1_{FAD}}} = \frac{fraction\ of\ enzyme\ bound\ NADH}{fraction\ of\ enzyme\ bound\ FAD} \quad (X)$$

where lower FLIRR values have previously reported to correspond with glycolytic metabolism and higher FLIRR values to correspond with more oxidative phosphorylation (OXPHOS) phenotype (Figure 5.1d) (Wallrabe et al., 2018)

5.2.7 Probability distribution functions of FLIRR populations

Kernel density estimates of the probability distribution function (PDF) for FLIRR values for each condition was generated by pooling the FLIRR values from each binarized pixel across the three samples and using the MATLAB function *ksdensity*. For each condition, the probability distribution function was evaluated from FLIRR values of 0.2 to 1.3 in increments of 0.01 to represent the measured range of FLIRR values.

5.2.8 Estimates of differences in FLIRR distributions

The overall differences between the pdfs were quantified using the overlap index (Pastore & Calcagnì, 2019). The overlap index is calculated between two different spheroid treatment conditions by calculating the minimum of each probability

density functions of FLIRR distributions at each evaluation point (0.2:0.01:1.3) and calculating the sum over that range:

$$Overlap\ Index = \int \min\{pdf_x, pdf_y\}$$

An overlap index value of 1 represents perfect similarity and a value of 0 represents no overlap between the pdfs.

Significance was assessed by computing the median of each FLIRR distribution and computing a two-tailed t-test to compare the differences from Day 0 to Day 3 for each treatment condition at a critical alpha level of 0.05.

5.2.9 Quantification of Proliferation and Migration

Changes in proliferation was estimated by quantifying the total area of each spheroid and comparing the differences from Day 0 to Day 3. The total area was calculated by summing every binarized pixel in the segmented spheroid image. The data is displayed as the mean and standard deviation in pixels over the three replicates. Differences across time were assessed for significance by a two-tailed t-test at a significance level of $p<0.05$.

Migration was estimated by calculating the distance (in μm) every binarized pixel was from the center of the spheroid. The center was adaptively calculated depending on whether the spheroid was no longer intact. In the case of intact or partially intact spheroids, the center was identified by finding the largest unconnected object in the image and computing the center of mass using the MATLAB function *regionprops*. For

samples with no intact spheroid, the centers were determined by identifying the centers of voids left behind from previously intact spheroids using overlaid images of NAD(P)H intensity and collagen from SHG imaging. After locating the centers, the distance transform was computed relative to the center pixels using the built-in MATLAB function *bwdist* to compute the 2D Euclidean distance transform (Maurer et al., 2003). The distance distributions were pooled together across all three replicates and plotted in Figure 5.2b as boxplots. The whiskers represent 5% and 95% and the box represent 25%, 50%, and 75%.

5.2.10 2D Spatial analysis of FLIRR

The 2D spatial distribution of FLIRR was adaptively analyzed with consideration of the final organizational status of the spheroids: intact or partially intact. The 2D spatial FLIRR characteristics of intact spheroids relied on FLIRR as a function of Euclidean distance from the edge of the spheroid based on the inverted version of the segmented and binarized spheroid images (Figure 5.4). Since the cells at or near the edge of intact spheroids are either in direct contact or close proximity to the collagen environment, this 2D FLIRR analysis characterized the impact of collagen proximity on cellular metabolism.

Samples with spheroids that were partially or no longer intact due to the migration of cells lacked defined edges, and thus FLIRR values were analyzed as a function of distance from the centers of what were previously completely intact spheroids. In the case

of intact or partially intact spheroids, the center was identified by finding the largest unconnected object with the MATLAB function, *regionprops* in the segmented and binarized images, which corresponded to the core, and then computing the center of mass of that object. For samples with spheroids that were no longer intact, the centers were determined by identifying the centers of voids left behind from previously intact spheroids using overlaid images of NAD(P)H intensity and collagen from SHG imaging. After locating centers within samples with partially or no longer intact spheroids, the distance transform was computed relative to the center pixels (Figure 5.5). This form of 2D FLIRR analysis enabled a spatial assessment of metabolism as a function of migration.

5.3 Results

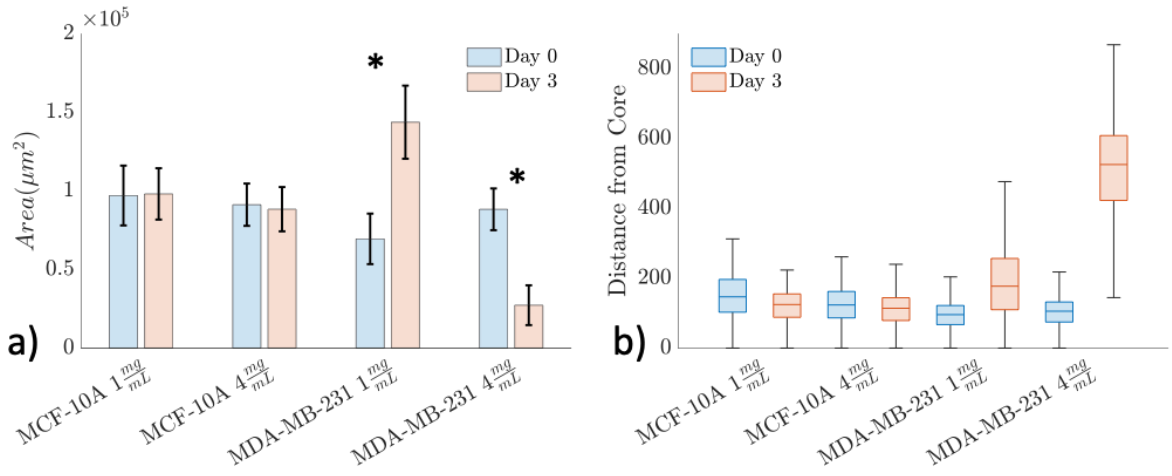

Figure 5.2. Proliferation and migration of cells across time. a) The total area occupied in each spheroid condition separated by Day 0 (blue) and Day 3 (red). Each bar represents the mean and standard deviation across the three replicates. For each condition, Day 0 (blue) was compared to Day 3 (orange) using a t-test and significance was indicated with a * ($p<0.05$). The MDA-MB-231 samples had a significant increase in proliferation at 1 mg/mL and a significant decrease at 4 mg/mL. b) The distance of every pixel from its spheroid

center for each condition separated by Day 0 (blue) and Day 3 (red). The whiskers represent 5% and 95%, the box represent 25% and 75%, and median is indicated on the boxplot. The MDA-MB-231 samples had a modest increase in migration distance at 1 mg/mL and a much larger increase at 4 mg/mL.

5.3.1 Proliferation and Migration trends across cell line, collagen concentration, and timepoint

The changes in the proliferation and migratory phenotypes were assessed from Day 0 to Day 3 across cell lines and collagen concentrations. The MCF-10A spheroids showed no significant differences in area across collagen concentrations or time as shown in Figure 5.2a. The MDA-MB-231 spheroids at 1 mg/mL had a significant increase from Day 0 to 3 in area occupied by the spheroid ($p=0.01$) demonstrating an increase in proliferation, while at 4 mg/mL there was a significant decrease in area occupied by the spheroid ($p=0.0045$) indicating a lack of proliferation.

The MCF-10A and the MDA-MB-231 spheroids at Day 0 all had intact cores and approximately the same farthest distance from the core (~300 μm), as a reference to compare against non-intact spheroids (Figure 5.2b). The MDA-MB-231 spheroids in 1 mg/mL collagen at Day 3 had a moderate increase in spheroid migration relative to Day 0 (farthest distance: ~300 μm at Day 0 vs ~500 μm at Day 3) while the MDA-MB-231 spheroids in 4 mg/mL collagen at Day 3 had a larger increase in farthest distance relative to Day 0 (~300 μm at Day 0 vs ~800μm at Day 3).

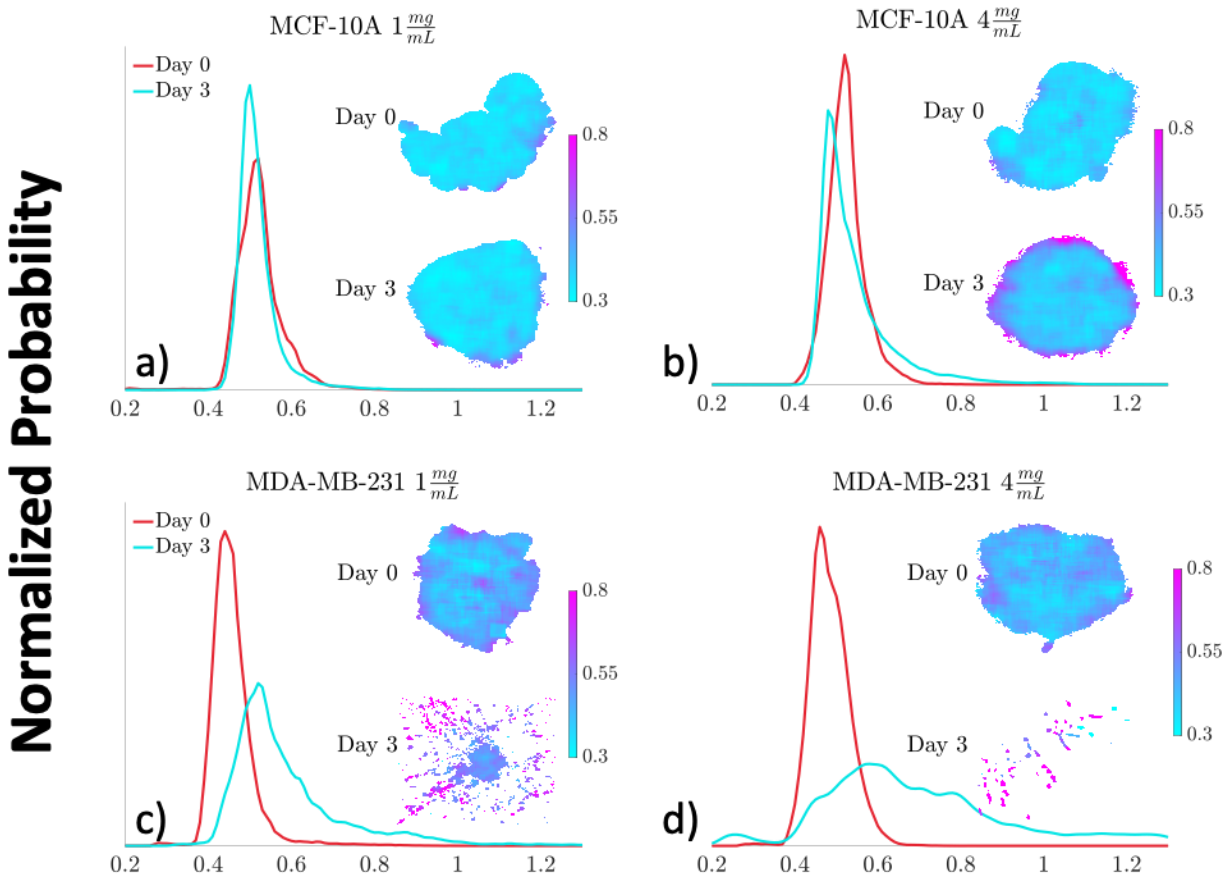

Figure 5.3. Probability Distribution Function (PDF) estimates of FLIRR values and representative FLIRR maps. Estimated PDFs of pooled FLIRR values across the three replicates are shown for MCF-10A at a) 1mg/mL and b) 4mg/mL for Day 0 (red) and Day 3 (turquoise) along with a representative example of a FLIRR map. MDA-MB-231 PDFs are shown at c) 1mg/mL and c) 4mg/mL for Day 0 (blue) and Day 3 (orange) along with representative examples of FLIRR maps. The intact spheroids (MCF-10A and the MDA-MB-231 spheroids at Day 0) are approximately 300 µm in radius, while the MDA-MB-231 spheroids at Day 3 has started to migrate and are shown over the entire 825 x 825 µm field of view. MCF-10A spheroids demonstrated a small decrease in FLIRR values towards glycolysis with a larger change at 4 mg/mL. MDA-MB-231 spheroids exhibited a large increase in FLIRR values from Day 0 to Day 3 accompanied with an increase in migration consistent with a shift towards OXPHOS.

5.3.2 Distinct FLIRR trends across cell line, collagen concentration, and timepoint

The changes in FLIRR values of the spheroids from Day 0 to Day 3, and how those changes varied across cell lines and collagen concentrations were examined using the

probability density functions of spheroid FLIRR values (Figure 5.3). The MCF-10A spheroids showed a modest shift towards lower FLIRR values from Day 0 to Day 3 in both the 1 mg/mL (overlap index: 0.85, p=0.54) and 4 mg/mL (overlap index: 0.76, p=0.85) collagen concentrations (Figure 5.3 a,b, Figure S5.1), which was more pronounced at 4 mg/mL. The MCF-10A spheroids in 4 mg/mL collagen on Day 3 had an overall shift towards lower FLIRR values although there was a subpopulation of larger FLIRR values represented by a long tail of the distribution (Figure 5.3b), suggesting that a subset of MCF-10A cells were metabolically distinct.

This contrasted with the MDA-MB-231 samples which had a much larger and statistically significant shift towards higher FLIRR values from Day 0 to Day 3. This shift was larger in the 4 mg/mL collagen concentration (overlap index: 0.32, p=0.05) compared to the 1 mg/mL (overlap index: 0.37, p=0.02). Additionally, MDA-MB-231 spheroids had slightly lower FLIRR values than the MCF-10A spheroids on Day 0, regardless of collagen concentration.

5.3.3 FLIRR spatial trends as a function of distance from the edge

The metabolic spatial gradients across the spheroids were measured to evaluate how they were modified over time and across cell lines and collagen concentrations. All the MCF-10A and MDA-MB-231 spheroids at Day 0 showed pronounced spatial patterns in terms of their FLIRR values as a function of a distance from the spheroid edge in Figure 5.4d-f. There were larger FLIRR values in the cells closest to the spheroid edge, while cells closer to the core tended to have smaller FLIRR values. The MCF-10A spheroids in 1

mg/mL collagen displayed little difference between the spatial distribution at Day 0 vs Day 3 (Figure 5.4d). The MCF-10A spheroids in 4 mg/mL collagen on Day 3 showed an increase in FLIRR values at the edge with a decrease in FLIRR values moving towards the core relative to Day 0 (Figure 5.4e). The MDA-MB-231 spheroids at Day 0 in both collagen concentrations displayed relatively similar FLIRR gradients, though steeper compared to the MCF-10A spheroids at Day 0 (Figure 5.4f). The MDA-MB-231 spheroids in 4 mg/mL collagen had larger FLIRR values at each distance bin than the 1mg/mL samples at Day 0, but both still had approximately the same gradient slope over the distance bins.

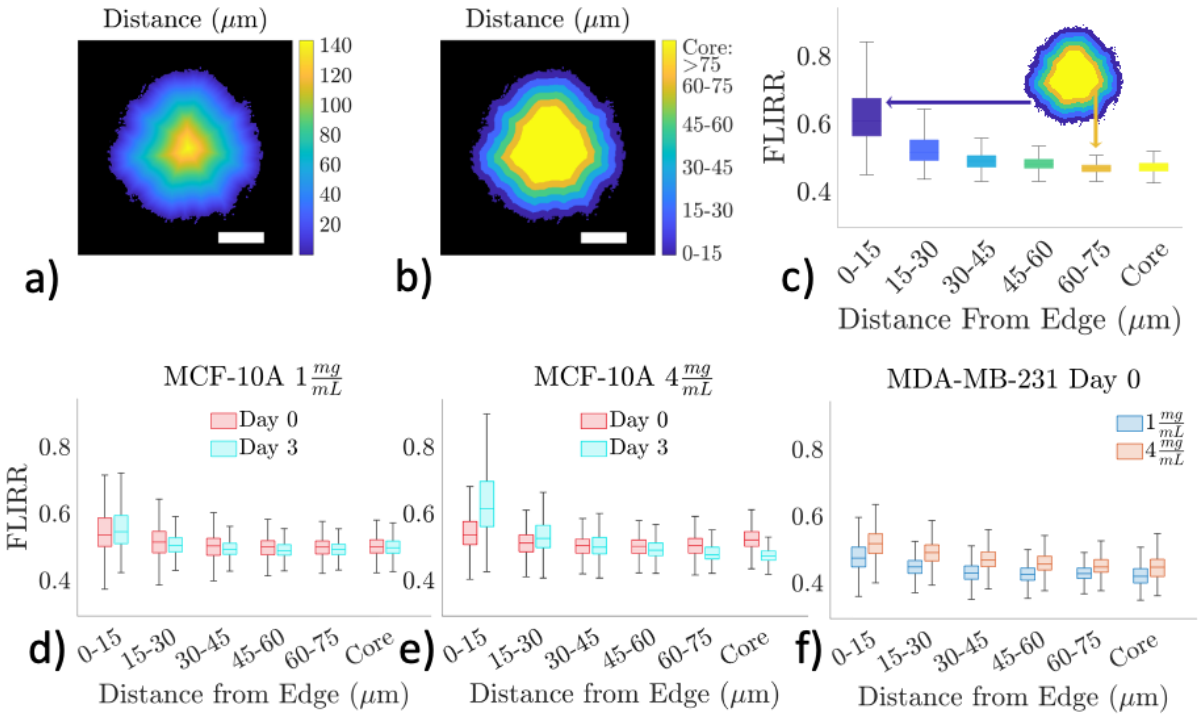

Figure 5.4. FLIRR gradients as distances from the edge. a) Map of Euclidian Distance transform where each pixel's value represents distance to the nearest edge pixel. b) Discretized distance from the edge map with each color representing a 15um step size. Values greater than 75um are considered as the core. Scale bars (white) indicate 100 µm. c) Representative example of FLIRR vs Distance from the edge plot. For each discretized

distance in b) the FLIRR values for those pixels are displayed as a boxplot. Pooled FLIRR vs Distance from the edge for MCF-10A are shown for d) 1mg/mL and e) 4mg/mL with Day 0 (red) and Day 3 (turquoise). f) Pooled FLIRR vs Distance from the edge for MDA-MB-231 at Day 0 with 1mg/mL (blue) and 4mg/mL (orange). All of the MCF-10A spheroids and the MDA-MB-231 spheroids at Day 0 displayed enhanced FLIRR values closer to the edge relative to the core with the MCF-10A spheroids on Day 3 at 4 mg/mL displaying the most prominent gradient.

5.3.4 FLIRR spatial trends as a function of distance from centroid

The metabolic spatial gradients in the MDA-MB-231 spheroids at Day 3 was measured to see how FLIRR values changed as a function of migration distance. MDA-MB-231 spheroids in both collagen concentrations at Day 3 displayed trends of increasing FLIRR values in the cells farthest away from the centroid in Figure 5.5c. The 1mg/mL samples had a much steeper gradient than the 4mg/mL samples, with the cells farthest away from the centroid having larger FLIRR values and cells closer to the centroid having lower FLIRR values.

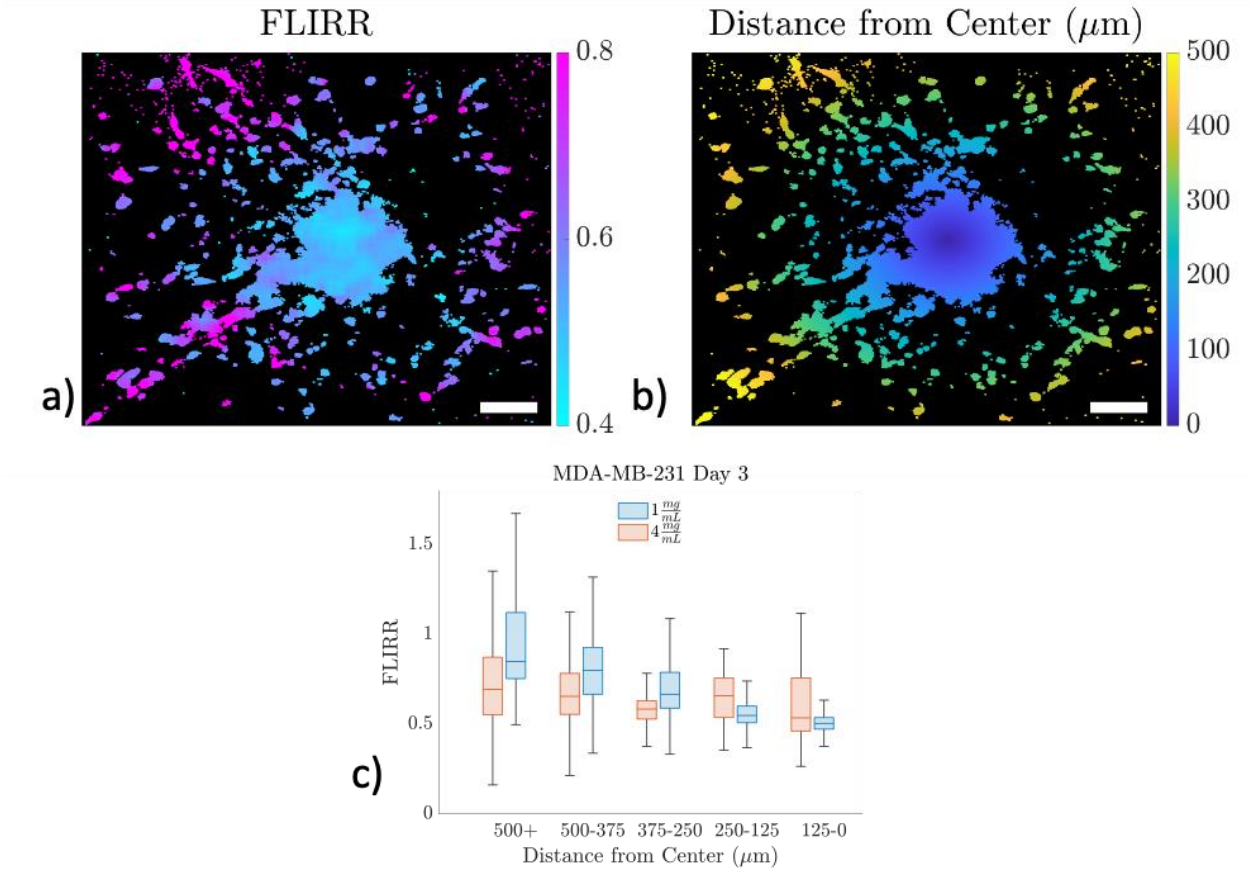

Figure 5.5. FLIRR gradients as distance from the centroid. a) FLIRR map of an MDA-MB-231 spheroid in 1 mg/mL on Day 3. b) Euclidian distance transform from the centroid of the spheroid where each pixel represents the distance away from the centroid. Scale bars (white) indicate 100 µm. c) FLIRR vs Distance from the centroid plot for MDA-MB-231 at Day 3 comparing 1mg/mL (blue) vs 4 mg/mL (red). In these samples, the cells that had migrated the farthest had a preferential shift towards larger FLIRR values consistent with a shift towards OXPHOS.

5.4 Discussion

This work helps to demonstrate the utility of FLIM to non-invasively track the spatial metabolic patterns of breast cancer spheroids in a 3D microenvironment. Importantly, the metabolic profile of each cell line was modulated by collagen concentration and time. The MCF-10A spheroids had a relatively small shift towards smaller FLIRR values over

time, while the MDA-MB-231 samples shifted towards larger FLIRR values over time, a shift consistent with OXPHOS, with a more pronounced effect at the higher collagen concentration. Importantly, spatial metabolic gradients were demonstrated across the entire spheroid in both invasive and non-invasive breast cells derived spheroids.

The MCF-10A cell line has been extensively characterized as non-invasive model for normal breast tissue (Imbalzano et al., 2009). The MCF-10A spheroids shifted towards lower FLIRR values over time, with more prominent shifts occurring at higher collagen concentrations. A shift towards lower FLIRR values has been previously shown to be consistent with a shift towards glycolysis (Wallrabe et al., 2018). Other groups have observed breast and lung cancer cells shift towards glycolysis when embedded in higher collagen concentrations (Kim et al., 2019; Mah et al., 2018; Morris et al., 2016; Park et al., 2020). For example, increases in collagen density induced a shift in 3D breast cancer spheroids: 4T07 and 4T1 towards increased glucose metabolism and decreased oxygen consumption rate in the tricarboxylic acid (TCA) cycle (Morris et al., 2016).

The MDA-MB-231 cell line has been characterized as a highly invasive breast cancer model (Cailleau et al., 1978). The MDA-MB-231 spheroids have lower FLIRR values at Day 0 compared to MCF-10A spheroids, which may be indicative of increased glycolysis, as previously observed through significantly increased lactate production, and decreased mitochondria reduction activity (Zancan et al., 2010). A low overlap index

(~0.4) on Day 0 comparing MDA-MB-231 samples with MCF-10A samples, characterized the large baseline differences between the cell lines (Figure S5.1).

The MDA-MB-231 samples from Day 0 to 3 displayed significantly different proliferation and migration characteristics between the 1 mg/mL and 4 mg/mL collagen concentrations (Figure 5.2). In the MDA-MB-231 spheroids, the increase in spheroid area in the 1 mg/mL from Day 0 to Day 3 (Figure 5.2a) potentially indicates that these spheroids were proliferative at the low collagen concentration in contrast to the 4 mg/mL, where a decrease in spheroid area indicates a lack of proliferation. The MDA-MB-231 spheroids on Day 3 in 1 mg/mL collagen showed a substantially farther migratory extent than the intact spheroids (~500 vs 300 μm, while the 4 mg/mL samples on Day 3 had a much larger migratory extent overall (~800 μm). These differences in the proliferative and migratory characteristics potentially indicate that the 1 mg/mL collagen MDA-MB-231 samples were a mix of proliferative and migratory phenotypes compared to the 4 mg/mL collagen MDA-MB-231 samples which shifted to a predominantly migratory phenotype. This aligns with prior work evaluating MDA-MB-231 3D spheroids in collagen/alginate hybrid hydrogels with modifiable stiffness, where a softer environment drove proliferation while a stiffer environment induced a shift towards migration (C. Liu et al., 2021).

Proliferating and migrating cancer cells have been shown to have different metabolic demand and rely on different metabolic pathways (Zanotelli et al., 2021). In the previous

work done by Liu et al. the authors described how genetic enrichment analysis revealed that MDA-MB-231 spheroids exposed to stiffer environments with increased migratory phenotypes had an upregulation of OXPHOS and fatty acid metabolism genes and downregulation of glycolysis genes compared to softer environments (C. Liu et al., 2021). This is consistent with the increase in FLIRR observed for MDA-MB-231 spheroids at Day 3 with a larger increase in FLIRR in the 4 mg/mL samples with the greater cell migration compared to the lower collagen concentration.

Since the MCF-10A cells did not invade through the collagen and remained as intact spheroids, it is difficult to ascertain whether these spheroids continued to proliferate in either collagen concentration. Healthy epithelial cells, like MCF-10A, experience contact inhibition which normally inhibits proliferation when the cell density reaches a threshold (Pavel et al., 2018). However, a stiff ECM has shown to be able to downregulate this contact inhibition causing an increase in proliferation and inducing a malignant phenotype in MCF-10A cells through YAP/TAZ activation. (Chaudhuri et al., 2014; Pavel et al., 2018). This malignant transformation may also explain the shift towards lower FLIRR values by starting to induce the Warburg effect and shift towards glycolysis (Liberti & Locasale, 2016; Warburg et al., 1927).

Interestingly, as shown in Figure 5.4d, e, while there was an overall small shift towards lower FLIRR values in the MCF-10A samples from Day 0 to Day 3, the cells closest to the edge had an increase in FLIRR values. In the 4mg/mL MCF-10A sample at Day 3,

this trend was particularly enhanced. The cells closest to the edge of the spheroid would be directly engaging with the collagen and presumably have the largest response to increased stiffness of collagen gel at higher concentrations and may represent cells in a pre-invasive phenotype (Chaudhuri et al., 2014). The invasion transformation of MCF-10A cells may take longer than the timepoint of Day 3 when the spheroids were imaged (Kang et al., 2021). Similarly, MDA-MB-231 cells at Day 0 in both collagen concentrations had lower values closer to the core and elevated FLIRR values towards the edge, which may be starting to shift from a purely proliferative phenotype to a migratory phenotype (Cunniff et al., 2016; LeBleu et al., 2014).

In the MDA-MB-231 spheroids on Day 3, there were increasing FLIRR values as a function of distance away from the core (Figure 5.5c). In the 1mg/mL samples, the cells that had travelled the farthest from the core had a larger increase in FLIRR values, while cells closer to the core had lower FLIRR values. The 4mg/mL MDA-MB-231 spheroids at Day 3 had a more modest FLIRR gradient as a function of distance from the core. However, for those spheroids there was not an aggregation of cancer cells at the core, rather all the cells were migratory and invaded into the collagen.

Prior work has found that the leading invasive edge of cancer spheroids shift their metabolism towards OXPHOS to meet the energy demands of invasion (Ashton et al., 2018; LeBleu et al., 2014; Zanotelli et al., 2021). Other groups have shown that MDA-MB-231 migration in stiffer collagen gels corresponds to an increase in glucose uptake

and ATP/ADP ratio (Zhang et al., 2019). Cancer cells on the leading edge of migration have been shown to have increased number of mitochondria and ATP output (Cunniff et al., 2016). The leader cells of those migrating cells had increased metabolic output compared to the follower cells and may explain the FLIRR gradients as a function of distance of center. Additionally, Davis et al. showed that primary MDA-MB-231 tumor cells were significantly more glycolytic and underwent less OXPHOS compared to the matched micrometastatic cells using single-cell RNA sequencing, flow cytometry and qPCR (Davis et al., 2020). In that work, inhibiting OXPHOS in MDA-MB-231 cells inoculated in mice significantly decreased the number of metastases found in the lungs demonstrating the need for OXPHOS in the migration cascade. Understanding the phenotypic metabolic changes underlying how cancer cells migrate would be critical to develop metabolic therapies that are able to target aspects of the metastatic cascade (Faubert et al., 2020).

This work did not confirm the differences in metabolic profiles and proliferation through *ex vivo* molecular analysis techniques such as RNA sequencing. The exact stiffness of the 1mg/mL and 4mg/mL collagen concentrations was not measured; however, prior work has shown collagen concentration correlates with rheology measurements of stiffness (DeCamp et al., 2020; Mah et al., 2018). Additionally, our model of ECM consisted of only collagen and did not include other critical features of the ECM such as fibroblasts. There were only a limited number of replicate spheroids per condition (n=3).

In summary, this work demonstrated that FLIM can non-invasively monitor the metabolic profile of live 3D breast cancer spheroids. The MCF-10A and MDA-MB-231 samples differentially shifted their metabolic profile in response to modifications to the collagen concentration of the ECM. The physical properties of the ECM also impacted the proliferative vs migratory phenotype of MDA-MB-231 cells. Finally, FLIM was able to reveal spatial metabolic gradients across individual spheroids. FLIM's ability to non-invasively probe the metabolic profile while preserving the spatial information makes it a critical tool to longitudinally track metabolic changes in 3D samples.

Acknowledgements

We would like to thank the BU Neurophotonics Center (NPC) and Jack Giblin for their assistance in imaging. This work was supported in part by the US Department of Defense (award no. W81XWH-15-1-0070) and the National Science Foundation (award no. 1830878).

5.5 Supplemental

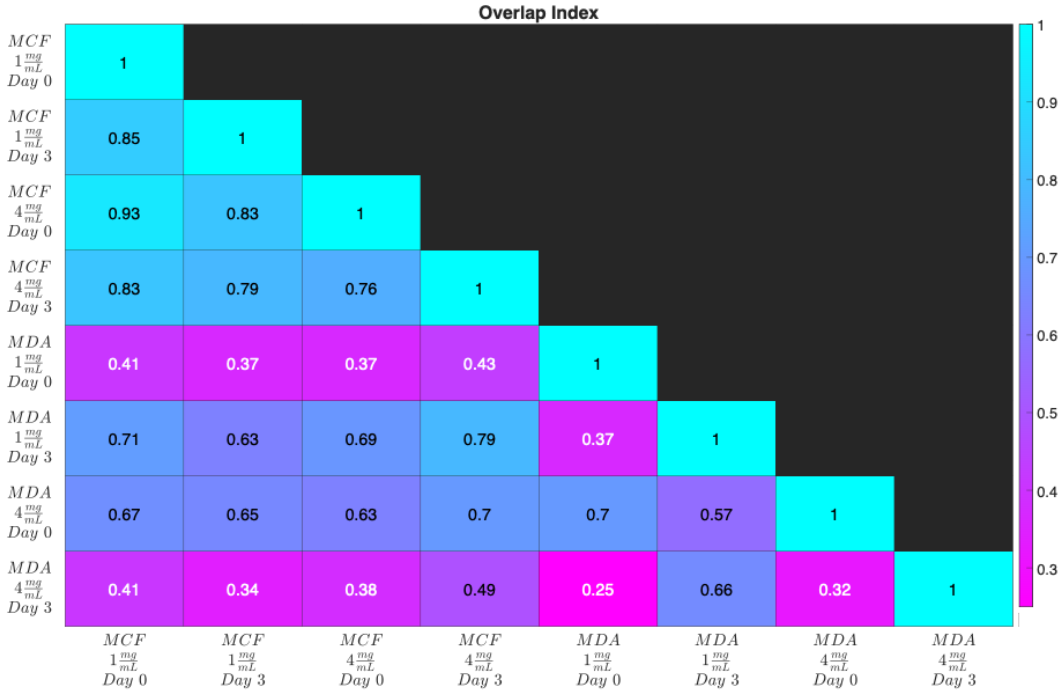

Figure S5.1 Overlap Index Heatmap. The overlap index is computed for each unique combination of cell line, collagen concentration and timepoint and displayed with its value and the color coded.

Chapter 6: Conclusions and Future Directions

6.1 Conclusions

In this dissertation, chapters 3,4, and 5 describe the utility of non-invasive imaging tools to study breast cancer at multiple scales in models ranging from breast cancer patients to mouse models, to 3D spheroids.

DOSI was shown to be a powerful tool capable of discovering prognostic biomarkers. The validation of the oxyhemoglobin flare is extremely promising since it occurs day 1 into treatment, allowing rapid feedback into the effectiveness of treatment and allowing adaptive treatments. Additionally, for the first time, the specific treatment regimen was shown to affect the manifestation of prognostic biomarkers. This raises a critical point for future clinical trial design as heterogenous treatments may obfuscate biomarkers when analyzed in overall populations.

SFDI was shown to be a powerful research tool for murine breast cancer monitoring. Its ease of use and rapid, widefield capabilities make it a very useful tool to longitudinally measure breast tumors. Optical scattering was validated as a powerful prognostic biomarker for treatment response in an immune responsive-resistant model. This raises the potential for scattering to be a prognostic biomarker that could be validated in the clinic using DOSI.

Finally, FLIM was shown to be useful tool for non-invasively being able to measure metabolic profiles in live cancer spheroids. Cancer cell migration and metabolic profiles were modulated by modifying the collagen concentration of its ECM. Spatial metabolic gradients were discovered in both non-invasive and invasive breast cell lines and demonstrates the importance of using a spatially resolved method such as FLIM to investigate metabolic perturbations.

6.2 Future Directions

The work described in this dissertation provides many imaging opportunities in the future. The clinical breast cancer tumor monitoring field's future is particularly interesting. It will be critical to understand how prognostic biomarkers would be integrate into the clinical setting. It is clear in the NAC setting if a biomarker, with 100% accuracy, could identify patients as pCR or as those with progressive disease, they would finish their treatment or progress to surgery, respectively. It is less clear, what the clinical course of action would be if an oncologist knew the tumor size would reduce by 50%. A practical implantation would be to measure a subgroup of patients where there is a clear first- and second-line treatment such as HER2+ patients. Currently, patients receiving trastuzumab who do not have a pCR to neoadjuvant therapy continue to receive trastuzumab in the adjuvant setting (NCCN, 2022). The KATHERINE trial established that those non-pCR patients benefitted from receiving an antibody-drug conjugate (ADC), trastuzumab-emtansine rather than trastuzumab (von Minckwitz et al., 2019). A simple prospective clinical trial could be to measure HER2+ NAC patients with DOSI

and if patients are predicted to be non-pCR immediately proceed with surgery and continue treating with trastuzumab-emtansine with an outcome of survival.

Similarly, it would be of interest if DOSI could be used as a clinical source of validating a mechanism of action or biomarker. For example, as demonstrated in Chapter 4, optical scattering served as a promising prognostic biomarker in a mouse model, DOSI could be used to determine if scattering could serve as a useful prognostic parameter in breast cancer patients using existing trial frameworks. Additionally, as discussed in Chapter 5, OXPHOS has been implicated in disease progression and metastasis and is currently being investigated in trials as a target for inhibition (Ashton et al., 2018). DOSI is an easily integrated tool in the clinical trial setting to non-invasively observe longitudinal changes in tumor oxygenation as a result of OXPHOS inhibition and understand its relationship with treatment response.

All three of the imaging modalities: DOSI, SFDI, and FLIM are non-invasive label free imaging modalities whose ease of use should make them a logical addition to biology studies. These imaging modalities provide information through non-invasive means that could usually only be obtained through invasive destructive techniques, unfeasible for longitudinal monitoring. These three modalities operate on very different length scales and can all provide critical feedback about the response and progression of cancer.

BIBLIOGRAPHY

Abotaleb, M., Kubatka, P., Caprnda, M., Varghese, E., Zolakova, B., Zubor, P., Opatrilova, R., Kruzliak, P., Stefanicka, P., & Büsselberg, D. (2018). Chemotherapeutic agents for the treatment of metastatic breast cancer: An update. *Biomedicine & Pharmacotherapy*, *101*, 458–477. https://doi.org/10.1016/j.biopha.2018.02.108

Alfarouk, K. O., Stock, C. M., Taylor, S., Walsh, M., Muddathir, A. K., Verduzco, D., Bashir, A. H. H., Mohammed, O. Y., Elhassan, G. O., Harguindey, S., Reshkin, S. J., Ibrahim, M. E., & Rauch, C. (2015). Resistance to cancer chemotherapy: Failure in drug response from ADME to P-gp. *Cancer Cell International*, *15*(1), 1–13. https://doi.org/10.1186/s12935-015-0221-1

Al-Masri, M., Paliotti, K., Tran, R., Halaoui, R., Lelarge, V., Chatterjee, S., Wang, L.-T., Moraes, C., & McCaffrey, L. (2021). Architectural control of metabolic plasticity in epithelial cancer cells. *Communications Biology*, *4*(1), 371. https://doi.org/10.1038/s42003-021-01899-4

Altoe, M., Gunther, J., Lim, E., Marone, A., Kim, H. K., Ha, R. S., Hibshoosh, H., Kalinsky, K., Hershman, D., & Hielscher, A. H. (2018). *Neoadjuvent Therapy Monitoring in Breast Cancer Patients with Diffuse Optical Tomography*. *2018*, CTu4B.6. https://doi.org/10.1364/translational.2018.ctu4b.6

Applegate, M. B., Istfan, R. E., Spink, S., Tank, A., & Roblyer, D. (2020). Recent advances in high speed diffuse optical imaging in biomedicine. *APL Photonics*, *5*(4). https://doi.org/10.1063/1.5139647

Ashton, T. M., McKenna, W. G., Kunz-Schughart, L. A., & Higgins, G. S. (2018). Oxidative Phosphorylation as an Emerging Target in Cancer Therapy. *Clinical Cancer Research*, *24*(11), 2482–2490. https://doi.org/10.1158/1078-0432.CCR-17-3070

Asselain, B., Barlow, W., Bartlett, J., Bergh, J., Bergsten-Nordström, E., Bliss, J., Boccardo, F., Boddington, C., Bogaerts, J., Bonadonna, G., Bradley, R., Brain, E., Braybrooke, J., Broet, P., Bryant, J., Burrett, J., Cameron, D., Clarke, M., Coates, A., … Zujewski, J. A. (2018). Long-term outcomes for neoadjuvant versus adjuvant chemotherapy in early breast cancer: meta-analysis of individual patient data from ten randomised trials. *The Lancet Oncology*, *19*(1), 27–39. https://doi.org/10.1016/S1470-2045(17)30777-5

Avril, S., Muzic, R. F., Plecha, D., Traughber, B. J., Vinayak, S., & Avril, N. (2016). 18F-FDG PET/CT for Monitoring of Treatment Response in Breast Cancer. *Journal of Nuclear Medicine*, *57*(Supplement_1), 34S-39S. https://doi.org/10.2967/jnumed.115.157875

Baker, E. L., Bonnecaze, R. T., & Zaman, M. H. (2009). Extracellular Matrix Stiffness and Architecture Govern Intracellular Rheology in Cancer. *Biophysical Journal*, *97*(4), 1013–1021. https://doi.org/10.1016/j.bpj.2009.05.054

Barker, A. D., Sigman, C. C., Kelloff, G. J., Hylton, N. M., Berry, D. A., & Esserman, L. J. (2009). I-SPY 2: An adaptive breast cancer trial design in the setting of

neoadjuvant chemotherapy. *Clinical Pharmacology and Therapeutics*, *86*(1), 97–100. https://doi.org/10.1038/clpt.2009.68

Beard, P. (2011). Biomedical photoacoustic imaging. *Interface Focus*, *1*(4), 602–631. https://doi.org/10.1098/rsfs.2011.0028

Bertolini, F., Paul, S., Mancuso, P., Monestiroli, S., Gobbi, A., Shaked, Y., & Kerbel, R. S. (2003). Maximum tolerable dose and low-dose metronomic chemotherapy have opposite effects on the mobilization and viability of circulating endothelial progenitor cells. *Cancer Research*, *63*(15), 4342–4346.

Bevilacqua, F., Berger, A. J., Cerussi, A. E., Jakubowski, D., & Tromberg, B. J. (2000). Broadband absorption spectroscopy in turbid media by combined frequency-domain and steady-state methods. *Applied Optics*, *39*(34), 6498. https://doi.org/10.1364/AO.39.006498

Bird, D. K., Yan, L., Vrotsos, K. M., Eliceiri, K. W., Vaughan, E. M., Keely, P. J., White, J. G., & Ramanujam, N. (2005). Metabolic Mapping of MCF10A Human Breast Cells via Multiphoton Fluorescence Lifetime Imaging of the Coenzyme NADH. *Cancer Research*, *65*(19), 8766–8773. https://doi.org/10.1158/0008-5472.CAN-04-3922

Boyd, N. F., Byng, J. W., Jong, R. A., Fishell, E. K., Little, L. E., Miller, A. B., Lockwood, G. A., Tritchler, D. L., & Yaffe, M. J. (1995). Quantitative Classification of Mammographic Densities and Breast Cancer Risk: Results From the Canadian National Breast Screening Study. *JNCI Journal of the National Cancer Institute*, *87*(9), 670–675. https://doi.org/10.1093/jnci/87.9.670

Bracci, L., Schiavoni, G., Sistigu, A., & Belardelli, F. (2014). Immune-based mechanisms of cytotoxic chemotherapy: implications for the design of novel and rationale-based combined treatments against cancer. *Cell Death & Differentiation*, *21*(1), 15–25. https://doi.org/10.1038/cdd.2013.67

Bradley, D., & Roth, G. (2011). Adaptive Thresholding using the Integral Image. *Journal of Graphics Tools*, *12*(2), 13–21. https://doi.org/10.1080/2151237x.2007.10129236

Cailleau, R., Olivé, M., & Cruciger, Q. V. J. (1978). Long-term human breast carcinoma cell lines of metastatic origin: Preliminary characterization. *In Vitro*, *14*(11), 911–915. https://doi.org/10.1007/BF02616120

Cerussi, A. E., Tanamai, V. W., Hsiang, D., Butler, J., Mehta, R. S., & Tromberg, B. J. (2011). Diffuse optical spectroscopic imaging correlates with final pathological response in breast cancer neoadjuvant chemotherapy. *Philosophical Transactions of the Royal Society A: Mathematical, Physical and Engineering Sciences*, *369*(1955), 4512–4530. https://doi.org/10.1098/rsta.2011.0279

Cerussi, A., Shah, N., Hsiang, D., Durkin, A., Butler, J., & Tromberg, B. J. (2006). In vivo absorption, scattering, and physiologic properties of 58 malignant breast tumors determined by broadband diffuse optical spectroscopy.

Journal of Biomedical Optics, *11*(4), 044005. https://doi.org/10.1117/1.2337546

Chan, T. F., & Vese, L. A. (2001). Active contours without edges. *IEEE Transactions on Image Processing*, *10*(2), 266–277. https://doi.org/10.1109/83.902291

Chaudhuri, O., Koshy, S. T., Branco da Cunha, C., Shin, J.-W., Verbeke, C. S., Allison, K. H., & Mooney, D. J. (2014). Extracellular matrix stiffness and composition jointly regulate the induction of malignant phenotypes in mammary epithelium. *Nature Materials*, *13*(10), 970–978. https://doi.org/10.1038/nmat4009

Chen, C.-S., Doloff, J. C., & Waxman, D. J. (2015). Intermittent Metronomic Drug Schedule Is Essential for Activating Antitumor Innate Immunity and Tumor Xenograft Regression. *Neoplasia*, *16*(1), 84-W27. https://doi.org/10.1593/neo.131910

Cochran, J. M., Busch, D. R., Leproux, A., Zhang, Z., O'Sullivan, T. D., Cerussi, A. E., Carpenter, P. M., Mehta, R. S., Roblyer, D., Yang, W., Paulsen, K. D., Pogue, B., Jiang, S., Kaufman, P. A., Chung, S. H., Schnall, M., Snyder, B. S., Hylton, N., Carp, S. A., … Yodh, A. G. (2018). Tissue oxygen saturation predicts response to breast cancer neoadjuvant chemotherapy within 10 days of treatment. *Journal of Biomedical Optics*, *24*(02), 1. https://doi.org/10.1117/1.JBO.24.2.021202

Cochran, J. M., Chung, S. H., Leproux, A., Baker, W. B., Busch, D. R., DeMichele, A. M., Tchou, J., Tromberg, B. J., & Yodh, A. G. (2017). Longitudinal optical monitoring of blood flow in breast tumors during neoadjuvant chemotherapy. *Physics in Medicine and Biology*, *62*(12), 4637–4653. https://doi.org/10.1088/1361-6560/aa6cef

Cortazar, P., Zhang, L., Untch, M., Mehta, K., Costantino, J. P., Wolmark, N., Bonnefoi, H., Cameron, D., Gianni, L., Valagussa, P., Swain, S. M., Prowell, T., Loibl, S., Wickerham, D. L., Bogaerts, J., Baselga, J., Perou, C., Blumenthal, G., Blohmer, J., … von Minckwitz, G. (2014). Pathological complete response and long-term clinical benefit in breast cancer: the CTNeoBC pooled analysis. *The Lancet*, *384*(9938), 164–172. https://doi.org/10.1016/S0140-6736(13)62422-8

Cuccia, D. J., Bevilacqua, F., Durkin, A. J., Ayers, F. R., & Tromberg, B. J. (2009). Quantitation and mapping of tissue optical properties using modulated imaging. *Journal of Biomedical Optics*, *14*(2), 024012. https://doi.org/10.1117/1.3088140

Cuccia, D. J., Bevilacqua, F., Durkin, A. J., & Tromberg, B. J. (2005). Modulated imaging: quantitative analysis and tomography of turbid media in the spatial-frequency domain. *Optics Letters*, *30*(11), 1354. https://doi.org/10.1364/ol.30.001354

Cunniff, B., McKenzie, A. J., Heintz, N. H., & Howe, A. K. (2016). AMPK activity regulates trafficking of mitochondria to the leading edge during cell

migration and matrix invasion. *Molecular Biology of the Cell*, *27*(17), 2662–2674. https://doi.org/10.1091/mbc.e16-05-0286

Danishada, K. K. A., Sharmaa, U., Saha, R. G., Seenub, V., Parshadb, R., & Jagannathan, N. R. (2010). Assessment of therapeutic response of locally advanced breast cancer (LABC) patients undergoing neoadjuvant chemotherapy (NACT) monitored using sequential magnetic resonance spectroscopic imaging (MRSI). *NMR in Biomedicine*, *23*(3), 233–241. https://doi.org/10.1002/nbm.1436

Datta, R., Heaster, T. M., Sharick, J. T., Gillette, A. A., & Skala, M. C. (2020). Fluorescence lifetime imaging microscopy: fundamentals and advances in instrumentation, analysis, and applications. *Journal of Biomedical Optics*, *25*(07), 1. https://doi.org/10.1117/1.JBO.25.7.071203

Davis, R. T., Blake, K., Ma, D., Gabra, M. B. I., Hernandez, G. A., Phung, A. T., Yang, Y., Maurer, D., Lefebvre, A. E. Y. T., Alshetaiwi, H., Xiao, Z., Liu, J., Locasale, J. W., Digman, M. A., Mjolsness, E., Kong, M., Werb, Z., & Lawson, D. A. (2020). Transcriptional diversity and bioenergetic shift in human breast cancer metastasis revealed by single-cell RNA sequencing. *Nature Cell Biology*, *22*(3), 310–320. https://doi.org/10.1038/s41556-020-0477-0

DeCamp, S. J., Tsuda, V. M. K., Ferruzzi, J., Koehler, S. A., Giblin, J. T., Roblyer, D., Zaman, M. H., Weiss, S. T., Kılıç, A., de Marzio, M., Park, C. Y., Ogassavara, N. C., Mitchel, J. A., Butler, J. P., & Fredberg, J. J. (2020). Epithelial layer unjamming shifts energy metabolism toward glycolysis. *Scientific Reports*, *10*(1), 18302. https://doi.org/10.1038/s41598-020-74992-z

Dehdashti, F., Mortimer, J. E., Trinkaus, K., Naughton, M. J., Ellis, M., Katzenellenbogen, J. A., Welch, M. J., & Siegel, B. A. (2009). PET-based estradiol challenge as a predictive biomarker of response to endocrine therapy in women with estrogen-receptor-positive breast cancer. *Breast Cancer Research and Treatment*, *113*(3), 509–517. https://doi.org/10.1007/s10549-008-9953-0

Dieci, M. V., Miglietta, F., & Guarneri, V. (2021). Immune Infiltrates in Breast Cancer: Recent Updates and Clinical Implications. *Cells*, *10*(2), 1–27. https://doi.org/10.3390/CELLS10020223

Dieci, M. V., Radosevic-Robin, N., Fineberg, S., van den Eynden, G., Ternes, N., Penault-Llorca, F., Pruneri, G., D'Alfonso, T. M., Demaria, S., Castaneda, C., Sanchez, J., Badve, S., Michiels, S., Bossuyt, V., Rojo, F., Singh, B., Nielsen, T., Viale, G., Kim, S.-R., … Salgado, R. (2018). Update on tumor-infiltrating lymphocytes (TILs) in breast cancer, including recommendations to assess TILs in residual disease after neoadjuvant therapy and in carcinoma in situ: A report of the International Immuno-Oncology Biomarker Working Group on Bre. *Seminars in Cancer Biology*, *52*(September 2017), 16–25. https://doi.org/10.1016/j.semcancer.2017.10.003

Doloff, J. C., & Waxman, D. J. (2012). VEGF receptor inhibitors block the ability of metronomically dosed cyclophosphamide to activate innate immunity-

induced tumor regression. *Cancer Research*, *72*(5), 1103–1115. https://doi.org/10.1158/0008-5472.CAN-11-3380

Du, B., & Waxman, D. J. (2020). Medium dose intermittent cyclophosphamide induces immunogenic cell death and cancer cell autonomous type I interferon production in glioma models. *Cancer Letters*, *470*, 170–180. https://doi.org/10.1016/J.CANLET.2019.11.025

Emens, L. A. (2018). Breast Cancer Immunotherapy: Facts and Hopes. *Clinical Cancer Research*, *24*(3), 511–520. https://doi.org/10.1158/1078-0432.CCR-16-3001

Esserman, L. J., & DeMichele, A. (2014). Accelerated approval for pertuzumab in the neoadjuvant setting: Winds of change? *Clinical Cancer Research*, *20*(14), 3632–3636. https://doi.org/10.1158/1078-0432.CCR-13-3131

Falou, O., Soliman, H., Sadeghi-Naini, A., Iradji, S., Lemon-Wong, S., Zubovits, J., Spayne, J., Dent, R., Trudeau, M., Boileau, J. F., Wright, F. C., Yaffe, M. J., & Czarnota, G. J. (2014). Diffuse Optical Spectroscopy Evaluation of Treatment Response in Women with Locally Advanced Breast Cancer Receiving Neoadjuvant Chemotherapy. *Translational Oncology*, *5*(4), 238–246. https://doi.org/10.1593/tlo.11346

Faubert, B., Solmonson, A., & DeBerardinis, R. J. (2020). Metabolic reprogramming and cancer progression. *Science*, *368*(6487). https://doi.org/10.1126/science.aaw5473

FDA. (2014). Guidance for Industry: Pathologic Complete Response in Early-Stage Breast Cancer: Use as an Endpoint to Support Accelerated Approval. *[Online], Http://Www.Fda.Gov/Downloads/Drugs/ Guidancecomplianceregulatoryinformation/Guidances/ Ucm305501.Pdf*, *October*, 1–7.

Georgakoudi, I., & Quinn, K. P. (2012). Optical Imaging Using Endogenous Contrast to Assess Metabolic State. *Annual Review of Biomedical Engineering*, *14*(1), 351–367. https://doi.org/10.1146/annurev-bioeng-071811-150108

Gibson, A., & Dehghani, H. (2009). Diffuse optical imaging. *Philosophical Transactions of the Royal Society A: Mathematical, Physical and Engineering Sciences*, *367*(1900), 3055–3072. https://doi.org/10.1098/rsta.2009.0080

Gioux, S., Mazhar, A., & Cuccia, D. J. (2019). Spatial frequency domain imaging in 2019: principles, applications, and perspectives. *Journal of Biomedical Optics*, *24*(07), 1. https://doi.org/10.1117/1.JBO.24.7.071613

Graham, L. J., Shupe, M. P., Schneble, E. J., Flynt, F. L., Clemenshaw, M. N., Kirkpatrick, A. D., Gallagher, C., Nissan, A., Henry, L., Stojadinovic, A., Peoples, G. E., & Shumway, N. M. (2014). Current Approaches and Challenges in Monitoring Treatment Responses in Breast Cancer. *Journal of Cancer*, *5*(1), 58–68. https://doi.org/10.7150/jca.7047

Grivennikov, S. I., Greten, F. R., & Karin, M. (2010). Immunity, Inflammation, and Cancer. *Cell*, *140*(6), 883–899. https://doi.org/10.1016/j.cell.2010.01.025

Gunther, J. E., Lim, E. A., Kim, H. K., Flexman, M., Altoé, M., Campbell, J. A., Hibshoosh, H., Crew, K. D., Kalinsky, K., Hershman, D. L., & Hielscher, A. H. (2018). Dynamic Diffuse Optical Tomography for Monitoring Neoadjuvant Chemotherapy in Patients with Breast Cancer. *Radiology*, *000*(0), 161041. https://doi.org/10.1148/radiol.2018161041

Hamy, A.-S., Darrigues, L., Laas, E., de Croze, D., Topciu, L., Lam, G.-T., Evrevin, C., Rozette, S., Laot, L., Lerebours, F., Pierga, J.-Y., Osdoit, M., Faron, M., Feron, J.-G., Laé, M., & Reyal, F. (2020). Prognostic value of the Residual Cancer Burden index according to breast cancer subtype: Validation on a cohort of BC patients treated by neoadjuvant chemotherapy. *PLOS ONE*, *15*(6), e0234191. https://doi.org/10.1371/journal.pone.0234191

Hanahan, D., Bergers, G., & Bergsland, E. (2000). Less is, more, regularly: Metronomic dosing of cytotoxic drugs can target tumor angiogenesis in mice. In *Journal of Clinical Investigation* (Vol. 105, Issue 8, pp. 1045–1047). https://doi.org/10.1172/JCI9872

Hanahan, D., & Weinberg, R. A. (2011). Hallmarks of Cancer: The Next Generation. *Cell*, *144*(5), 646–674. https://doi.org/10.1016/j.cell.2011.02.013

Haskell, R. C., Svaasand, L. O., Tsay, T.-T., Feng, T.-C., Tromberg, B. J., & McAdams, M. S. (1994). Boundary conditions for the diffusion equation in radiative transfer. *Journal of the Optical Society of America A*, *11*(10), 2727. https://doi.org/10.1364/JOSAA.11.002727

Helmchen, F., & Denk, W. (2005). Deep tissue two-photon microscopy. *Nature Methods*, *2*(12), 932–940. https://doi.org/10.1038/nmeth818

Hendry, S. A., Farnsworth, R. H., Solomon, B., Achen, M. G., Stacker, S. A., & Fox, S. B. (2016). The Role of the Tumor Vasculature in the Host Immune Response: Implications for Therapeutic Strategies Targeting the Tumor Microenvironment. *Frontiers in Immunology*, *7*(December), 1–21. https://doi.org/10.3389/fimmu.2016.00621

Hielscher, A. H., Mourant, J. R., & Bigio, I. J. (1997). Influence of particle size and concentration on the diffuse backscattering of polarized light from tissue phantoms and biological cell suspensions. *Applied Optics*, *36*(1), 125. https://doi.org/10.1364/ao.36.000125

Hoiland, R. L., Bain, A. R., Rieger, M. G., Bailey, D. M., & Ainslie, P. N. (2016). Hypoxemia, oxygen content, and the regulation of cerebral blood flow. *American Journal of Physiology - Regulatory Integrative and Comparative Physiology*, *310*(5), R398–R413. https://doi.org/10.1152/ajpregu.00270.2015

Hou, J., Wright, H. J., Chan, N., Tran, R., Razorenova, O. v., Potma, E. O., & Tromberg, B. J. (2016). Correlating two-photon excited fluorescence imaging of breast cancer cellular redox state with seahorse flux analysis of normalized cellular oxygen consumption. *Journal of Biomedical Optics*, *21*(6), 060503. https://doi.org/10.1117/1.JBO.21.6.060503

Huber, J. P., & David Farrar, J. (2011). Regulation of effector and memory T-cell functions by type I interferon. *Immunology*, *132*(4), 466–474. https://doi.org/10.1111/j.1365-2567.2011.03412.x

Hylton, N. M., Blume, J. D., Bernreuter, W. K., Pisano, E. D., Rosen, M. A., Morris, E. A., Weatherall, P. T., Lehman, C. D., Newstead, G. M., Polin, S., Marques, H. S., Esserman, L. J., & Schnall, M. D. (2012). Locally Advanced Breast Cancer: MR Imaging for Prediction of Response to Neoadjuvant Chemotherapy—Results from ACRIN 6657/I-SPY TRIAL. *Radiology*, *263*(3), 663–672. https://doi.org/10.1148/radiol.12110748

Imbalzano, K. M., Tatarkova, I., Imbalzano, A. N., & Nickerson, J. A. (2009). Increasingly transformed MCF-10A cells have a progressively tumor-like phenotype in three-dimensional basement membrane culture. *Cancer Cell International*, *9*(1), 7. https://doi.org/10.1186/1475-2867-9-7

Insua-Rodríguez, J., & Oskarsson, T. (2016). The extracellular matrix in breast cancer. *Advanced Drug Delivery Reviews*, *97*, 41–55. https://doi.org/10.1016/j.addr.2015.12.017

Ireson, C. R., Alavijeh, M. S., Palmer, A. M., Fowler, E. R., & Jones, H. J. (2019). The role of mouse tumour models in the discovery and development of anticancer drugs. *British Journal of Cancer*, *121*(2), 101–108. https://doi.org/10.1038/s41416-019-0495-5

Jakubowski, D. B., Cerussi, A. E., Bevilacqua, F., Shah, N., Hsiang, D., Butler, J., & Tromberg, B. J. (2004). Monitoring neoadjuvant chemotherapy in breast cancer using quantitative diffuse optical spectroscopy: a case study. *Journal of Biomedical Optics*, *9*(1), 230. https://doi.org/10.1117/1.1629681

Jerman, T., Pernuš, F., Likar, B., & Špiclin, Ž. (2015). Beyond Frangi: an improved multiscale vesselness filter. In S. Ourselin & M. A. Styner (Eds.), *Medical Imaging 2015: Image Processing* (Vol. 9413, Issue April 2017, p. 94132A). https://doi.org/10.1117/12.2081147

Jiang, S., Pogue, B. W., Kaufman, P. A., Gui, J., Jermyn, M., Frazee, T. E., Poplack, S. P., DiFlorio-Alexander, R., Wells, W. A., & Paulsen, K. D. (2014). Predicting Breast Tumor Response to Neoadjuvant Chemotherapy with Diffuse Optical Spectroscopic Tomography prior to Treatment. *Clinical Cancer Research*, *20*(23), 6006–6015. https://doi.org/10.1158/1078-0432.CCR-14-1415

Kang, W., Ferruzzi, J., Spatarelu, C.-P., Han, Y. L., Sharma, Y., Koehler, S. A., Mitchel, J. A., Khan, A., Butler, J. P., Roblyer, D., Zaman, M. H., Park, J.-A., Guo, M., Chen, Z., Pegoraro, A. F., & Fredberg, J. J. (2021). A novel jamming phase diagram links tumor invasion to non-equilibrium phase separation. *IScience*, *24*(11), 103252. https://doi.org/10.1016/j.isci.2021.103252

Kareva, I., Waxman, D. J., & Lakka, G. (2015). Metronomic chemotherapy : An attractive alternative to maximum tolerated dose therapy that can activate

anti-tumor immunity and minimize therapeutic resistance. *Cancer Letters*, *358*(2), 100–106. https://doi.org/10.1016/j.canlet.2014.12.039

Karrobi, K., Tank, A., Tabassum, S., Pera, V., & Roblyer, D. (2019). Diffuse and nonlinear imaging of multiscale vascular parameters for in vivo monitoring of preclinical mammary tumors. *Journal of Biophotonics*, *12*(6), e201800379. https://doi.org/10.1002/jbio.201800379

Kaushik, G., Gil, D. A., Torr, E., Berge, E. S., Soref, C., Uhl, P., Fontana, G., Antosiewicz-bourget, J., Edington, C., Schwartz, M. P., Griffith, L. G., Thomson, J. A., Skala, M. C., Daly, W. T., & Murphy, W. L. (2019). *Quantitative Label-Free Imaging of 3D Vascular Networks Self-Assembled in Synthetic Hydrogels*. *1801186*, 1–12. https://doi.org/10.1002/adhm.201801186

Kerbel, R. S., & Kamen, B. A. (2004). The anti-angiogenic basis of metronomic chemotherapy. *Nature Reviews Cancer*, *4*(6), 423–436. https://doi.org/10.1038/nrc1369

Kim, B. G., Sung, J. S., Jang, Y., Cha, Y. J., Kang, S., Han, H. H., Lee, J. H., & Cho, N. H. (2019). Compression-induced expression of glycolysis genes in CAFs correlates with EMT and angiogenesis gene expression in breast cancer. *Communications Biology*, *2*(1), 313. https://doi.org/10.1038/s42003-019-0553-9

Koo, J. H., & Guan, K.-L. (2018). Interplay between YAP/TAZ and Metabolism. *Cell Metabolism*, *28*(2), 196–206. https://doi.org/10.1016/j.cmet.2018.07.010

Kosaka, N., Ogawa, M., Choyke, P. L., & Kobayashi, H. (2009). Clinical implications of near-infrared fluorescence imaging in cancer. *Future Oncology*, *5*(9), 1501–1511. https://doi.org/10.2217/fon.09.109

Kroon, D., & Slump, C. H. (2009). Coherence Filtering to Enhance the Mandibular Canal in Cone-Beam CT data. *Annual Symposium of the IEEE-EMBS Benelux Chapter 2009*, 41–44. http://doc.utwente.nl/73094/%5Cnhttp://eprints.eemcs.utwente.nl/18439/01/Kroon_CoherenceFiltering.pdf

Krystel-Whittemore, M., Xu, J., Brogi, E., Ventura, K., Patil, S., Ross, D. S., Dang, C., Robson, M., Norton, L., Morrow, M., & Wen, H. Y. (2019). Pathologic complete response rate according to HER2 detection methods in HER2-positive breast cancer treated with neoadjuvant systemic therapy. *Breast Cancer Research and Treatment*, *177*(1), 61–66. https://doi.org/10.1007/s10549-019-05295-9

Kümmel, S., Holtschmidt, J., & Loibl, S. (2014). Surgical treatment of primary breast cancer in the neoadjuvant setting. *British Journal of Surgery*, *101*(8), 912–924. https://doi.org/10.1002/bjs.9545

LeBleu, V. S., O'Connell, J. T., Gonzalez Herrera, K. N., Wikman, H., Pantel, K., Haigis, M. C., de Carvalho, F. M., Damascena, A., Domingos Chinen, L. T., Rocha, R. M., Asara, J. M., & Kalluri, R. (2014). PGC-1α mediates

mitochondrial biogenesis and oxidative phosphorylation in cancer cells to promote metastasis. *Nature Cell Biology*, *16*(10), 992–1003. https://doi.org/10.1038/ncb3039

Liberti, M. v., & Locasale, J. W. (2016). The Warburg Effect: How Does it Benefit Cancer Cells? *Trends in Biochemical Sciences*, *41*(3), 211–218. https://doi.org/10.1016/j.tibs.2015.12.001

Littell, R., Freund, R., & Spector, P. (1991). *SAS System for Linear Models* (Third). SAS Institute.

Liu, C., Li, M., Dong, Z.-X., Jiang, D., Li, X., Lin, S., Chen, D., Zou, X., Zhang, X.-D., & Luker, G. D. (2021). Heterogeneous microenvironmental stiffness regulates pro-metastatic functions of breast cancer cells. *Acta Biomaterialia*, *131*, 326–340. https://doi.org/10.1016/j.actbio.2021.07.009

Liu, Z., Pouli, D., Alonzo, C. A., Varone, A., Karaliota, S., Quinn, K. P., Münger, K., Karalis, K. P., & Georgakoudi, I. (2018). Mapping metabolic changes by noninvasive, multiparametric, high-resolution imaging using endogenous contrast. *Science Advances*, *4*(3). https://doi.org/10.1126/sciadv.aap9302

Mah, E. J., Lefebvre, A. E. Y. T., McGahey, G. E., Yee, A. F., & Digman, M. A. (2018). Collagen density modulates triple-negative breast cancer cell metabolism through adhesion-mediated contractility. *Scientific Reports*, *8*(1), 17094. https://doi.org/10.1038/s41598-018-35381-9

Martin, J. D., Seano, G., & Jain, R. K. (2019). Normalizing Function of Tumor Vessels: Progress, Opportunities, and Challenges. *Annual Review of Physiology*, *81*(1), 505–534. https://doi.org/10.1146/annurev-physiol-020518-114700

Martínez-Lostao, L., Anel, A., & Pardo, J. (2015). How Do Cytotoxic Lymphocytes Kill Cancer Cells? *Clinical Cancer Research*, *21*(22), 5047–5056. https://doi.org/10.1158/1078-0432.CCR-15-0685

Masuda, N., Higaki, K., Takano, T., Matsunami, N., Morimoto, T., Ohtani, S., Mizutani, M., Miyamoto, T., Kuroi, K., Ohno, S., Morita, S., & Toi, M. (2014). A phase II study of metronomic paclitaxel/cyclophosphamide/capecitabine followed by 5-fluorouracil/epirubicin/cyclophosphamide as preoperative chemotherapy for triple-negative or low hormone receptor expressing/HER2-negative primary breast cancer. *Cancer Chemotherapy and Pharmacology*, *74*(2), 229–238. https://doi.org/10.1007/s00280-014-2492-y

Maurer, C. R., Rensheng Qi, & Raghavan, V. (2003). A linear time algorithm for computing exact Euclidean distance transforms of binary images in arbitrary dimensions. *IEEE Transactions on Pattern Analysis and Machine Intelligence*, *25*(2), 265–270. https://doi.org/10.1109/TPAMI.2003.1177156

Mclaughlin, R., & Hylton, N. (2011). MRI in breast cancer therapy monitoring. *NMR in Biomedicine*, *24*(6), 712–720. https://doi.org/10.1002/nbm.1739

Meisamy, S., Bolan, P. J., Baker, E. H., Bliss, R. L., Gulbahce, E., Everson, L. I., Nelson, M. T., Emory, T. H., Tuttle, T. M., Yee, D., & Garwood, M. (2004). Neoadjuvant Chemotherapy of Locally Advanced Breast Cancer: Predicting Response with in Vivo 1 H MR Spectroscopy—A Pilot Study at 4 T. *Radiology*, *233*(2), 424–431. https://doi.org/10.1148/radiol.2332031285

Mendrik, A. M., Vonken, E.-J., Rutten, A., Viergever, M. A., & van Ginneken, B. (2009). Noise Reduction in Computed Tomography Scans Using 3-D Anisotropic Hybrid Diffusion With Continuous Switch. *IEEE Transactions on Medical Imaging*, *28*(10), 1585–1594. https://doi.org/10.1109/TMI.2009.2022368

Mieog, J. S. D., van der Hage, J. A., & van de Velde, C. J. H. (2007). Neoadjuvant chemotherapy for operable breast cancer. *British Journal of Surgery*, *94*(10), 1189–1200. https://doi.org/10.1002/bjs.5894

Morris, B. A., Burkel, B., Ponik, S. M., Fan, J., Condeelis, J. S., Aguirre-Ghiso, J. A., Castracane, J., Denu, J. M., & Keely, P. J. (2016). Collagen Matrix Density Drives the Metabolic Shift in Breast Cancer Cells. *EBioMedicine*, *13*, 146–156. https://doi.org/10.1016/j.ebiom.2016.10.012

Mourant, J. R., Fuselier, T., Boyer, J., Johnson, T. M., & Bigio, I. J. (1997). Predictions and measurements of scattering and absorption over broad wavelength ranges in tissue phantoms. *Applied Optics*, *36*(4), 949. https://doi.org/10.1364/ao.36.000949

Mulvey, C. S., Lie, W.-H., Bigio, I. J., Zhang, K., & Waxman, D. (2011). Wavelength-dependent backscattering measurements for quantitative monitoring of apoptosis, Part 2: early spectral changes during apoptosis are linked to apoptotic volume decrease. *Journal of Biomedical Optics*, *16*(11), 117002. https://doi.org/10.1117/1.3644911

Mulvey, C. S., Zhang, K., Liu, W.-H. B., Waxman, D. J., & Bigio, I. J. (2011). Wavelength-dependent backscattering measurements for quantitative monitoring of apoptosis, Part 1: early and late spectral changes are indicative of the presence of apoptosis in cell cultures. *Journal of Biomedical Optics*, *16*(11), 117001. https://doi.org/10.1117/1.3644389

Munzone, E., & Colleoni, M. (2015). Clinical overview of metronomic chemotherapy in breast cancer. *Nature Reviews Clinical Oncology*, *12*(11), 631–644. https://doi.org/10.1038/nrclinonc.2015.131

Nakasone, E. S., Askautrud, H. A., Kees, T., Park, J.-H., Plaks, V., Ewald, A. J., Fein, M., Rasch, M. G., Tan, Y.-X., Qiu, J., Park, J., Sinha, P., Bissell, M. J., Frengen, E., Werb, Z., & Egeblad, M. (2012). Imaging Tumor-Stroma Interactions during Chemotherapy Reveals Contributions of the Microenvironment to Resistance. *Cancer Cell*, *21*(4), 488–503. https://doi.org/10.1016/j.ccr.2012.02.017

National Cancer Institute. (2022). *SEER Cancer Stat Facts: Female Breast Cancer*. National Cancer Institute. https://seer.cancer.gov/statfacts/html/breast.html

NCCN. (2019). *Clinical Practice Guidelines: Breast Cancer*. National Comprehensive Cancer Network. https://www.nccn.org/professionals/physician_gls/pdf/breast_blocks.pdf

NCCN. (2022). *NCCN Clinical Practice Guidelines in Oncology: Breast Cancer*.

Newton, K., & Dixit, V. M. (2012). Signaling in Innate Immunity and Inflammation. *Cold Spring Harbor Perspectives in Biology*, *4*(3), a006049–a006049. https://doi.org/10.1101/cshperspect.a006049

No, K., Kwong, R., Chou, P. H., & Cerussi, A. (2008). Design and testing of a miniature broadband frequency domain photon migration instrument. *Journal of Biomedical Optics*, *13*(5), 050509. https://doi.org/10.1117/1.2998473

O'Farrell, A. C., Shnyder, S. D., Marston, G., Coletta, P. L., & Gill, J. H. (2013). Non-invasive molecular imaging for preclinical cancer therapeutic development. *British Journal of Pharmacology*, *169*(4), 719–735. https://doi.org/10.1111/bph.12155

Oshi, M., Asaoka, M., Tokumaru, Y., Yan, L., Matsuyama, R., Ishikawa, T., Endo, I., & Takabe, K. (2020). CD8 T Cell Score as a Prognostic Biomarker for Triple Negative Breast Cancer. *International Journal of Molecular Sciences*, *21*(18), 1–16. https://doi.org/10.3390/IJMS21186968

O'Sullivan, T. D., Cerussi, A. E., Cuccia, D. J., & Tromberg, B. J. (2012). Diffuse optical imaging using spatially and temporally modulated light. *Journal of Biomedical Optics*, *17*(7), 0713111. https://doi.org/10.1117/1.JBO.17.7.071311

Otsu, N. (1979). A Threshold Selection Method from Gray-Level Histograms. *IEEE Transactions on Systems, Man, and Cybernetics*, *9*(1), 62–66. https://doi.org/10.1109/TSMC.1979.4310076

Park, J. S., Burckhardt, C. J., Lazcano, R., Solis, L. M., Isogai, T., Li, L., Chen, C. S., Gao, B., Minna, J. D., Bachoo, R., DeBerardinis, R. J., & Danuser, G. (2020). Mechanical regulation of glycolysis via cytoskeleton architecture. *Nature*, *578*(7796), 621–626. https://doi.org/10.1038/s41586-020-1998-1

Partridge, S. C., Zhang, Z., Newitt, D. C., Gibbs, J. E., Chenevert, T. L., Rosen, M. A., Bolan, P. J., Marques, H. S., Romanoff, J., Cimino, L., Joe, B. N., Umphrey, H. R., Ojeda-Fournier, H., Dogan, B., Oh, K., Abe, H., Drukteinis, J. S., Esserman, L. J., & Hylton, N. M. (2018). Diffusion-weighted MRI Findings Predict Pathologic Response in Neoadjuvant Treatment of Breast Cancer: The ACRIN 6698 Multicenter Trial. *Radiology*, *289*(3), 618–627. https://doi.org/10.1148/radiol.2018180273

Pasquier, E., Kavallaris, M., & André, N. (2010). Metronomic chemotherapy: New rationale for new directions. *Nature Reviews Clinical Oncology*, *7*(8), 455–465. https://doi.org/10.1038/nrclinonc.2010.82

Pastore, M., & Calcagnì, A. (2019). Measuring Distribution Similarities Between Samples: A Distribution-Free Overlapping Index. *Frontiers in Psychology*, *10*. https://doi.org/10.3389/fpsyg.2019.01089

Pavel, M., Renna, M., Park, S. J., Menzies, F. M., Ricketts, T., Füllgrabe, J., Ashkenazi, A., Frake, R. A., Lombarte, A. C., Bento, C. F., Franze, K., & Rubinsztein, D. C. (2018). Contact inhibition controls cell survival and proliferation via YAP/TAZ-autophagy axis. *Nature Communications*, *9*(1), 2961. https://doi.org/10.1038/s41467-018-05388-x

Perrin, L., Bayarmagnai, B., & Gligorijevic, B. (2020). Frontiers in intravital multiphoton microscopy of cancer. *Cancer Reports*, *3*(1), 1–22. https://doi.org/10.1002/cnr2.1192

Pham, T. H., Coquoz, O., Fishkin, J. B., Anderson, E., & Tromberg, B. J. (2000). Broad bandwidth frequency domain instrument for quantitative tissue optical spectroscopy. *Review of Scientific Instruments*, *71*(6), 2500. https://doi.org/10.1063/1.1150665

Pucci, B., Kasten, M., & Giordano, A. (2000). Cell Cycle and Apoptosis. *Neoplasia*, *2*(4), 291–299. https://doi.org/10.1038/sj.neo.7900101

Quinn, K. P., Sridharan, G. v., Hayden, R. S., Kaplan, D. L., Lee, K., & Georgakoudi, I. (2013). Quantitative metabolic imaging using endogenous fluorescence to detect stem cell differentiation. *Scientific Reports*, *3*(1), 3432. https://doi.org/10.1038/srep03432

Rastogi, P., Anderson, S. J., Bear, H. D., Geyer, C. E., Kahlenberg, M. S., Robidoux, A., Margolese, R. G., Hoehn, J. L., Vogel, V. G., Dakhil, S. R., Tamkus, D., King, K. M., Pajon, E. R., Wright, M. J., Robert, J., Paik, S., Mamounas, E. P., & Wolmark, N. (2008). Preoperative Chemotherapy: Updates of National Surgical Adjuvant Breast and Bowel Project Protocols B-18 and B-27. *Journal of Clinical Oncology*, *26*(5), 778–785. https://doi.org/10.1200/JCO.2007.15.0235

Robbins, C. M., Raghavan, G., Antaki, J. F., & Kainerstorfer, J. M. (2017). Feasibility of spatial frequency-domain imaging for monitoring palpable breast lesions. *J Biomed Opt*, *22*(12), 1–9. https://doi.org/10.1117/1.JBO.22.12.121605

Roblyer, D., Ueda, S., Cerussi, A., Tanamai, W., Durkin, A., Mehta, R., Hsiang, D., Butler, J. a, McLaren, C., Chen, W.-P., & Tromberg, B. (2011). Optical imaging of breast cancer oxyhemoglobin flare correlates with neoadjuvant chemotherapy response one day after starting treatment. *Proceedings of the National Academy of Sciences of the United States of America*, *108*(35), 14626–14631. https://doi.org/10.1073/pnas.1013103108

Roghanian, A., Hu, G., Fraser, C., Singh, M., Foxall, R. B., Meyer, M. J., Lees, E., Huet, H., Glennie, M. J., Beers, S. A., Lim, S. H., Ashton-key, M., Thirdborough, S. M., Cragg, M. S., & Chen, J. (2019). *Cyclophosphamide Enhances Cancer Antibody Immunotherapy in the Resistant Bone Marrow Niche by Modulating Macrophage Fc γ R Expression*. https://doi.org/10.1158/2326-6066.CIR-18-0835

Sajjadi, A. Y., Isakoff, S. J., Deng, B., Singh, B., Wanyo, C. M., Fang, Q., Specht, M. C., Schapira, L., Moy, B., Bardia, A., Boas, D. A., & Carp, S. A. (2017).

Normalization of compression-induced hemodynamics in patients responding to neoadjuvant chemotherapy monitored by dynamic tomographic optical breast imaging (DTOBI). *Biomedical Optics Express*, *8*(2), 555. https://doi.org/10.1364/BOE.8.000555

Sakadžić, S., Roussakis, E., Yaseen, M. A., Mandeville, E. T., Srinivasan, V. J., Arai, K., Ruvinskaya, S., Devor, A., Lo, E. H., Vinogradov, S. A., & Boas, D. A. (2010). Two-photon high-resolution measurement of partial pressure of oxygen in cerebral vasculature and tissue. *Nature Methods*, *7*(9), 755–759. https://doi.org/10.1038/nmeth.1490

Sharma, P., Hu-Lieskovan, S., Wargo, J. A., & Ribas, A. (2017). Primary, Adaptive, and Acquired Resistance to Cancer Immunotherapy. *Cell*, *168*(4), 707–723. https://doi.org/10.1016/j.cell.2017.01.017

Soille, P. (1999). *Morphological Image Analysis*. Springer Berlin Heidelberg. https://doi.org/10.1007/978-3-662-03939-7

Sopik, V., & Narod, S. A. (2018). The relationship between tumour size, nodal status and distant metastases: on the origins of breast cancer. *Breast Cancer Research and Treatment*, *170*(3), 647–656. https://doi.org/10.1007/s10549-018-4796-9

Tabassum, S., Pera, V., Greening, G., Muldoon, T. J., & Roblyer, D. (2018). Two-layer inverse model for improved longitudinal preclinical tumor imaging in the spatial frequency domain. *Journal of Biomedical Optics*, *23*(07), 1. https://doi.org/10.1117/1.jbo.23.7.076011

Tabassum, S., Tank, A., Wang, F., Karrobi, K., Vergato, C., Bigio, I. J., Waxman, D. J., & Roblyer, D. (2021). Optical scattering as an early marker of apoptosis during chemotherapy and antiangiogenic therapy in murine models of prostate and breast cancer. *Neoplasia*, *23*(3), 294–303. https://doi.org/10.1016/j.neo.2021.01.005

Tabassum, S., Zhao, Y., Istfan, R., Wu, J., Waxman, D. J., & Roblyer, D. (2016). Feasibility of spatial frequency domain imaging (SFDI) for optically characterizing a preclinical oncology model. *Biomedical Optics Express*, *7*(10), 4154. https://doi.org/10.1364/boe.7.004154

Tank, A., Peterson, H. M., Pera, V., Tabassum, S., Leproux, A., O'Sullivan, T., Jones, E., Cabral, H., Ko, N., Mehta, R. S., Tromberg, B. J., & Roblyer, D. (2020). Diffuse optical spectroscopic imaging reveals distinct early breast tumor hemodynamic responses to metronomic and maximum tolerated dose regimens. *Breast Cancer Research*, *22*(1), 1–10. https://doi.org/10.1186/s13058-020-01262-1

Tank, A., Vergato, C., Waxman, D. J., & Roblyer, D. (2022). Spatial frequency domain imaging for monitoring immune-mediated chemotherapy treatment response and resistance in a murine breast cancer model. *Scientific Reports*, *12*(1), 5864. https://doi.org/10.1038/s41598-022-09671-2

Tromberg, B. J., Pogue, B. W., Paulsen, K. D., Yodh, A. G., Boas, D. A., & Cerussi, A. E. (2008). Assessing the future of diffuse optical imaging technologies for breast cancer management. *Medical Physics*, *35*(6Part1), 2443–2451. https://doi.org/10.1118/1.2919078

Tromberg, B. J., Zhang, Z., Leproux, A., O'Sullivan, T. D., Cerussi, A. E., Carpenter, P. M., Mehta, R. S., Roblyer, D., Yang, W., Paulsen, K. D., Pogue, B. W., Jiang, S., Kaufman, P. A., Yodh, A. G., Chung, S. H., Schnall, M., Snyder, B. S., Hylton, N., Boas, D. A., … Mankoff, D. (2016). Predicting responses to neoadjuvant chemotherapy in breast cancer: ACRIN 6691 trial of diffuse optical spectroscopic imaging. *Cancer Research*, *76*(20), 5933–5944. https://doi.org/10.1158/0008-5472.CAN-16-0346

Ueda, S., Roblyer, D., Cerussi, A., Durkin, A., Leproux, A., Santoro, Y., Xu, S., O'Sullivan, T. D., Hsiang, D., Mehta, R., Butler, J., & Tromberg, B. J. (2012). Baseline tumor oxygen saturation correlates with a pathologic complete response in breast cancer patients undergoing neoadjuvant chemotherapy. *Cancer Research*, *72*(17), 4318–4328. https://doi.org/10.1158/0008-5472.CAN-12-0056

Ueda, S., Saeki, T., Osaki, A., Yamane, T., & Kuji, I. (2017). Bevacizumab induces acute hypoxia and cancer progression in patients with refractory breast cancer: Multimodal functional imaging and multiplex cytokine analysis. *Clinical Cancer Research*, *23*(19), 5769–5778. https://doi.org/10.1158/1078-0432.CCR-17-0874

Varone, A., Xylas, J., Quinn, K. P., Pouli, D., Sridharan, G., McLaughlin-Drubin, M. E., Alonzo, C., Lee, K., Münger, K., & Georgakoudi, I. (2014). Endogenous Two-Photon Fluorescence Imaging Elucidates Metabolic Changes Related to Enhanced Glycolysis and Glutamine Consumption in Precancerous Epithelial Tissues. *Cancer Research*, *74*(11), 3067–3075. https://doi.org/10.1158/0008-5472.CAN-13-2713

Vergato, C., Doshi, K., Roblyer, D., & Waxman, D. (2021). Type-I interferon signaling is essential for robust metronomic chemo-immunogenic tumor regression in murine triple-negative breast cancer. *BioRxiv*. https://doi.org/10.1101/2021.12.05.471293

Viani, G. A., Afonso, S. L., Stefano, E. J., de Fendi, L. I., & Soares, F. v. (2007). Adjuvant trastuzumab in the treatment of her-2-positive early breast cancer: a meta-analysis of published randomized trials. *BMC Cancer*, *7*(1), 153. https://doi.org/10.1186/1471-2407-7-153

von Minckwitz, G., Huang, C.-S., Mano, M. S., Loibl, S., Mamounas, E. P., Untch, M., Wolmark, N., Rastogi, P., Schneeweiss, A., Redondo, A., Fischer, H. H., Jacot, W., Conlin, A. K., Arce-Salinas, C., Wapnir, I. L., Jackisch, C., DiGiovanna, M. P., Fasching, P. A., Crown, J. P., … Geyer, C. E. (2019). Trastuzumab Emtansine for Residual Invasive HER2-Positive Breast Cancer. *New England Journal of Medicine*, *380*(7), 617–628. https://doi.org/10.1056/NEJMoa1814017

Vonderheide, R. H., Domchek, S. M., & Clark, A. S. (2017). Immunotherapy for Breast Cancer: What Are We Missing? *Clinical Cancer Research*, *23*(11), 2640–2646. https://doi.org/10.1158/1078-0432.CCR-16-2569

Wallrabe, H., Svindrych, Z., Alam, S. R., Siller, K. H., Wang, T., Kashatus, D., Hu, S., & Periasamy, A. (2018). Segmented cell analyses to measure redox states of autofluorescent NAD(P)H, FAD & Trp in cancer cells by FLIM. *Scientific Reports*, *8*(1), 79. https://doi.org/10.1038/s41598-017-18634-x

Walsh, A. J., Cook, R. S., Manning, H. C., Hicks, D. J., Lafontant, A., Arteaga, C. L., & Skala, M. C. (2013). Optical Metabolic Imaging Identifies Glycolytic Levels, Subtypes, and Early-Treatment Response in Breast Cancer. *Cancer Research*, *73*(20), 6164–6174. https://doi.org/10.1158/0008-5472.CAN-13-0527

Walsh, A. J., Cook, R. S., Sanders, M. E., Aurisicchio, L., Ciliberto, G., Arteaga, C. L., & Skala, M. C. (2014). Quantitative Optical Imaging of Primary Tumor Organoid Metabolism Predicts Drug Response in Breast Cancer. *Cancer Research*, *74*(18), 5184–5194. https://doi.org/10.1158/0008-5472.CAN-14-0663

Walsh, J. C., Lebedev, A., Aten, E., Madsen, K., Marciano, L., & Kolb, H. C. (2014). The clinical importance of assessing tumor hypoxia: Relationship of tumor hypoxia to prognosis and therapeutic opportunities. *Antioxidants and Redox Signaling*, *21*(10), 1516–1554. https://doi.org/10.1089/ars.2013.5378

Wanderley, C. W., Colon, D. F., Luiz, J. P. M., Oliveira, F. F., Viacava, P. R., Leite, C. A., Pereira, J. A., Silva, C. M., Silva, C. R., Silva, R. L., Speck-Hernandez, C. A., Mota, J. M., Alves-Filho, J. C., Lima-Júnior, R. C., Cunha, T. M., & Cunha, F. Q. (2018). Paclitaxel reduces tumor growth by reprogramming tumor-associated macrophages to an M1- profile in a TLR4-dependent manner. *Cancer Research*, *78*(20), canres.3480.2017. https://doi.org/10.1158/0008-5472.CAN-17-3480

Warburg, O., Wind, F., & Negelein, E. (1927). THE METABOLISM OF TUMORS IN THE BODY. *Journal of General Physiology*, *8*(6), 519–530. https://doi.org/10.1085/jgp.8.6.519

Weickert, J., & Scharr, H. (2002). A Scheme for Coherence-Enhancing Diffusion Filtering with Optimized Rotation Invariance. *Journal of Visual Communication and Image Representation*, *13*(1–2), 103–118. https://doi.org/10.1006/jvci.2001.0495

Winkler, J., Abisoye-Ogunniyan, A., Metcalf, K. J., & Werb, Z. (2020). Concepts of extracellular matrix remodelling in tumour progression and metastasis. *Nature Communications*, *11*(1), 5120. https://doi.org/10.1038/s41467-020-18794-x

Yeh, E., Slanetz, P., Kopans, D. B., Rafferty, E., Georgian-Smith, D., Moy, L., Halpern, E., Moore, R., Kuter, I., & Taghian, A. (2005). Prospective Comparison of Mammography, Sonography, and MRI in Patients

Undergoing Neoadjuvant Chemotherapy for Palpable Breast Cancer. *American Journal of Roentgenology*, *184*(3), 868–877. https://doi.org/10.2214/ajr.184.3.01840868

Zancan, P., Sola-Penna, M., Furtado, C. M., & da Silva, D. (2010). Differential expression of phosphofructokinase-1 isoforms correlates with the glycolytic efficiency of breast cancer cells. *Molecular Genetics and Metabolism*, *100*(4), 372–378. https://doi.org/10.1016/j.ymgme.2010.04.006

Zanconato, F., Cordenonsi, M., & Piccolo, S. (2016). YAP/TAZ at the Roots of Cancer. *Cancer Cell*, *29*(6), 783–803. https://doi.org/10.1016/j.ccell.2016.05.005

Zanotelli, M. R., Goldblatt, Z. E., Miller, J. P., Bordeleau, F., Li, J., VanderBurgh, J. A., Lampi, M. C., King, M. R., & Reinhart-King, C. A. (2018). Regulation of ATP utilization during metastatic cell migration by collagen architecture. *Molecular Biology of the Cell*, *29*(1), 1–9. https://doi.org/10.1091/mbc.E17-01-0041

Zanotelli, M. R., Zhang, J., & Reinhart-King, C. A. (2021). Mechanoresponsive metabolism in cancer cell migration and metastasis. *Cell Metabolism*, *33*(7), 1307–1321. https://doi.org/10.1016/j.cmet.2021.04.002

Zhang, J., Goliwas, K. F., Wang, W., Taufalele, P. v., Bordeleau, F., & Reinhart-King, C. A. (2019). Energetic regulation of coordinated leader–follower dynamics during collective invasion of breast cancer cells. *Proceedings of the National Academy of Sciences*, *116*(16), 7867–7872. https://doi.org/10.1073/pnas.1809964116

Zhao, Y., Tabassum, S., Piracha, S., Nandhu, M. S., Viapiano, M., & Roblyer, D. (2016). Angle correction for small animal tumor imaging with spatial frequency domain imaging (SFDI). *Biomedical Optics Express*, *7*(6), 2373. https://doi.org/10.1364/boe.7.002373

Zheng, X., Fang, Z., Liu, X., Deng, S., Zhou, P., Wang, X., Zhang, C., Yin, R., Hu, H., Chen, X., Han, Y., Zhao, Y., Lin, S. H., Qin, S., Wang, X., Kim, B. Y. S., Zhou, P., Jiang, W., Wu, Q., & Huang, Y. (2018). Increased vessel perfusion predicts the efficacy of immune checkpoint blockade. *The Journal of Clinical Investigation*, *128*(5), 2104–2115. https://doi.org/10.1172/JCI96582

Zhu, Q., Tannenbaum, S., Kurtzman, S. H., DeFusco, P., Ricci, A., Vavadi, H., Zhou, F., Xu, C., Merkulov, A., Hegde, P., Kane, M., Wang, L., & Sabbath, K. (2018). Identifying an early treatment window for predicting breast cancer response to neoadjuvant chemotherapy using immunohistopathology and hemoglobin parameters. *Breast Cancer Research*, *20*(1), 1–17. https://doi.org/10.1186/s13058-018-0975-1

CURRICULUM VITAE

Anup Tank

anuptank@gmail.com • linkedin.com/in/anuptank • +1-408-472-5167

Education

Boston University
Ph.D. Candidate in Biomedical Engineering — *Sep '16 - Aug '22 (Expected)*

University of California, San Diego
B.S. in Nanoengineering: Bioengineering — *Jun '16*

Research Experience

Boston University
Graduate Researcher, Biomedical Optical Technologies Lab — *Sep '16 – Present*
Developing optical tools to study breast cancer treatment response in pre-clinical and clinical subjects

- Performed longitudinal statistical analysis of a large dataset of optical measurements on breast cancer patients undergoing chemotherapy to quantify prognostic biomarkers and treatment specific effects.
- Developed image processing pipeline to analyze changes in tumor vasculature and intravascular pO_2 using multiphoton microscopy in a mouse model.
- Conducted longitduinal optical measurements in mouse breast cancer model to discover prognostic optical biomarkers capable of differentiating immune responsiveness and resistance using discriminant analysis.
- Analyzed non-invasive optical metabolic profiles and spatial distributions of non-metastatic and metastatic 3D breast cancer spheroids.

University of California, San Diego
Undergraduate Researcher, Esener Lab for Biophotonics — *Oct '14 – Jun '16*
Designing optical systems to manipulate nanoscale objects

- Led project to build a custom microscope-optical tweezer system with a spatial light modulator (SLM).
- Characterized the phase shift-polarization relationship of a SLM and developed a forward and inverse model.
- Developed LabView software to integrate optical tweezer-SLM use and dynamically encode polarization.

University of California, San Diego
Project Team Lead, Engineering World Health — *Sep '13 – Jun '16*
Developing low cost platform to detect HIV drug resistance for low resource settings

- Led the development of affordable, fully automated RNA extraction system.
- Designed circuitry and software for precise control of microfluidic pumps using an Arduino.

Relevant Experience

Boston University Optica/SPIE Chapter: **President** — *Mar '18 - Present*

- Led board of 5 students to apply for grants, manage budgets,plan quarterly seminars,and organize community outreach and professional development events.
- Organized Boston Photonics Conference for more than 300 attendees from 12 universities and 6 companies.

Boston University Graduate Teaching Fellow — *Jan '19 - May '19, Jan '20 - May '20*

- Primary Teaching Fellow for courses: Computational Linear Algebra and Biomedical Measurements Lab.
- Led discussion and lab sessions for ∼30 students.

Intern, Biotech Vendor Services — *May '14 - Oct '14*

- Led group to integrate new biotech vendors onto company platform to connect with prospective clients.
- Preformed outreach to invite local life science companies and academic institutions to vendor showcases.

Additional Skills

Technical: MATLAB, Python, ImageJ, Labview, SolidWorks, SAS, JMP, Excel, Office
Research: Multiphoton Microscopy, Animal Handling & Surgery, Cell Culture, IACUC Correspondence

Selected Publications

Tank, A., Peterson, H.M., Pera, V. et al. Diffuse optical spectroscopic imaging reveals distinct early breast tumor hemodynamic responses to metronomic and maximum tolerated dose regimens. Breast Cancer Res 22, 29 (2020).https://doi.org/10.1186/s13058-020-01262-1

Tank, A., Vergato, C., Waxman, D.J. et al. Spatial frequency domain imaging for monitoring immune-mediated chemotherapy treatment response and resistance in a murine breast cancer model. Sci Rep 12, 5864 (2022). https://doi.org/10.1038/s41598-022-09671-2

Tabassum, S., **Tank, A.** et al. Optical scattering as an early marker of apoptosis during chemotherapy and antiangiogenic therapy in murine models of prostate and breast cancer, Neoplasia, Volume 23, Issue 3,2021,Pages 294-303,ISSN 1476-5586, https://doi.org/10.1016/j.neo.2021.01.005.

Karrobi, K., **Tank, A.** et al. "Diffuse and Nonlinear Imaging of Multiscale Vascular Parameters for in Vivo Monitoring of Preclinical Mammary Tumors." Journal of Biophotonics, vol.12, no.6, 2019, doi:10.1002/jbio.201800379.

For a complete publication list including 7 peer-reviewed articles, and 5 conference abstracts, please refer to
https://www.ncbi.nlm.nih.gov/myncbi/1fSO3TWCs1UEdo/bibliography/public/.